

Exploring the mass accretion rates of neutron star X-ray
binaries and the properties of Cadmium Zinc Telluride
for hard X-ray astronomy

Thesis by
Sean N. Pike

In Partial Fulfillment of the Requirements for the
Degree of
PhD in Physics

The logo for the California Institute of Technology (Caltech), featuring the word "Caltech" in a bold, orange, sans-serif font.

CALIFORNIA INSTITUTE OF TECHNOLOGY
Pasadena, California

2023
Defended July 18, 2022

© 2023

Sean N. Pike

ORCID: 0000-0002-8403-0041

All rights reserved

ACKNOWLEDGEMENTS

It's almost impossible to count the number of people responsible for my success leading to the submission of this dissertation, much less to list them all, but I will attempt to acknowledge some of those most impactful during my time at Caltech. I would of course like to thank my advisor, Fiona Harrison, for many years of guidance, for encouraging me get involved in all sorts of exciting projects and collaborations even when I was in way over my head, and for cultivating within the NuSTAR group an environment of mutual respect and scientific excellence where each person feels valued as a human being. I would also like to thank everyone in the NuSTAR group for constantly teaching me new things and answering my constant and varied questions. I would particularly like to acknowledge Brian Grefenstette, Kristin Madsen, Hiromasa Miyasaka, and Vikram Rana for their guidance in the lab, as well as Javier Garcia, Murray Brightman, Amruta Jaodand, and Renee Ludlam for helping me become an Xspec wizard.

I want to thank each of the SURF students I have mentored for being patient as I learned how to guide young scientists through scientific projects, and for pushing me to be a better scientist in turn. I want to especially thank Julian Sanders and Andrew Sosanya for working hard to translate my mess of Python scripts into the first iteration of the nudetect module, which has been invaluable to my work on X-ray detectors, and which I hope will continue to aid the lab in detector characterization.

I want to thank the CaltechY, and Liz Jackman in particular for doing so much amazing work running the Rise program, in which I participated as a tutor for several years. Liz is really one of the most thoughtful people I've met at Caltech. Whatever she's getting paid, it should be doubled. I also thank the dining, facilities, janitorial, library, and other staff at Caltech for making this place run, and I believe their pay should also be doubled. The same goes for Mika and Nam, who have put so much effort into trying to make the Physics program at Caltech more welcoming and enjoyable for grad students.

My parents Jon and Diana were the first to teach me to ask questions and to think hard in order to grasp at answers, and for that they share most of the responsibility for this thesis. My brother Daniel has been a constant source of laughter and humility, keeping me from getting too caught up in my own issues. And of course it's very likely I would not have completed this thesis without the constant support of my

partner in life and in crime, Sarah. Our dogs, Sparky and Snuggles, have also played an important role in keeping me happy and healthy over the past 6+ years, and I'm going to give them many treats after I defend.

I acknowledge the many irreplaceable friends I made at Caltech with whom I spent countless hours playing DnD, dancing, exploring, eating good food, and commiserating. I didn't expect to find at Caltech many of the most incredible people I have ever met in my life. Thanks to Mats and Josh, Rob and Lealia, Reem and Ivaylo. I want to thank everyone in the Socialists of Caltech for being extremely cool and smart and for transforming the way I understand the world, for honing my ability to question my own beliefs, and for developing my skills as an organizer so that I can feel confident going into the world and producing liberatory change. Thanks to Jane, Ashay, B, Peishi, Arian, and everyone else in SoC.

Finally, I feel it's important to acknowledge that this thesis work was undertaken on occupied Tongva land. I firmly believe that science cannot achieve its potential as an endeavor which enriches the lives of all people until we bring about the end of settler colonial capitalist society.

ABSTRACT

My thesis work has consisted of investigations of several X-ray binaries using the Nuclear Spectroscopic Telescope Array (NuSTAR), as well as characterization of NuSTAR-like hybrid X-ray detectors for the purpose of future hard X-ray observatories. I present analyses of three X-ray binaries in particular, probing different luminosities with the goal of investigating accreting neutron stars at different accretion rates. At high accretion rates, approaching and moderately exceeding the Eddington limit, I performed a timing and spectral analysis of the neutron star supergiant X-ray binary SMC X-1. I tracked the transient pulsations of this source at different apparent luminosities and analyzed the source spectrum as pulsations evolved in order to infer that the mechanism leading to pulsation transience is likely related to periodic obscuration by a warped accretion disk. At lower accretion rates, I studied the low-mass X-ray binary GRS 1741.9–2853. I proposed for NuSTAR observations of this source in outburst, and as a result I observed two type-I X-ray bursts originating from the source. I performed a time-resolved spectroscopic study of each of these bursts, and I used the results of this analysis to determine the composition of the burning material and the distance to the source from Earth. The third X-ray binary I present is MAXI J1848–015. This source was discovered by the Monitor of All-sky X-ray Image (MAXI) in winter 2020 at which point its luminosity was abnormally low for an accreting compact object in outburst, making it a good candidate for the study of neutron star X-ray binaries at low accretion rates. I performed rapid follow-up of the source with NuSTAR, and I performed a detailed spectroscopic study of the NuSTAR observations, utilizing relativistic disk reflection models in order to determine that the source is in fact a black hole rather than a neutron star. Complementing these observational astrophysics projects, I characterized Cadmium Zinc Telluride (CZT) detectors procured from Redlen Technologies in order to determine their usefulness for future hard X-ray observatories. Using Python, I produced an adaptable calibration and analysis pipeline with which to analyze noise, leakage current, spectral, and other data which I obtained in the lab. Using this pipeline, I determined that the material available from Redlen shows good uniformity, yield, and superior spectral resolution up to high photon energies, making it an excellent candidate for application to hard X-ray astronomy.

PUBLISHED CONTENT AND CONTRIBUTIONS

Pike, Sean N., Hitoshi Negoro, et al. (Mar. 2022). “MAXI and NuSTAR Observations of the Faint X-Ray Transient MAXI J1848-015 in the GLIMPSE-C01 Cluster”. In: *ApJ* 927.2, 190, p. 190. doi: 10.3847/1538-4357/ac5258. arXiv: 2202.02883 [astro-ph.HE].

S.N.P. participated in the conception of the project and in the proposal of NuSTAR observations. With the exception of Section 5.2, S.N.P. performed all data analysis and calculations, produced the figures and tables, and wrote the manuscript. S.N.P. edited Section 5.2 and submitted and revised the manuscript.

Pike, Sean N., Milan Roberson, et al. (2022). “Properties of Redlen CZT with respect to X-ray spectroscopy”. In: *JATIS* submitted.

S.N.P. participated in the conception of the project and supervised and participated in the collection of data. S.N.P. performed all data analysis and calculations, produced the figures and tables, and wrote, submitted, and revised the manuscript.

Pike, Sean N., Fiona A. Harrison, John A. Tomsick, et al. (Sept. 2021). “Photospheric Radius Expansion and a Double-peaked Type-I X-Ray Burst from GRS 1741.9-2853”. In: *ApJ* 918.1, 9, p. 9. doi: 10.3847/1538-4357/ac0ef9. arXiv: 2106.13312 [astro-ph.HE].

S.N.P. participated in the conception of the project, proposed the NuSTAR observations, performed all data analysis and calculations, produced the figures and tables, and wrote, submitted, and revised the manuscript.

Pike, Sean N., Fiona A. Harrison, Matteo Bachetti, et al. (Apr. 2019). “Observing the Transient Pulsations of SMC X-1 with NuSTAR”. In: *ApJ* 875.2, 144, p. 144. doi: 10.3847/1538-4357/ab0f2b. arXiv: 1903.06306 [astro-ph.HE].

S.N.P. participated in the conception of the project, performed all data analysis and calculations, produced the figures and tables, and wrote, submitted, and revised the manuscript.

TABLE OF CONTENTS

Acknowledgements	iii
Abstract	v
Published Content and Contributions	vi
Table of Contents	vi
List of Illustrations	ix
List of Tables	xviii
Nomenclature	xix
Chapter I: An introduction to X-ray binaries	1
1.1 A brief overview of disk accretion	1
1.2 Observational properties of X-ray Binaries	3
1.3 Neutron star X-ray binaries over a range of accretion rates	8
Chapter II: Instrumentation for the study of hard X-rays	14
2.1 A brief history of hard X-ray observatories	15
2.2 NuSTAR: the Nuclear Spectroscopic Telescope Array	16
2.3 The future of high energy X-ray astronomy	18
Chapter III: Observing the transient pulsations of SMC X-1 with NuSTAR	20
3.1 SMC X-1: a mildly super-Eddington supergiant X-ray binary	20
3.2 Observations and Data Reduction	23
3.3 Timing Analysis	25
3.4 Spectral Analysis	29
3.5 Discussion	34
3.6 Conclusions	36
Chapter IV: Photospheric Radius Expansion and a Double-peaked Type-I X-Ray Burst from GRS 1741.9-2853	37
4.1 Type-I X-ray bursts	37
4.2 Observation and Data Reduction	39
4.3 Light Curve Analysis	41
4.4 Spectral Analysis	44
4.5 Timing Analysis	51
4.6 Discussion	53
4.7 Summary and Conclusions	58
Chapter V: MAXI and NuSTAR observations of the faint X-ray transient MAXI J1848-015 in the GLIMPSE-C01 Cluster	60
5.1 An unknown X-ray transient in outburst	60
5.2 MAXI Observations	63
5.3 NuSTAR Observations	66
5.4 Discussion	78
5.5 Summary and Conclusions	83
Chapter VI: Properties of Redlen CZT with respect to X-ray spectroscopy	85

6.1 CZT detectors for X-ray Astronomy	85
6.2 Leakage Current	86
6.3 Flood illumination	87
6.4 Investigating a small region of the detector	91
6.5 Summary and Conclusions	97
Bibliography	100
Appendix A: Breaking the Spectral fit degeneracy	117
Appendix B: Investigating errors in hybridization	120

LIST OF ILLUSTRATIONS

<i>Number</i>	<i>Page</i>
1.1 Figure from Hynes (2010) showing an artistic representation of a compact object accreting via Roche lobe overflow. Each of the physical regions of the binary system are labeled with the electromagnetic bandpass corresponding to the majority of their emission. NuSTAR primarily observes the innermost regions of the accretion disk thanks to its hard X-ray sensitivity.	1
1.2 Figure from J. García, T. Dauser, Lohfink, et al. (2014) mapping the energy shift of photons from an accretion disk with inclination $i = 80^\circ$ around a maximally spinning black hole as seen by a distant observer.	4
1.3 Figure from R. P. Fender, T. M. Belloni, and Gallo (2004) illustrating the cycle of accretion states exhibited by many accreting black holes. The top panel shows a schematic of the hardness (the fraction of hard X-ray photons to soft X-ray photons) on the x-axis vs. intensity on the y-axis, while the bottom panel plots the disk and jet properties in different states. These states are also shown as illustrations on the left and right hand sides of the figure with the jet shown in blue, the disk shown in red, and the corona shown in yellow. A typical outburst of a black hole X-ray binary begins in the bottom right corner of the top panel, and traverses the hardness-intensity diagram in the counterclockwise direction, following the arrows shown. The source may remain in outburst for months at a time.	6
1.4 The approximate ranges of Eddington fractions, corresponding to accretion rates, of different classes of NS XRB. Atoll and Z-track sources have low-mass companions, while BeXBs, SgXBs, and at least some ULXPs have high-mass companions. The vertical dashed line denotes the Eddington limit itself. Some NS XRBs move between periods of quiescence and periods of outburst, leading to a wide range of observed accretion rates. Each class exhibits unique behavior which evolves depending upon the mass accretion rate.	8

1.5	Figure from Church, Gibiec, and Bałucińska-Church (2014) showing the hardness-intensity diagrams of prototypical Atoll (left) and Z-track (right) sources 4U 0614+091 and GX 340+0, respectively. Both classes of NS LMXB move between different accretion states defined by their positions on these tracks.	9
2.1	Rendering of NuSTAR with insets showing a focal plane module made up of 4 NuSTAR hybrids on the left and the Wolter grazing incidence angle optics on the right.	16
2.2	Schematic showing a sideways cross-section of a NuSTAR hybrid, made up of a CZT crystal shown in grey, 32 stud bumps in gold, and readout electronics in green, interacting with an incoming photon shown as an orange dashed line. When a photon interacts with the detector, it produces a cloud of liberated electrons (blue) and a positively charged hole cloud (purple). An electric field, \vec{E} shown in red, is applied across the detector, causing the electron cloud to drift towards the anode and the hole cloud towards the cathode. In CZT, electrons move more freely than holes, meaning the signal measured due to the motion of electrons is stronger than that of the motion of the hole cloud.	17
2.3	Schematic of a proposed design for the hard X-ray mission concept HEX-P. The focal plane module aboard HEX-P will consist of hybrid detectors very similar in design to those of NuSTAR, but the collecting area will be increased. The design shown here consists of 16 hybrids made up of CZT or similar semiconductor (blue with yellow outlines) bonded to an improved readout electronics (grey).	19
3.1	<i>Swift</i> BAT light curve of SMC X-1 during 2012. The moving average of the BAT flux is shown in gold. A super-orbital period of around 60 days is clearly visible. The red vertical bars indicate the duration of each NuSTAR observation presented here. The first observation (10002013001) took place near the end of the low state, while the second observation (10002013003) took place as the source was growing fainter shortly after the high state.	21

- 3.2 (a) NuSTAR FPMA count rate of the source during the first observation (10002013001). The gap between 30000 and 50000 seconds is due to a failed data downlink and is not inherent to the source. We have split this observation into two epochs. (b) NuSTAR FPMA count rate of the source during the second observation (10002013003). We define the third epoch as the entirety of this observation. The apparent variability on timescales of ~ 5000 s during Epoch III can be attributed to movement of the source between detectors. Both light curves are binned into intervals of 40 s. The orbital phase, which is defined by full eclipse of the source at $\phi = 0$ and $\phi = 1$, is included along the horizontal axis as well as the time in seconds since the beginning of the each observation. 22
- 3.3 Results of pulsation searches applied to each epoch. The left column shows the results of a dynamic folding search. Pulsations are not detected during Epoch I but seem to appear and gradually increase in strength after observation continues during Epoch II. Pulsations are clearly detected in Epoch III and do not appear to vary significantly throughout the epoch. The middle column shows the results of folding searches over both the pulse period and its first derivative. The results of the dynamic searches allowed us to search over a narrower period range. The resulting Z_4^2 distribution (b, e, and h) for each epoch is fitted to a 2-d Gaussian distribution. The mean of the fitted Gaussian is indicated by a black cross while the white contours represent the 1- and 2-sigma confidence regions. The apparent correlation between P and \dot{P} is an artifact of the search itself and is not intrinsic to the source. The maximum Z_4^2 value achieved by each search is indicated by a blue cross and was used to produce pulse profiles shown in blue in panels b, d, and f. In gold are the 90% confidence regions determined by the Monte Carlo procedure described in Section 3.1. When applied to Epoch I, the search produces multiple maxima of relatively low detection probability, resulting in a poor fit which cannot constrain the pulse period and first derivative to within the search bounds. We therefore do not show the fitted Gaussian, and we choose to fold the pulse profile using the maximum nearest the values measured for Epochs II and III. The result is a profile with weak pulsations which are not detected when the last 5000 s of Epoch I are omitted. During Epochs II and III, however, the pulse period is well-constrained, resulting in distinctive pulse profiles, shown in the right column. Note that the scale of the y-axis in panel (c) is narrower than those of (f) and (i) in order to better illustrate the pulse profile during Epoch I. 26

- 3.4 Observed spectra for each epoch are shown unfolded against a model with constant (energy-independent) flux in the top panels, and fitting residuals for three different models are shown in the lower panels. The FPMA spectra are shown in black while the FPMB spectra are shown in red. The data is consistently described well by a partially absorbed power law with a high energy cutoff. While the shape of the continuum remains relatively constant, the covering fraction and absorbing column vary between successive epochs, with the covering fraction decreasing significantly between Epoch II and Epoch III. . . . 32
- 4.1 The total, background subtracted, livetime corrected NuSTAR light curve is shown twice. The light curve in the top panel shows the entire dynamic range of the light curve and is binned with a resolution of 0.5 s in order to illustrate the bursting behavior. The light curve in the bottom panel is the same as the top, but has been rebinned to a resolution of 10 s and has been restricted along the y-axis in order to illustrate the behavior of the persistent emission. 40
- 4.2 Burst light curves along with their best-fit models and residuals. The observed light curves are shown in blue and have been plotted in logarithmic space, where the origin of the x-axis lies 10 s prior to the onset of the corresponding burst, in order to more clearly illustrate the burst structure. The left two panels correspond to Burst 1 and the right two panels to Burst 2. The top panels show the bursts fit to a simple FRED model described by Equation 4.1 and shown by the solid lines. The bottom panels show the bursts fit to more complex models. Burst 1 is fit to a sum of two FRED sub-bursts, the first of which is plotted as a dashed line and second of which is dotted. Burst 2 is modeled by adding a power law component at late times and is described by Equation 4.2. The dashed line shows the FRED component and the solid line shows the total model. Both bursts are described more accurately by their respective augmented models rather than by a simple FRED model. 42

- 4.3 Persistent and burst spectra and their best-fit models. The persistent spectra are shown on the left with FPMA in blue and FPMB in red. The solid lines show the best-fit reflection model, and the dashed lines shows the blackbody component, the Comptonized component, and the reflected cutoff power law component. The burst spectra are shown on the right with Burst 1 shown in orange and Burst 2 shown in green. For clarity, only the FPMA spectra are shown. The solid lines show the best-fit models which are dominated by the blackbody component which has been added to the persistent model. 44
- 4.4 Evolution of the blackbody component which describes the emission for each type-I X-ray burst. The apparent unabsorbed bolometric luminosity, temperature, and radius (assuming a distance of 7 kpc) of the blackbody are shown for Burst 1 on the left in orange and for Burst 2 on the right in green. The double-peaked structure of Burst 1 is observed in the intrinsic luminosity, confirming that it is not the result of the spectrum dropping below the NuSTAR bandpass. Burst 2 exhibits a PRE “touchdown” event a few seconds after burst onset in which the blackbody radius contracts rapidly while the temperature increases at constant luminosity. 49
- 5.1 2–4 keV and 4–10 keV light-curves (upper and middle panels) and their ratios (lower) of MAXI J1848–015 obtained with MAXI/GSC. Average fluxes in 1 scan (grey), 6 hours (black), and 1 day (red) are shown (1 scan data are omitted in the lower panel). The average 2–4 keV and 4–10 keV count rates for Crab are 1.065 and 1.172 $\text{ct cm}^{-2} \text{s}^{-1}$, respectively. The blue and green lines are the start and end time of the first and second NuSTAR observations, respectively. 64

- 5.2 Long-term 2–10 keV light-curve of MAXI J1848–015 from MAXI. Unused data during interference with the Space-X Crew-1 spacecraft are also shown in grey. A logarithmically rebinned curve and the best fitting curves are also shown in the inset panel. The data during a dip shown in grey are not used in the fits (see Section 5.2). Observed fluxes for the two NuSTAR and Swift observations are indicated with the red filled circle, rectangle, and triangle, respectively, between the dashed lines showing the observation periods. The orange line shown in the inset represents a linear fit to the initial rapid decay, while the blue and green lines represent exponential and power law fits, respectively, to the observed second decay. 65
- 5.3 Background-subtracted 3-78 keV NuSTAR light-curve for each of the two observations, NuObs 1 (left) and NuObs 2 (right). The light-curves have been split into different CHU combinations. Time is measured in seconds since the observation start times listed in Table 5.1. 67
- 5.4 Summed Mode 6 data (all CHU combinations) from NuObs 1. The color bar is shown in units of counts. The source landed on the gap between detectors, and due to poor image reconstruction, multiple peaks in the count distribution are apparent. The green circle, which has a radius of 1', represents the ASCA error region for source AX J184848–0129 as reported by Sugizaki, Mitsuda, et al. (2001). . . . 68
- 5.5 Soft state (blue) and hard state (orange) spectra with best fit models and model components shown with solid and dashed lines, respectively. FPMA spectra are shown with x's while FPMB spectra are shown with filled circles. The soft state spectrum is described well by a Comptonized disk blackbody, while the hard state spectrum does not require a disk component. Instead, the hard state spectrum is described well by a power law with a high energy cutoff. Both models are improved by the addition of relativistic disk reflection as well as a narrow Fe line component. The lower two panels show the residuals resulting from the model fits in units of $\chi = (\text{data} - \text{model})/\text{error}$ 70

5.6	Broad Fe emission profiles in the soft state (top) and hard state (bottom) spectra. These residuals were produced by fitting the spectra to a simplified continuum model while ignoring data points in the range 5 – 10 keV. Significant changes to the shape of the profile can be seen between the two states with the peak growing stronger and shifting to lower energies during the hard state.	70
5.7	Averaged cospectrum calculated for the hard state NuSTAR observation, NuObs 2, using only CHU12 data. The cospectrum has been rebinned for clarity. The best-fit power law is shown in red. We did not find evidence for QPOs or pulsations.	76
6.1	Leakage current measured in Charge Pump (CP) mode. Measurements were taken at 5° C with an applied voltage of 500 V. On the left we show the leakage currents for each pixel, and on the right we show the distribution of leakage currents. Outliers, shown in grey, have been omitted for clarity. We find relatively low leakage currents and good uniformity.	87
6.2	The channel-to-energy gain calculated for each activated pixel. We illuminated the full detector with an ^{241}Am source and determined the conversion from channel to energy by fitting the 59.54 keV line to a simple Gaussian. Left: Map of gain calculated for each pixel. Pixels deactivated due to bursting behavior are shown in grey. The five regions for which we produced spectra are enclosed in white squares. Right: Distribution of gain values across the detector. We find good uniformity aside from higher gain measured near the edges due to the guard ring.	89
6.3	Spectra measured for a ^{241}Am source (blue) and a ^{155}Eu source (orange) using a 5×5 pixel region using only single-pixel events. Several corrections, described in Section 6.3 have been applied. The FWHM of each singlet emission line is labeled with black arrows. . .	92

- 6.4 Fits to singlet emission lines in the spectra shown in Figure 6.3, transformed into logarithmic scale for legibility. Each line was fitted to the sum of a normal distribution, an exponential power law tail, a low-energy shelf, and a constant offset. These components are plotted as dashed lines while the full model is shown by the solid orange line. For each line, we also show the residuals to the model in the lower panels. The centroid of each line was determined via least-squares fitting to the model, and the FWHM (shown in black) was calculated from the resulting model. We achieve good resolution across the hard X-ray band, with particularly good performance at higher energies. 93
- 6.5 Spectra (top) and depth plots (bottom) measured for a ^{241}Am source (right) and a ^{155}Eu source (left) using a 5×5 pixel region using only single-pixel events. Several corrections, described in Section 6.3, have been applied to determine the energy of each event. The bottom panels show the distribution of the negative hole signal observed in pixels surrounding the central pixel in which the electron signal is observed. This acts as a proxy for the depth of interaction of an event, where events which lie near 0 on the y axis occurred near the top of the detector, with depth of interaction increasing as one follows the tracks downwards and to the left. By excluding events beyond a certain depth (shown by the red line with slope -0.01 hole signal/keV), energy resolution can be improved, especially at higher energies. 95
- 6.6 The fraction of total events which triggered more than one pixel, as a function of measured energy. Each line represents the multiple-pixel event fraction for a different depth cut slope (see Figure 6.5) between -10^{-5} and -0.1 . The shallower the slope, the more aggressive the depth cut. For a slope of -10^{-5} , all events included occurred near the top, or cathode, of the detector. 96
- 6.7 Spectra measured for a ^{241}Am source (blue) and a ^{155}Eu source (orange) using a 5×5 pixel region using single-pixel events as well as events for which two adjacent pixels were triggered. Several corrections, described in Section 6.3 and Section 6.4 have been applied. The FWHM of each singlet emission line is labeled with black arrows. 98

A.1	Distributions of selected parameters resulting from MCMC analysis of each spectrum individually, without joint fitting. The dashed lines shown in the one-dimensional histograms represent, from left to right, the 5%, 50%, and 95% quantiles, while the contours shown in the two-dimensional histograms represent confidence regions of increasing sigma. Top: soft state parameters. Bottom: hard state parameters.	118
A.2	Distributions of selected parameters resulting from MCMC analysis of the NuSTAR spectra with joint fitting where the parameters a , i , and A_{Fe} were tied between the soft and hard states. The dashed lines shown in the one-dimensional histograms represent, from left to right, the 5%, 50%, and 95% quantiles, while the contours shown in the two-dimensional histograms represent confidence regions of increasing sigma.	119
B.1	Electronic noise maps for two hybrids which suffered poor hybridization. High levels of noise can be seen across the majority of each detector, rendering them both unusable for scientific applications. In the ideal case, the electronic noise should be less than 1 keV and should show good uniformity across the detector.	120
B.2	Interpixel conductance maps for a hybrid which we determined to have suffered a failure in the application of epoxy during the hybridization process. The figure on the left shows the conductance in the horizontal direction, while the figure on the right shows the conductance in the vertical direction. Large regions of the detector were rendered unusable due to the high conductance between pixels.	120
B.3	SEM images of epoxy used to bond the CZT detector to the custom NuSTAR ASIC. On the left is shown an example of a failed bond, while on the right is shown a successful bond. It is clear from SEM imaging that the noisy batch of hybrids suffered from a failure in the application of epoxy which resulted in overflow onto the detector electronics. We inferred that this was the cause of the large-scale pixel failure observed in this batch of hybrids.	121

LIST OF TABLES

<i>Number</i>	<i>Page</i>
3.1 Results of the folding pulsation search for each epoch.	25
3.2 Values of spectral parameters determined by χ^2 fitting of observed spectra. Two models are shown: a fully covered power law with a Fermi-Dirac-like cutoff modeled by <code>fdcut</code> (top), and a partially covered power law with an exponential cutoff, modeled by <code>cutoffpl</code> (bottom).	30
4.1 light curve parameters for Bursts 1 and 2. Burst 1 is further broken down into sub-burst 1 and sub-burst 2. The top seven rows were determined via model fitting, while the bottom two rows were calculated based on the fitted parameters. The burst onset times, t_0 , are given relative to the start of the observation, $t_{\text{ref}} = \text{MJD } 58976.305553$	43
4.2 Spectral parameters determined by fitting the persistent spectra in Xspec. Model 1 corresponds to a Comptonized blackbody without disk reflection, Model 2 corresponds to relativistic disk reflection of an irradiating blackbody, and Model 3 corresponds to relativistic disk reflection of an irradiating cutoff power law.	45
4.3 Physical quantities calculated for the persistent emission, based on the non-reflection spectral model.	46
4.4 Comparison of PRE bursts presented in this work and in Barrière et al., 2015.	55
5.1 Log of NuSTAR observations presented in this paper.	66
5.2 Spectral parameters determined by performing a joint fit of the soft and hard state spectra in Xspec.	71
5.3 Timing properties of the source during each NuSTAR observation.	75
6.1 Spectral resolution measured for different regions in the detector.	90

NOMENCLATURE

- ADAF.** Advection-dominated Accretion Flow.
- ARF.** Ancillary Response Files.
- ASIC.** Application specific integrated circuit.
- BeXB.** Be X-ray Binary.
- BH.** Black Hole.
- BIC.** Bayesian Information Criterion.
- CHU.** Camera Head Unit.
- CZT.** Cadmium Zinc Telluride.
- DIM.** Disk Instability Model.
- FPMA/B.** Focal Plane Module A/B.
- GTI.** Goodtime Interval.
- HEX-P.** High Energy X-ray Probe.
- HMXB.** High Mass X-ray Binary.
- LMXB.** Low Mass X-ray Binary.
- MAXI.** Monitor of All-sky X-ray Image.
- NS.** Neutron Star.
- NuSTAR.** Nuclear Spectroscopic Telescope Array.
- PRE.** Photospheric Radius Expansion.
- QPO.** Quasiperiodic Oscillation.
- RMF.** Response Matrix Files.
- SgXB.** Supergiant X-ray Binary.
- ULX.** Ultraluminous X-ray Source.
- ULXP.** Ultraluminous X-ray Pulsar.
- XRB.** X-ray Binary.

Chapter 1

AN INTRODUCTION TO X-RAY BINARIES

The primary goal of my thesis work has been to study accreting compact objects across a range of mass accretion rates, with a focus on accreting neutron stars (NS). Let us start therefore with an introduction to the physics and observable properties of accreting compact objects in general, then turn our attention towards NS accretors in particular and the range of phenomena that arise due to differences in accretion rates.

1.1 A brief overview of disk accretion

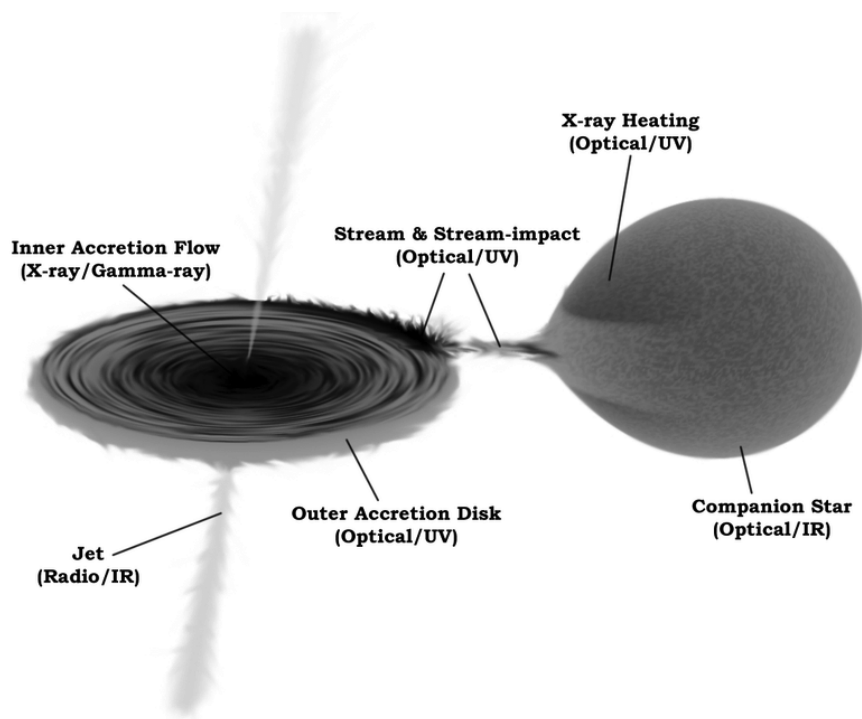


Figure 1.1: Figure from Hynes (2010) showing an artistic representation of a compact object accreting via Roche lobe overflow. Each of the physical regions of the binary system are labeled with the electromagnetic bandpass corresponding to the majority of their emission. NuSTAR primarily observes the innermost regions of the accretion disk thanks to its hard X-ray sensitivity.

X-ray binaries (XRBs) represent one of the most important physical laboratories

in the universe for studying complex interactions between matter, light, gravity, and magnetic fields. These systems are formed when a compact stellar remnant, such as a NS or a stellar mass black hole (BH), accretes material from a main sequence or supergiant companion star, resulting in the formation of an accretion disk which transforms gravitational potential energy into electromagnetic radiation with staggering efficiency. These systems are generally broken down into two categories: low mass X-ray binaries (LMXB) with companion masses $\lesssim 2.5M_{\odot}$ and high mass X-ray binaries (HMXB) with companion masses $\gtrsim 6M_{\odot}$.

The channel by which the companion star donates material to the compact object depends on the radius of the companion star, the mass ratio, q , of the companion to the compact object, and the binary separation. As the companion evolves, and its radius increases, it may eventually fill its Roche lobe — the equipotential surface within which material is gravitationally bound to the star. When this occurs, material begins to flow off the surface of the companion, passing through Lagrange point L1 and falling into orbit around the compact object.

Alternatively, a compact object may accrete from a companion which does not fill its Roche lobe via capture of stellar winds. This accretion channel, also known as Bondi-Hoyle-Lyttleton after the work of Bondi and Hoyle (1944) and Hoyle and Lyttleton (1939), may even account for the majority of low-luminosity X-ray binaries in our galaxy (Pfahl, Rappaport, and Podsiadlowski, 2002). For a review of wind-fed accretion see Edgar (2004).

Material which has fallen into orbit around the central compact object circularizes, and internal friction carries angular momentum from the inner regions of accreting material outwards, causing the material to spiral inwards towards the compact object, forming an accretion disk. The standard model of disk accretion was first laid out by Shakura and R. A. Sunyaev (1973). As material falls inward, gravitational energy is converted into kinetic and thermal energy, and the latter is radiated as blackbody emission. The temperature and luminosity of the disk both depend on the rate of accretion, \dot{M} , which in turn depends on the efficiency of angular momentum transport as well as the rate of mass loss from the companion. At high accretion rates, the disk may reach temperatures on the order 10^7 K, corresponding to photon energies of ~ 1 keV, placing accretion disk emission in the X-ray band. A schematic view of an XRB accreting via Roche lobe overflow is shown in Figure 1.1 reproduced from Hynes (2010). In addition to X-ray emission from the innermost regions of the disk, XRBs may also emit radiation in the radio, infrared, optical, UV, and

gamma-ray bands, making multi-wavelength observation campaigns an important tool for studies of accreting systems.

1.2 Observational properties of X-ray Binaries

Accreting compact objects exhibit myriad energetic phenomena across the X-ray band and over a wide range of timescales. Their spectra are generally described by a combination of a multicolor disk blackbody with a maximum temperature between 0.1-1 keV as well as a power law component which originates from a region of hot plasma known as the corona, the geometry of which and the mechanism by which it is powered are not currently well understood. The spectral index of the power law component may vary in the range $\Gamma = 0.5 - 2.0$, and can therefore extend into the hard X-ray band. The power law component may also exhibit a high-energy cutoff, meaning that the spectrum begins to drop off more rapidly in intensity beyond a certain energy, which is typically above 10 keV. In the case of a NS accretor, an additional continuum spectral component is often present in the form of a single-temperature blackbody originating from the the surface of the accreting star, or the boundary layer where accreting material slows down to match the rotational velocity of the NS. The spectrum of the supergiant X-ray binary SMC X-1, which I present in Chapter 3, exhibits many of the features described above including two blackbody components, attributed to the disk and the NS surface, as well as a power law with a high-energy cutoff.

XRB spectra and relativistic disk reflection

In addition to the thermal and power law continuum components described above, XRB spectra also exhibit emission and absorption features which can help to illuminate physical properties of the source such as accretion geometry, disk ionization, BH spin, or NS magnetic field strength. Narrow absorption lines may be indicative of the presence of a disk wind driven by radiation pressure; discrete cyclotron energy levels in strong magnetic fields may produce broader absorption features at energies above 10 keV; material in the disk may fluoresce, producing prominent emission features in the spectra of XRBs.

One of the most common emission features present in the X-ray spectra of accreting compact objects is fluorescent emission of Fe $K\alpha$ between 6.4 and 7 keV. This emission is produced by the irradiation of the inner regions of the disk by the corona, the surface of an accreting NS, or even thermal disk emission which returns to the disk due to light bending in the strong gravitational field near an accreting

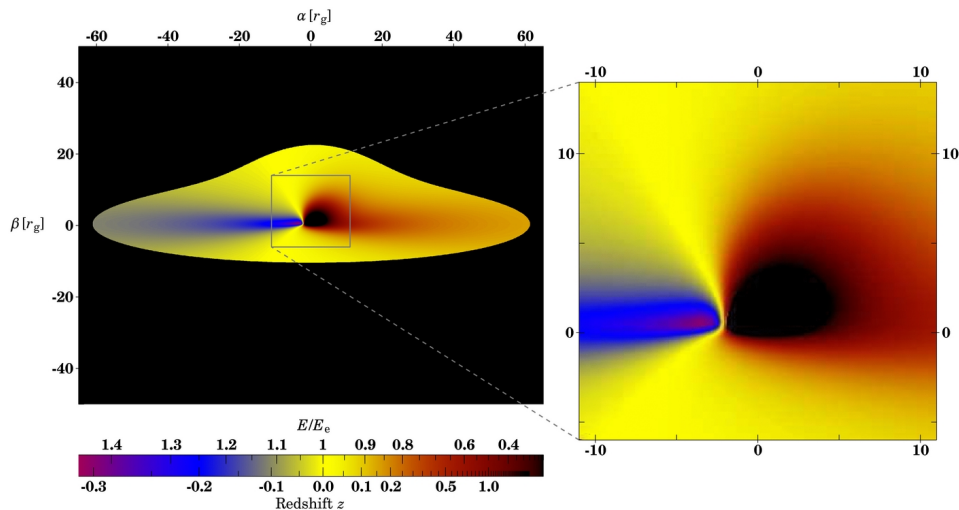


Figure 1.2: Figure from J. García, T. Dauser, Lohfink, et al. (2014) mapping the energy shift of photons from an accretion disk with inclination $i = 80^\circ$ around a maximally spinning black hole as seen by a distant observer.

BH. Because the fluorescent emission originates from the inner regions of the accretion disk, nearest the compact object where the fluorescing radiation field is most intense, the otherwise narrow Fe emission lines may be warped and broadened by gravitational redshifting as well as relativistic beaming and blueshifting due to rapid orbital velocities in the accretion disk. These effects are illustrated in Figure 1.2 reproduced from J. García, T. Dauser, Lohfink, et al. (2014), which shows the energy shift of photons originating from an accretion disk with inclination $i = 80^\circ$ around a maximally spinning black hole as seen by a distant observer. This warping of otherwise narrow emission lines, as well as the “Compton hump” at higher energies due to Compton upscattering of soft photons, are the telltale spectral features associated with relativistic disk reflection. Physical modeling of these spectral features using models such as `relxill` (J. García, T. Dauser, Lohfink, et al., 2014; T. Dauser et al., 2014), has proven to be a powerful tool for understanding accreting compact objects thanks to their ability to probe the regions closest to stellar mass BHs and NSs.

In particular, these models are sensitive to the angular momentum, J , of the compact object, parameterized as $a = cJ/GM^2$ where M is the mass of the compact object. The spin may take on values in the range $-1 < a < 1$, where negative values indicate that the spin is retrograde with respect to the disk rotation, while positive values

are prograde. Relativistic disk reflection models can also be used to measure the inner disk radius, R_{in} , or the radius of the innermost orbit in the accretion disk. Due to general relativistic deviations from classical gravity near the compact object, the inner disk radius has a physical lower limit at the innermost stable circle orbit, $R_{\text{ISCO}} = 6R_g \equiv 6GM/c^2$ for a Schwarzschild (non-spinning) BH, but can extend all the way down to $1R_g$ for a maximally spinning BH as frame dragging effects lead to stabilization of otherwise unstable orbits. Measuring these parameters can be key to a number of physical questions regarding the formation and growth of BHs (Christopher S. Reynolds, 2021), the equation of state for NSs (Ludlam et al., 2022), and the truncation of accretion disks (Xu et al., 2020). Additionally, as I show in Chapter 5, relativistic disk reflection modeling can be useful for identifying whether a given XRB harbors a BH or a NS.

Variability over many timescales

While some XRBs are persistent in terms of their luminosity and spectral states, transient XRBs undergo drastic variability in these states as their mass accretion rates vary. This variation may be due to evolution of the companion star, periodic changes in binary separation for eccentric orbits, or due to the instability in the rate of accretion in the disk.

According to the Disk Instability Model (DIM; Lasota, 2001), the efficiency of angular momentum transport within the disk depends upon the density of the accreting material. Thus, at low densities, mass accretes onto the compact object slowly, resulting in a cool, low-luminosity disk. In BH XRBs, this corresponds to the low hard spectral state, as the spectrum is dominated by hard X-ray emission from the corona. As material from the companion star continues to accumulate in the disk, the disk density increases. At a critical density, the ionization of the accreting material changes rapidly, increasing the efficiency of angular momentum transport, and therefore speeding up accretion onto the compact object. At this point radio emission may demonstrate evidence for jet-like outflows from the central accretor. As the accretion rate increases, the disk heats up and the corona is cooled via Compton scattering, resulting in a spectrum which is dominated by soft thermal emission. Therefore this state is referred to as the high soft state for BH XRBs. Over a timescale of weeks to months, the disk “drains,” eventually returning to the slowly accreting low hard state. Observational properties, such as spectral hardness and intensity, associated with different stages of this cycle of outburst are shown in Figure 1.3 reproduced from R. P. Fender, T. M. Belloni, and Gallo (2004).

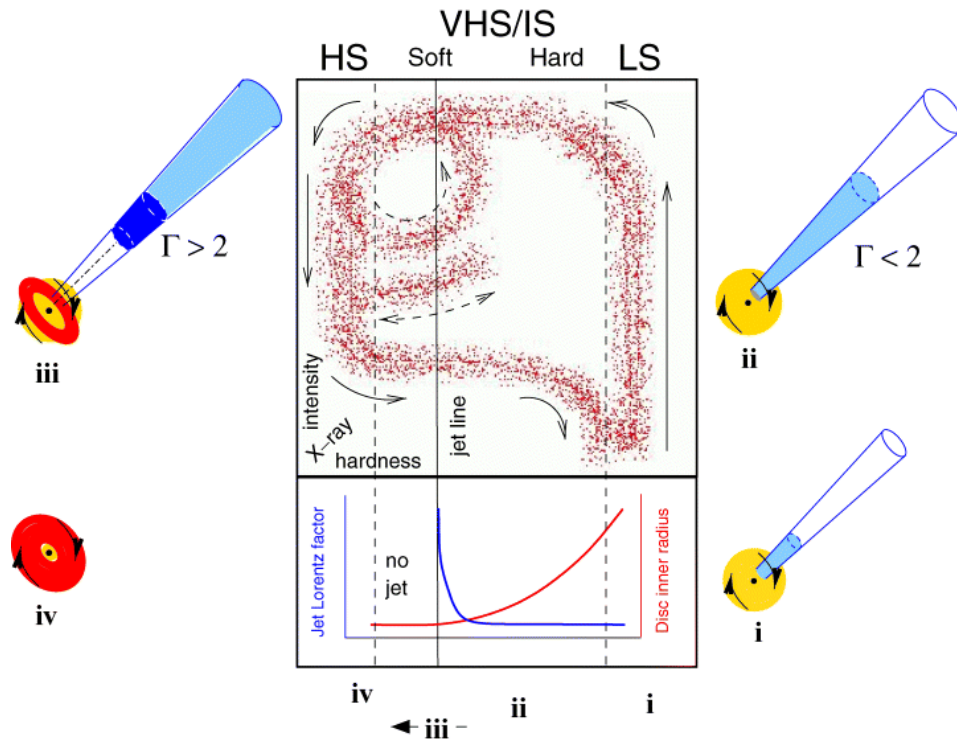


Figure 1.3: Figure from R. P. Fender, T. M. Belloni, and Gallo (2004) illustrating the cycle of accretion states exhibited by many accreting black holes. The top panel shows a schematic of the hardness (the fraction of hard X-ray photons to soft X-ray photons) on the x-axis vs. intensity on the y-axis, while the bottom panel plots the disk and jet properties in different states. These states are also shown as illustrations on the left and right hand sides of the figure with the jet shown in blue, the disk shown in red, and the corona shown in yellow. A typical outburst of a black hole X-ray binary begins in the bottom right corner of the top panel, and traverses the hardness-intensity diagram in the counterclockwise direction, following the arrows shown. The source may remain in outburst for months at a time.

On similar timescales, XRBs may vary in apparent flux due to orbital and super-orbital modulation. The long-term light-curve of SMC X-1 discussed in Chapter 3 demonstrates the former, in the form of eclipses, and the latter in the form of a superorbital period which varies between 45-60 days. While orbital modulation is straightforward in its physical origin, superorbital modulation is not as easily explained. A number of HMXBs exhibit such long-term variability, which is often attributed to precession of the accretion disk due to radiation-induced torque (Clarkson et al., 2003; Charles et al., 2008).

On much shorter timescales, NS XRBs may exhibit coherent oscillations in flux with frequencies anywhere between 10^{-3} Hz and 10^3 Hz corresponding to the rate of rotation of the NS itself. These pulsations often arise due to the interaction of the NS magnetic field and the accreting material. In the simple picture, the dipolar magnetic field of a NS threads the surrounding accretion disk, and we may define a quantity known as the “magnetospheric radius,” roughly defined as the radius at which the ram pressure of the accreting material is balanced by the pressure of the magnetic field. At this radius, the accretion flow is disrupted. If the magnetospheric radius falls outside of the corotation radius, at which the accreting material orbits with the same angular velocity as the rotating NS, then material may be ejected from the system by the rapidly rotating magnetic field via the so-called “propeller effect” (Illarionov and R A Sunyaev, 1975). In this case, angular momentum is removed from the NS and its rotation frequency decreases. On the other hand, if the magnetospheric radius falls within the corotation radius then material is funneled by the magnetic field lines onto the surface of the NS, depositing angular momentum and increasing the spin frequency of the NS. As material falls onto the magnetic poles of the rotating NS, it produces excess emission in the form of a hotspot or an extended column of accreting material, and the periodic passing in and out of line of sight of this emitting region produces a pulsating lighthouse effect from the point of view of a distant observer. For a recent review of the theoretical considerations of accretion onto magnetized NSs, see Lai (2014).

Other forms of variability on short timescales include quasiperiodic oscillations (QPO) which may occur in both BH and NS XRBs, and type-I X-ray bursts, which only occur in NS XRBs. Type-I bursts, which I discuss in more detail in Chapter 4, occur when accreting material builds up on the surface of a NS, eventually reaching a critical density and triggering runaway thermonuclear burning. This burning rapidly envelopes the NS surface, resulting in a dramatic increase in brightness which lasts

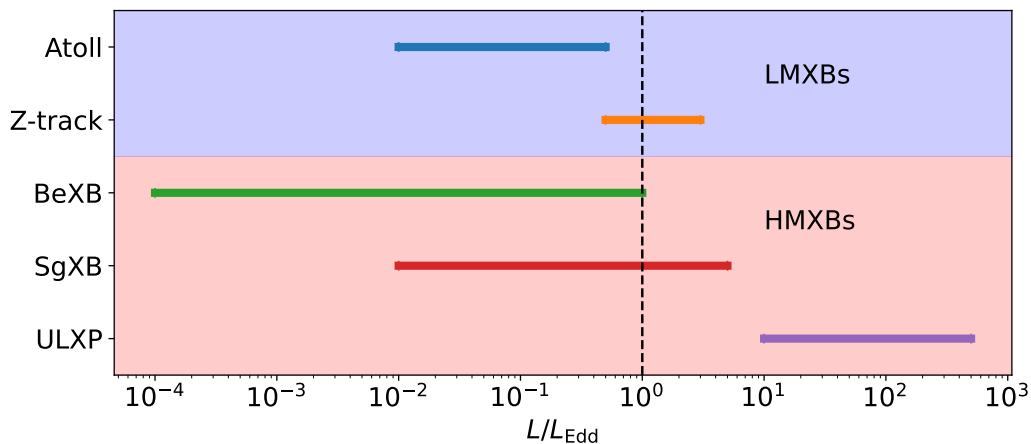


Figure 1.4: The approximate ranges of Eddington fractions, corresponding to accretion rates, of different classes of NS XRB. Atoll and Z-track sources have low-mass companions, while BeXBs, SgXBs, and at least some ULXPs have high-mass companions. The vertical dashed line denotes the Eddington limit itself. Some NS XRBs move between periods of quiescence and periods of outburst, leading to a wide range of observed accretion rates. Each class exhibits unique behavior which evolves depending upon the mass accretion rate.

tens to hundreds of seconds. These events may yield a plethora of information regarding the accreting NS, including the distance to the source, the composition of the burning material, and the NS spin frequency (Duncan K. Galloway and Laurens Keek, 2021).

1.3 Neutron star X-ray binaries over a range of accretion rates

The observational astrophysics portion of my thesis focused broadly on the study of XRBs at differing accretion rates, with the aim of studying NS XRBs in particular. Just as individual sources may vary in their rates of accretion as they undergo periods of quiescence and outburst, as a class NS XRBs vary in accretion rates depending on their orbits and the properties of their companions, and the observable properties of these systems exhibit startling diversity across this range of accretion rates. Because the luminosity of an accreting source is proportional to its accretion rate — modulo absorption, beaming, and other distorting effects — we may use luminosity as an indicator of accretion state:

$$L = \eta \dot{M} c^2 \quad (1.1)$$

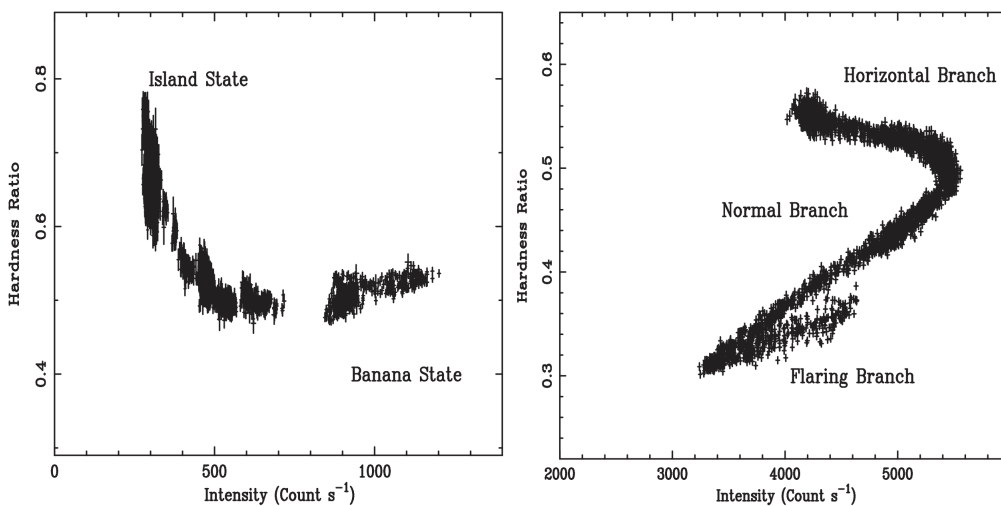


Figure 1.5: Figure from Church, Gibiec, and Bałucińska-Church (2014) showing the hardness-intensity diagrams of prototypical Atoll (left) and Z-track (right) sources 4U 0614+091 and GX 340+0, respectively. Both classes of NS LMXB move between different accretion states defined by their positions on these tracks.

where \dot{M} is the mass accretion rate and η is the efficiency of gravitationally energy release which typically has a value of around 10%. The masses of NSs found in XRBs are rarely known to great precision, but they occupy a narrow range of allowed masses, $1-2M_{\odot}$. Therefore, comparison of luminosities between NSs is relatively straightforward, particularly when written in terms of the Eddington luminosity, L_{Edd} . This is the luminosity (and therefore accretion rate) at which radiation pressure balances gravitational force, thereby halting accretion. For a NS this limit is about $2 \times 10^{38} \text{ erg s}^{-1}$. Several classes of NS XRB, which I discuss below, are listed in Figure 1.4 along with their ranges of observed luminosities with respect to the Eddington limit.

NS systems with low-mass companions ($\lesssim 2.5 M_{\odot}$) can be roughly subdivided into two classes: Atoll sources and Z-track sources. These are so named due to the tracks they trace out when their intensities are plotted with respect to their hardness ratio, or the fraction of high-energy counts to low-energy counts. Two such tracks are shown in Figure 1.5, which has been reproduced from Church, Gibiec, and Bałucińska-Church (2014). Atoll sources spend much of their time in the low-luminosity “island” state, and trace out a signature “banana” state during outbursts, whereas

Z-track sources move more rapidly between the so-called horizontal, normal, and flaring branches likely corresponding to continuous changes in accretion rate (M. van der Klis, 1989; Church, Gibiec, and Bałucińska-Church, 2014). Atoll sources tend to have lower luminosities, in the range $0.01L_{\text{Edd}} - 0.5L_{\text{Edd}}$, while Z-sources are brighter, approaching and sometimes moderately exceeding their Eddington luminosities. Both of these sources may exhibit type-I X-ray bursts (e.g. Kuulkers, M. van der Klis, and J. van Paradijs, 1995; Zhang, Méndez, and Altamirano, 2011), particularly in their lower-luminosity branches when accretion rates are low enough such that accreted material burns unstably.

These systems rarely exhibit strong pulsations, indicating that they are not highly magnetized, and making the measurement of their spin periods difficult. However, a number of LMXBs have shown millisecond oscillations during type-I X-ray bursts which has been attributed to their rotation (Watts, 2012). Due to their low inferred magnetic fields and rapid rotation, it is believed that these sources have been spun up by long periods of accretion and likely represent the progenitors of the millisecond pulsars observed by radio telescopes.

High mass XRBs harboring accreting NSs with companions of mass $\gtrsim 6M_{\odot}$ exhibit very different properties than their low mass counterparts. This class of binary system may similarly be further subdivided into supergiant XRBs (SgXB) and Be XRBs (BeXB) depending on whether the companion is a supergiant star or an OBe star, respectively. BeXBs are often transient, exhibiting low-luminosity ($L = 10^{-4} - 10^{-3}L_{\text{Edd}}$) persistent states which may be punctuated by type-I X-ray bursts as well as longer periods of outburst when the NS passes through periastron and forms a transient accretion disk. During such outbursts, BeXBs may reach their Eddington luminosities. In addition to having eccentric orbits, BeXBs also tend to have high magnetic fields ($B \sim 10^{12}G$), pulse periods on the order of several to thousands of seconds, and orbital periods of tens to thousands of days (Reig, 2011).

Due to their large binary separations, the vast majority of SgXBs accrete via stellar winds rather than Roche-lobe overflow leading to disk accretion. As a result, these systems tend to persistently accrete at an Eddington fraction of around 1% , although some, known as Supergiant Fast X-ray Transients (SFXT), only reach this luminosity during sporadic flares which punctuate periods of persistent emission at much lower luminosities (Hainich et al., 2020). A handful of SgXBs reach much higher accretion rates, even exceeding their Eddington limits by factors of a few. These accretion rates are achieved by disk accretion rather than Bondi-Hoyle-Lyttleton accretion, and

the high luminosities that result can induce disk warps which lead to superorbital modulation. SgXBs exhibit pulsations with periods very similar to those observed in BeXBs, but they tend to have shorter orbital periods in the range 1-10 days (Reig, 2011).

While the Eddington luminosity is meant to represent a rough limit on the allowed rate of accretion, in 2014 M. Bachetti et al. (2014) discovered the first ultraluminous X-ray source (ULX) known to harbor an accreting NS. ULXs are X-ray binaries defined primarily by their high luminosities, $L > 10^{39}$ erg s⁻¹, and they are notorious for their relatively featureless spectra which do not easily reveal the nature of the accreting object. Due to their high luminosities, however, they were long assumed to harbor black holes, whose higher masses compared to NSs would allow for higher Eddington limits. However, pulsation searches have now revealed a number of ultraluminous X-ray pulsars (ULXPs) which can only be NSs (e.g. F. Fürst et al., 2016; G. L. Israel et al., 2017; Gian Luca Israel et al., 2017). The luminosities of these sources push the limits of the imagination, reaching hundreds of times their Eddington limits in the most extreme cases. A number of theoretical explanations have been proposed to explain such high apparent accretion rates, including beaming and high magnetic field effects. These sources therefore represent an important new laboratory for understanding the physics of accretion onto compact objects. However, there are no known sources in our galaxy, making ULXPs difficult to study without long exposure times. Finding nearby analogues with which to compare them will be an important step to better understanding these extreme sources.

Determining the nature of a given XRB can pose some difficulty. We may employ a number of different tools to ascertain whether an X-ray binary actually contains an accreting NS rather than a BH, as well as to estimate the mass of the companion star from which the compact object accretes. One of the primary characteristics distinguishing a NS from a BH is the existence of a stellar surface onto which material accretes. Thus, evidence of this surface, for example in the form of pulsations or type-I X-ray bursts, acts as solid evidence that the source is a NS. The presence or absence of this surface may also be indirectly inferred via studies of XRB spectra, quiescent luminosities, and the extents of their inner disk radii. We may also rely on more circumstantial evidence, comparing a source's spectral and timing properties to those of the known population of LMXBs and HMXBs, in order to infer the natures of the accretor and the companion composing an XRB. There are currently hundreds of known NS XRBs in our galaxy, which may be found in both HMXB

and LMXB systems (Reig, 2011).

Additionally, BHs have higher masses than NSs, which are physically restricted to masses below about $3 M_{\odot}$ (Kalogera and Baym, 1996) and typically have masses in the range $1 - 2 M_{\odot}$. Therefore, whereas the detection of pulsations or type-I X-ray bursts proves beyond a doubt that an XRB hosts a NS accretor, a mass measurement significantly above $3 M_{\odot}$ is required to confirm with certainty the presence of an accreting BH. Measurement of the accretor mass and the companion mass require knowledge of the orbital parameters of the binary system, which are not always readily available. These dynamical mass measurements may be obtained via a few different routes, such as by the study of variable absorption features or of eclipses in the case of high-inclination systems. Among about 70 candidate BH XRBs, the majority of which reside in LMXBs, 20 have been dynamically confirmed (Corral-Santana et al., 2016).

In this dissertation, I present studies of three accreting compact objects at different accretion rates which I was able to see to fruition and which have each been accepted for publication. The first, presented in Chapter 3, is a study of the supergiant XRB, SMC X-1, which hosts a NS accreting via Roche lobe overflow thereby reaching luminosities at or above its Eddington limit. I investigated the superorbital modulation of the source and characterized the evolution of its pulsations and its spectrum in order to illuminate the physical mechanism responsible for the superorbital period and suggesting the source as a nearby analogue for more distant (and therefore more difficult to observe) ULXPs. Moving to lower accretion rates, in Chapter 4, I present a study of the NS LMXB GRS 1741.9–2853. The source is a known type-I X-ray burster, and I proposed NuSTAR observations which caught two bursts. Each exhibited unique behavior, which I investigated via timing and spectral analyses. I was thus able to measure the distance to the source, and to infer the composition of the material which was burned during the bursts. Finally, in Chapter 5, I present an investigation of a newly discovered XRB. The nature of the accreting compact object was unknown at the time of discovery, but its luminosity was exceptionally low, making it a good candidate for the study of NS accretors with low accretion rates. I analyzed its spectral and timing properties, specifically harnessing the power of relativistic disk reflection spectroscopy, in order to determine whether the system hosted a NS or BH, and to make other important measurements of its physical properties.

All of these analyses were performed using data collected by the Nuclear Spectro-

scopic Telescope Array, or NuSTAR (Harrison et al., 2013), which when it launched in 2012 was the world's first high-energy X-ray telescope to utilize focusing optics in order to image the hard X-ray sky. In order to complement my astronomical research, I have also pursued instrumentation projects which have led me to develop a deeper understanding for the operation of NuSTAR and other X-ray telescopes. In the subsequent chapter, I discuss the various instruments used to study XRBs and other sources, and I describe NuSTAR in more detail in order to introduce the instrumentation work which I have included as part of my dissertation.

Chapter 2

INSTRUMENTATION FOR THE STUDY OF HARD X-RAYS

Due to the wide variety of astrophysical phenomena that arises from accretion in XRBs, as well as the myriad other X-ray sources in the universe, there exist a variety of instruments with which astronomers observe the X-ray sky. The goals of a particular instrument influence the choice of detector design and materials. The Advanced CCD Imaging Spectrometer (ACIS) on board the Chandra X-ray Observatory is composed of silicon charge-coupled devices (CCD) which produce images with sharp spatial resolution, and Chandra's High Resolution Camera (HRC) utilizes a pair of lead-oxide microchannel plates to achieve a large field of view and low-energy sensitivity (Weisskopf et al., 2000a). XMM-Newton's European Photon Imaging Camera (EPIC; Turner et al., 2001; Strüder et al., 2001) and the X-ray Telescope (XRT) on board the Neil Gehrels *Swift* Observatory (Burrows et al., 2005a) similarly utilize silicon CCDs to achieve good spectral and timing resolution in the soft X-ray band. Silicon detectors like these are generally effective for detecting photons with energy in the range 0.1 – 10 keV.

While observations of soft X-rays are able to probe thermal emission, absorption features, and Fe fluorescence features in order to provide a detailed picture of accreting compact objects and other X-ray sources, instruments which can observe photons with energy far beyond 10 keV play an important role as well, filling in gaps in our understanding of the X-ray sky which cannot be addressed using only soft X-rays. Measurements up to and beyond 100 keV are crucial for studying such astrophysical phenomena as Compton upscattered emission in the hard X-ray band, and cyclotron resonance scattering features appearing in the hard X-ray spectra of accreting NSs due to their strong magnetic fields. Additionally, hard X-ray observatories can provide a closer look at the spin periods and accretion properties of highly magnetized NSs by tracking their pulsations, which often increase in flux fraction at higher photon energies. Such is the case for ULXPs, representing a relatively new and under-studied exotic class of X-ray source which require hard X-ray observations for adequate study of their spectral properties as well.

2.1 A brief history of hard X-ray observatories

While soft X-ray observatories largely utilize silicon detectors in the form of CCDs or solid state silicon drift detectors, hard X-ray observatories have historically used proportional counter arrays (PCA) or crystal scintillators in order to achieve good sensitivity above 10 keV. PCA detectors consist of chambers of high-Z gas which are ionized by the interaction of incoming X-rays. A voltage is applied across the chamber such that the resulting cascade of liberated electrons are accelerated towards the anode for readout. The energy of the interacting photon can then be inferred from the amount of charge collected. Scintillators on the other hand consist of a clear gas or crystal such as sodium iodide which absorb X-rays and re-emit the incoming radiation in a flash of visible light. Photomultiplier tubes then amplify the intensity of this flash and the intensity is registered. The energy of the incoming photon may be determined according to the brightness of the measured flash of visible light.

The very first space-based X-ray telescope, Uhuru, launched in 1970, scanned the X-ray sky in the 2-20 keV range using PCA detectors. This was a tremendous leap for astronomy, as the pioneering observatory discovered the first black hole and cataloged hundreds of X-ray sources, many of which continue to be important sources for the field. Later the European X-ray Observatory Satellite (EXOSAT) probed X-rays with higher energies — up to 80 keV — using xenon and argon scintillators. Reaching even further, the High Energy X-ray Timing Experiment (HEXTE) aboard the Rossi X-ray Timing Explorer (RXTE) combined a PCA and an array of 8 NaI/CaI crystal scintillator detectors in order to achieve an observable energy range of 2-250 keV until it ceased science operations in 2012.

More recently, solid state crystal semiconductor detectors have allowed for improved spatial and spectral resolution in the hard X-ray band. Pixelated electrodes may be imprinted on these crystals with small pixel pitch, allowing for the over-sampling of high-resolution images produced by advanced grazing-incidence-angle optics. Cadmium Zinc Telluride (CZT) has proved to be a particularly suitable candidate for semiconductor X-ray detectors. In addition to the high atomic numbers of the constituent elements, CZT has a high electron mobility which aids in charge collection, as well as a band gap of a few eV which leads to low leakage, or “dark,” current. This means that CZT detectors may be operated at or near room temperature without significant degradation of spectral resolution, compared to germanium detectors which require cooling using liquid nitrogen in order to perform observations suitable

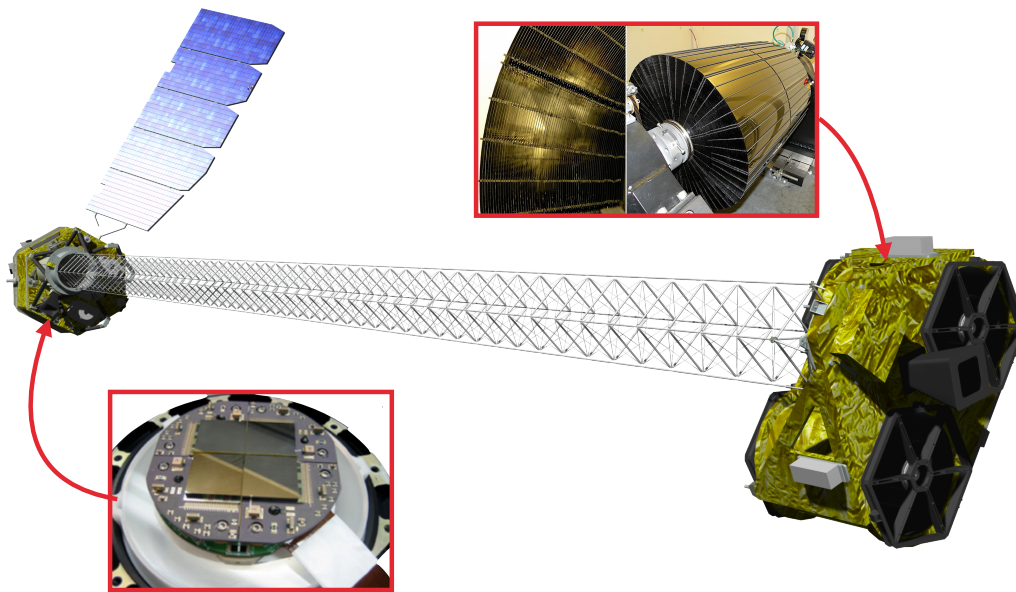


Figure 2.1: Rendering of NuSTAR with insets showing a focal plane module made up of 4 NuSTAR hybrids on the left and the Wolter grazing incidence angle optics on the right.

for scientific analysis. Additionally, CZT crystal can be produced with a relatively high production yield and uniformity.

2.2 NuSTAR: the Nuclear Spectroscopic Telescope Array

CZT detectors are currently being utilized by a number of space-based observatories, including the *Swift* Burst Alert Telescope (BAT) (Barthelmy et al., 2005) and the CZT Imager aboard AstroSat (Singh et al., 2014). Cadmium Telluride (CdTe), which shares many of the same qualities as CZT, has also been utilized by instruments such as the *Imager on Board the Integral Satellite* (IBIS) and the Hard X-ray Imager (HXI) on board the Hitomi observatory. The first focusing hard X-ray observatory was the Nuclear Spectroscopic Telescope Array, or NuSTAR (Harrison et al., 2013). NuSTAR consists of two separate focal plane modules, FPMA and FPMB, each of which is paired with a parabolic Wolter optics module (Wolter, 1952) with a focal length of 10 m in order to image the X-ray sky in the 3-79 keV band. Figure 2.1 shows a render of NuSTAR, with insets showing the Wolter optics on the right and an example FPM on the left. Each FPM consists of four CZT “hybrids,” produced by flip-chip bonding a custom application specific integrated circuit (ASIC) with

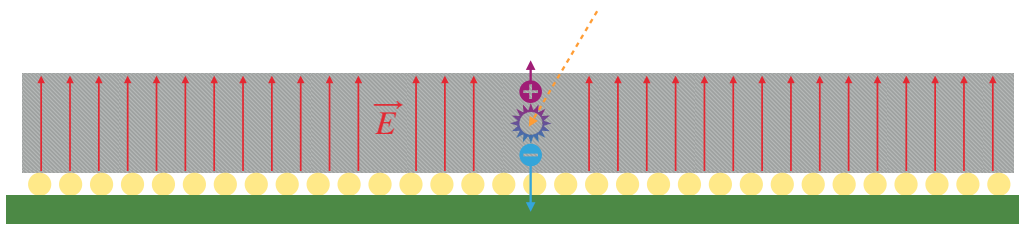


Figure 2.2: Schematic showing a sideways cross-section of a NuSTAR hybrid, made up of a CZT crystal shown in grey, 32 stud bumps in gold, and readout electronics in green, interacting with an incoming photon shown as an orange dashed line. When a photon interacts with the detector, it produces a cloud of liberated electrons (blue) and a positively charged hole cloud (purple). An electric field, \vec{E} shown in red, is applied across the detector, causing the electron cloud to drift towards the anode and the hole cloud towards the cathode. In CZT, electrons move more freely than holes, meaning the signal measured due to the motion of electrons is stronger than that of the motion of the hole cloud.

32×32 pixels to a CZT crystal with dimensions $2 \text{ cm} \times 2 \text{ cm} \times 2 \text{ mm}$. On the top of the crystal is printed a uniform cathode, while on the electronics side of the crystal is printed a pixelated anode pattern corresponding to the pixelated ASIC. Accordingly, each pixel of the detector has a pitch of $\sim 600 \mu\text{m}$.

When a photon interacts with the CZT detector, it liberates an inner-shell electron, which in turn causes a cascade of liberated electrons. The result is an unbound electron cloud and a corresponding cloud of positively charged holes. An electric potential of several hundred volts is applied between the cathode and the pixelated anode such that the electron cloud drifts towards the anode and the hole cloud towards the cathode. Figure 2.2 shows a schematic representation of a NuSTAR hybrid in cross-section and illustrates the interaction of a photon with the CZT crystal. Rather than simply collecting the liberated electrons, NuSTAR detectors operate according to the Shockley-Ramo Theorem (Shockley, 1938; Ramo, 1939) whereby charge is induced on the detector anode due to the motion of charges across the electric potential in the bulk of the semiconductor. In particular a larger change in potential traversed by a cloud of charge corresponds to a larger signal measured by the detector electronics. In the case of a pixelated detector architecture in which the pixel pitch is much smaller than the detector thickness, the potential gradient is steepest near the anode, meaning that the electrons, rather than positively charged

holes, contribute much more strongly to the measured signal (Barrett, Eskin, and Barber, 1995). This effect, known as the “small-pixel effect,” along with lower hole mobility compared to electron mobility, combine to produce spectral resolution on the order of one percent in pixelated CZT detectors like the NuSTAR hybrid.

2.3 The future of high energy X-ray astronomy

Focused hard X-ray astronomy of the kind that NuSTAR is capable has proven an invaluable tool for the field. The unique combination of spectral, timing, and imaging capabilities up to 79 keV has made possible the discovery and study of ultraluminous X-ray pulsars (ULXP), which proved that NS accretors can reach luminosities far in excess of their Eddington limit (e.g. M. Bachetti et al., 2014). Additionally, NuSTAR’s sharp spectral resolution across the Fe $K\alpha$ complex, combined with its sensitivity to Compton reflection features above 10 keV have made it a very successful tool for studies of relativistic disk reflection (e.g. J. A. García, John A. Tomsick, et al., 2019; Lazar et al., 2021; Connors, J. A. García, J. Tomsick, et al., 2021). Indeed NuSTAR has been central to my own thesis work, allowing me to probe the pulsations of accreting NSs, to track the rapidly evolving spectra arising from type-I bursts, and to measure the rapid spins of black holes. However, after the NuSTAR mission ends, the community may be left without a focusing hard X-ray observatory. The mission concept High Energy X-ray Probe (HEX-P) is poised to fill this gap (K. K. Madsen, Stern, and HEX-P Team, 2019).

HEX-P will inherit much of the technology and design which has made NuSTAR such a powerful scientific instrument. Like NuSTAR, it will combine grazing incidence angle optics with high-Z semiconductor detectors. With improved optics, pixel design, and crystal properties, it will achieve a bandpass of 2-200 keV, extending NuSTAR’s sensitivity in both the soft and hard X-ray regimes. The HEX-P focal plane will be composed of NuSTAR-like hybrids with four times the collecting area (see Figure 2.3 for a conceptual schematic of the focal plane module).

In order to prepare for future missions such as HEX-P, it is crucial to understand the capabilities of various semiconductor detector materials available for purchase. NuSTAR utilizes CZT from eV Products, which no longer provides CZT suitable for our purposes. Therefore, we have purchased CZT from Redlen Technologies in order to determine the uniformity, spectral resolution, and yield we can expect from currently available CZT. In Chapter 6, I present a study of newly purchased CZT material from Redlen Technologies and its characteristics when paired with the

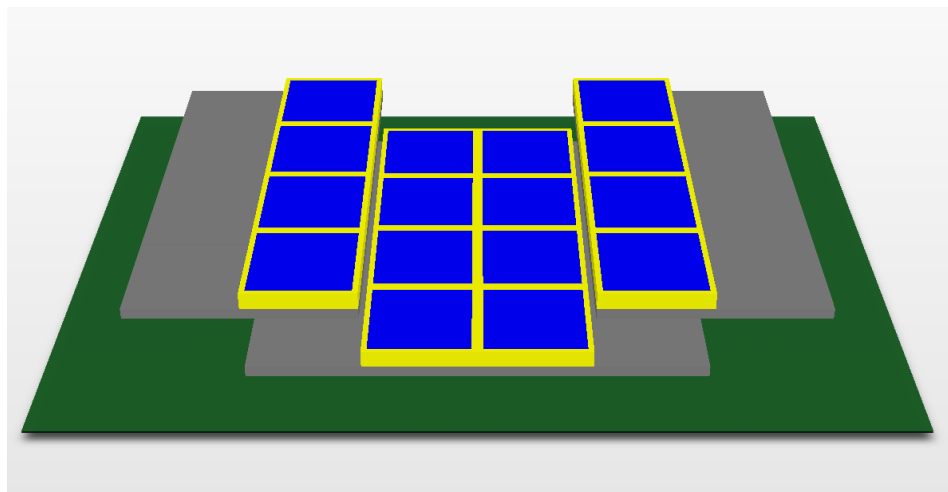


Figure 2.3: Schematic of a proposed design for the hard X-ray mission concept HEX-P. The focal plane module aboard HEX-P will consist of hybrid detectors very similar in design to those of NuSTAR, but the collecting area will be increased. The design shown here consists of 16 hybrids made up of CZT or similar semiconductor (blue with yellow outlines) bonded to an improved readout electronics (grey).

NuSTAR ASIC for the purpose of hard X-ray spectroscopy. Using a Python module I produced for the analysis of NuSTAR hybrid data, I determined the spectral resolution we can hope to achieve with the Redlen material, and I investigated effects arising from variations in the depth at which photons interact with the material. Chapter 6 was adapted from a manuscript which, at the time of writing, has been submitted for peer review in the SPIE Journal of Astronomical Telescopes, Instruments, and Systems.

*Chapter 3***OBSERVING THE TRANSIENT PULSATIONS OF SMC X-1
WITH NUSTAR**

Pike, Sean N. et al. (Apr. 2019). “Observing the Transient Pulsations of SMC X-1 with NuSTAR”. In: *ApJ* 875.2, 144, p. 144. DOI: 10.3847/1538-4357/ab0f2b. arXiv: 1903.06306 [astro-ph.HE].

3.1 SMC X-1: a mildly super-Eddington supergiant X-ray binary

High Mass X-ray binary (HMXB) systems, in which a compact object accretes matter from a more massive companion, often exhibit variability on multiple timescales ranging from less than a second to several months. For most HMXBs, accretion onto the compact object is fed by the stellar winds of the companion. However, in some cases, the objects may orbit at a small enough distance that the companion fills its Roche lobe, resulting in higher accretion rates and higher luminosities. In the case of accreting neutron stars, matter is funnelled along the magnetic field lines onto the surface of the star, resulting in a column of accreted material at the magnetic poles. Because the magnetic poles and the spin axes are not perfectly aligned, the accretion column revolves at the same rate as the neutron star, resulting in emission which appears pulsed.

One such HMXB which has been well-studied is SMC X-1. This system, residing in the Small Magellanic Cloud, was first detected by R. E. Price et al. (1971). It was later resolved as a discrete source by Leong et al. (1971), who reported significant variability in both the intensity and spectrum of the source. The binary nature of SMC X-1 was soon confirmed by Schreier et al. (1972) who discovered periodic occultations with an orbital period of around 3.9 days. SMC X-1 also exhibits pulsations with a period of about 0.7 seconds, and the pulse fraction and shape are known to vary significantly over time (Lucke et al., 1976). The existence of X-ray pulsations confirms that the accreting compact object is a neutron star. Accretion onto the neutron star has been attributed to Roche lobe overflow (Hutchings et al., 1977; Paradijs and Zuiderwijk, 1977) of its companion, Sk 160, which has been spectrographically classified as a B0 I supergiant (Webster et al., 1972). This classification places SMC X-1 in a subcategory of HMXBs known as supergiant X-ray binaries (SGXB). Finally, the source exhibits super-orbital variability on a

timescale of 45 to 60 days, which has been attributed to obscuration by a precessing tilted accretion disk (Wojdowski et al., 1998). Throughout this paper, we assume a distance to SMC X-1 of 60.6 kpc as reported by Hilditch, Howarth, and Harries (2005).

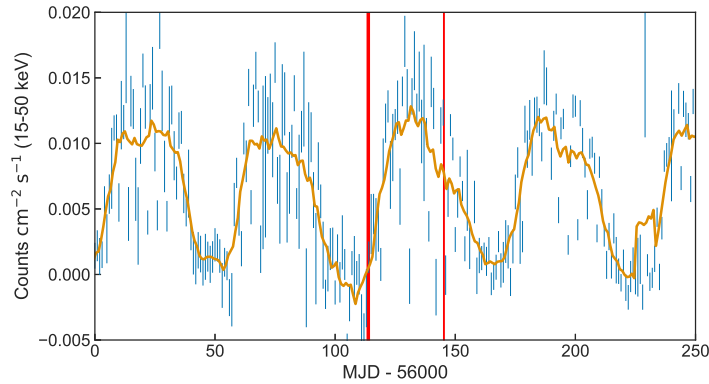


Figure 3.1: *Swift* BAT light curve of SMC X-1 during 2012. The moving average of the BAT flux is shown in gold. A super-orbital period of around 60 days is clearly visible. The red vertical bars indicate the duration of each NuSTAR observation presented here. The first observation (10002013001) took place near the end of the low state, while the second observation (10002013003) took place as the source was growing fainter shortly after the high state.

One of only a handful of SGXBs known to accrete via Roche lobe overflow, SMC X-1 exhibits persistent emission near or above its isotropic Eddington luminosity of $L_{Edd} \sim 1.3 \times 10^{38} \text{ erg s}^{-1}$ (for a mass of $\sim 1.1 M_{\odot}$, as reported by Meer et al. 2007) varying between $L_X(2 - 12 \text{ keV}) \sim 10^{37} \text{ erg s}^{-1}$ in the low state and luminosities in excess of $5 \times 10^{38} \text{ erg s}^{-1}(2 - 12 \text{ keV})$, more than three times its Eddington luminosity, in the high state (Bonnet-Bidaud and Klis, 1981). In addition to this persistent emission, SMC X-1 has been shown to exhibit type II X-ray bursts with durations of tens of seconds (Angelini, Stella, and White, 1991; Rai, Pradhan, and B. C. Paul, 2018). Its near- to super-Eddington luminosity places the source in a middle ground between less luminous Be/X-ray binaries (BeXB), which exhibit a range of persistent X-ray luminosities from $10^{32} \text{ erg s}^{-1}$ (John A. Tomsick et al., 2011) up to $10^{35} \text{ erg s}^{-1}$ (Reig and Roche, 1999), and brighter ultraluminous X-ray pulsars (ULXPs).

ULXPs, the known examples of which are M82 X-2 (M. Bachetti et al., 2014),

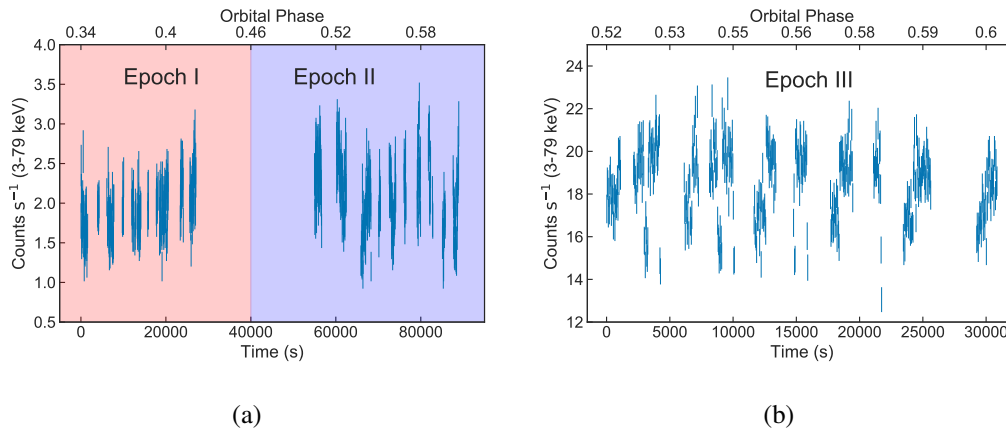


Figure 3.2: (a) NuSTAR FPMA count rate of the source during the first observation (10002013001). The gap between 30000 and 50000 seconds is due to a failed data downlink and is not inherent to the source. We have split this observation into two epochs. (b) NuSTAR FPMA count rate of the source during the second observation (10002013003). We define the third epoch as the entirety of this observation. The apparent variability on timescales of ~ 5000 s during Epoch III can be attributed to movement of the source between detectors. Both light curves are binned into intervals of 40 s. The orbital phase, which is defined by full eclipse of the source at $\phi = 0$ and $\phi = 1$, is included along the horizontal axis as well as the time in seconds since the beginning of the each observation.

NGC 7793 P13 (F. Fürst et al., 2016; G. L. Israel et al., 2017), NGC 300 ULX1 (also SN 2010da, Carpano et al. 2018) and NGC 5907 ULX-1 (Gian Luca Israel et al., 2017), vary between bright pulsing states during which the luminosity can reach 10^{41} erg s⁻¹ — several orders of magnitude above the Eddington limit of a typical neutron star — and faint states when the luminosity drops to 10^{37-38} erg s⁻¹ (Kaaret, Feng, and Roberts, 2017). Similar to SMC X-1 (Inam, Baykal, and Beklen, 2010), these sources exhibit pulsations with periods on the order of one second and spin-up rates of $|\dot{P}| = 10^{-11} - 10^{-9}$ s s⁻¹, with the exception of NGC 300 ULX1, which has a much longer pulse period of 32 s and a faster spin-up rate on the order of 10^{-7} s s⁻¹.

A given ULXP may not exhibit detectable pulsations at all times, and when they are detected, the fraction of their flux which is pulsed is variable. Pulse transience has been attributed to the propeller effect in which rotation of the neutron star’s magnetosphere halts accretion by flinging accreting material out of the system before it can reach the corotation radius (Illarionov and R A Sunyaev, 1975). In contrast to the flux variability of SMC X-1 which occurs quasi-periodically with a continuous

transition between high and low states, the propeller effect is associated with changes of more than a factor of 40 in luminosity on shorter timescales which results in a bimodal flux distribution in ULXPs (Sergey S Tsygankov et al., 2016). In terms of pulse fraction, this bimodality corresponds to distinct pulsed and non-pulsed states. However, continuous variability in pulse fraction has also been observed in ULXPs. In particular, the pulse fraction of M82 X-2 was shown to gradually increase from 8% to 23% in the 10 – 30 keV range over an interval of around 10 days (M. Bachetti et al., 2014).

Periodic variability on timescales of 60-80 days has also been measured for the ULXPs NGC 7793 P13, NGC 5907 ULX-1, and M82 X-2 (Motch et al., 2014; D. J. Walton et al., 2016; Brightman et al., 2019, respectively). While the 64 day period observed in NGC 7793 P13 has been attributed to the orbital motion of the binary (Fürst, D J Walton, et al., 2018), this variability has been classified as super-orbital in the case of M82 X-2. It is still uncertain whether the 78 day period observed in NGC 5907 ULX-1 is orbital or super-orbital in nature. Given that SMC X-1 displays super-orbital modulations on similar timescales, as well as its persistent near- to super-Eddington luminosity and variable pulsations, SMC X-1 may provide a link between ULXPs and classes of X-ray binaries which have been studied in more detail.

In this paper, we present timing and spectral analyses of two observations of SMC X-1. In Section 3.2, we describe the observations of SMC X-1 and our data reduction methods, including data extraction and corrections. In Section 3.3, we describe the methods and results of our timing analysis, and in Section 3.4, we describe the spectral analysis of SMC X-1. In Section 3.5, we discuss the results of our analyses and offer a physical interpretation. Finally, in Section 3.6, we list our conclusions and discuss possible applications of our analysis to studies of ULXPs.

3.2 Observations and Data Reduction

SMC X-1 was observed twice by the *Nuclear Spectroscopic Telescope Array* (NuSTAR) (Harrison et al., 2013) in 2012, in the first two months after the launch of the satellite for the purpose of calibration. NuSTAR consists of two focal plane modules, FPMA and FPMB, each of which is made up of four pixelated detectors (DET0-DET3). Each module has a field of view of about 12 arcminutes, and, combined with focusing optics at a focal length of 10 m, achieves an angular resolution of 18 arcseconds, full width at half maximum (FWHM). The energy resolution, given

by the FWHM, is 400 eV at 10 keV and 900 eV at 68 keV, and the full energy range is 3-79 keV. The timing resolution of the onboard clock is $2 \mu\text{s}$ with a dead time of 2.5 ms, leading to a maximum count rate of around $400 \text{ events s}^{-1}$.

The first observation took place on 2012 July 5 (OBSID 10002013001) and the second took place on 2012 August 6 (OBSID 10002013003) with exposure times of 27 ks and 15 ks, respectively. Figure 3.1 shows the light curve of the source as observed by the *Neil Gehrels Swift Observatory* Burst Alert Telescope (BAT) during a 250 day interval bracketing the NuSTAR observations in 2012. The super-orbital period of around 60 days is clearly visible, and the red bars show the location and duration of each observation in the super-orbital cycle. The first NuSTAR observation occurred at the end of the low state, when the luminosity was just beginning to rise, while the second observation occurred near the end of the high state, when the source was growing fainter. The observations were planned such that they avoided obscuration effects due to the donor star.

We reduced the data using version 1.8.0 of the NuSTARDAS pipeline and NuSTAR CALDB v20170817. We used DS9 (Joye and Mandel, 2003a) to select a circular source region with radius 55 arcseconds centered on the position of the source determined by automatic centroid detection. We also selected a circular background region with radius 80 arcseconds located on the same detector as the source, taking care to choose a region free of other sources and outside the source distribution. We corrected the photon arrival times to the solar system barycenter using the position of the source used for data extraction. Before analysis, the photon arrival times were also corrected for the orbital motion of the source using parameters reported by Falanga et al. (2015) and Inam, Baykal, and Beklen (2010).

We define three epochs of observation, labeled Epochs I, II, and III. The NuSTAR light curve for each observation is shown in Figure 3.2. Epoch I is defined as the first 40 ks (13 ks of exposure time) of observation 10002013001, while the latter half (14 ks of exposure) of observation 10002013001 makes up Epoch II. The whole of observation 10002013003 makes up Epoch III, which has an exposure time of 15 ks. During observation 10002013001, the source was positioned on DET0, while the source was positioned on DET3 near the gap between DET3 and DET0 during observation 10002013003. Movement of the source between the two detectors accounts for the $\sim 5000 \text{ s}$ variability apparent in Figure 3.2b. The background count rate did not vary significantly between observations, and for all three epochs, the background rate remained below 10% of the total count rate for energies up to

Table 3.1: Results of the folding pulsation search for each epoch.

Epoch	T_{ref} (MJD)	P (s)	$ \dot{P} $ (10^{-8} s s $^{-1}$)	Pulse Fraction (%)
I	56113.28661210	< 4.5
II	56113.92279551	0.70121(20)	< 1.2	21.5 ± 1.5
III	56145.10372569	0.70117(9)	< 0.77	40.9 ± 0.5

~ 50 keV. To avoid background contamination, we performed spectral analysis for energies between 3 keV and 40 keV, resulting in 5.2×10^4 , 6.3×10^4 , and 6.3×10^5 spectral counts (combined FPMA and FPMB) for Epochs I, II, and III, respectively. For the purpose of spectral analysis, we binned the data such that there are at least 50 counts in each energy bin in Epoch I and Epoch II, and at least 100 counts in each energy bin in Epoch III. We chose to bin Epoch III with more events per bin due to the significantly higher count rate during that epoch.

3.3 Timing Analysis

We performed a timing analysis of both observations using the Stingray (Huppenkothen et al., 2016) and HENDRICS (Matteo Bachetti, 2015) software packages in order to determine the pulse fraction, pulse period, and spin-up rate during each epoch. The results of this analysis are shown in Table 3.1. The pulse fraction, PF , is defined as follows

$$PF = \frac{F_{max} - F_{min}}{F_{max} + F_{min}} \quad (3.1)$$

where F_{max} and F_{min} are the maximum and minimum fluxes in the pulse profile, respectively. All pulse fractions and corresponding errors quoted were calculated using a Monte Carlo analysis. Given a measured pulse period and derivative, we folded the observed events into a pulse profile with sixteen phase bins per cycle. The uncertainty in flux for each phase bin is given by a Poisson distribution. We sampled this distribution for each phase bin to produce a large number of simulated pulse profiles and passed these profiles through a Savitzky-Golay filter (Savitzky and Golay, 1964). We thus arrived at a distribution of smoothed profiles from which we extracted the mean pulse fraction and corresponding confidence regions. All uncertainties and upper limits quoted in this section and following sections correspond to 90% confidence ranges unless otherwise indicated.

Before searching for and analyzing pulsations, we first determined the orbital phase

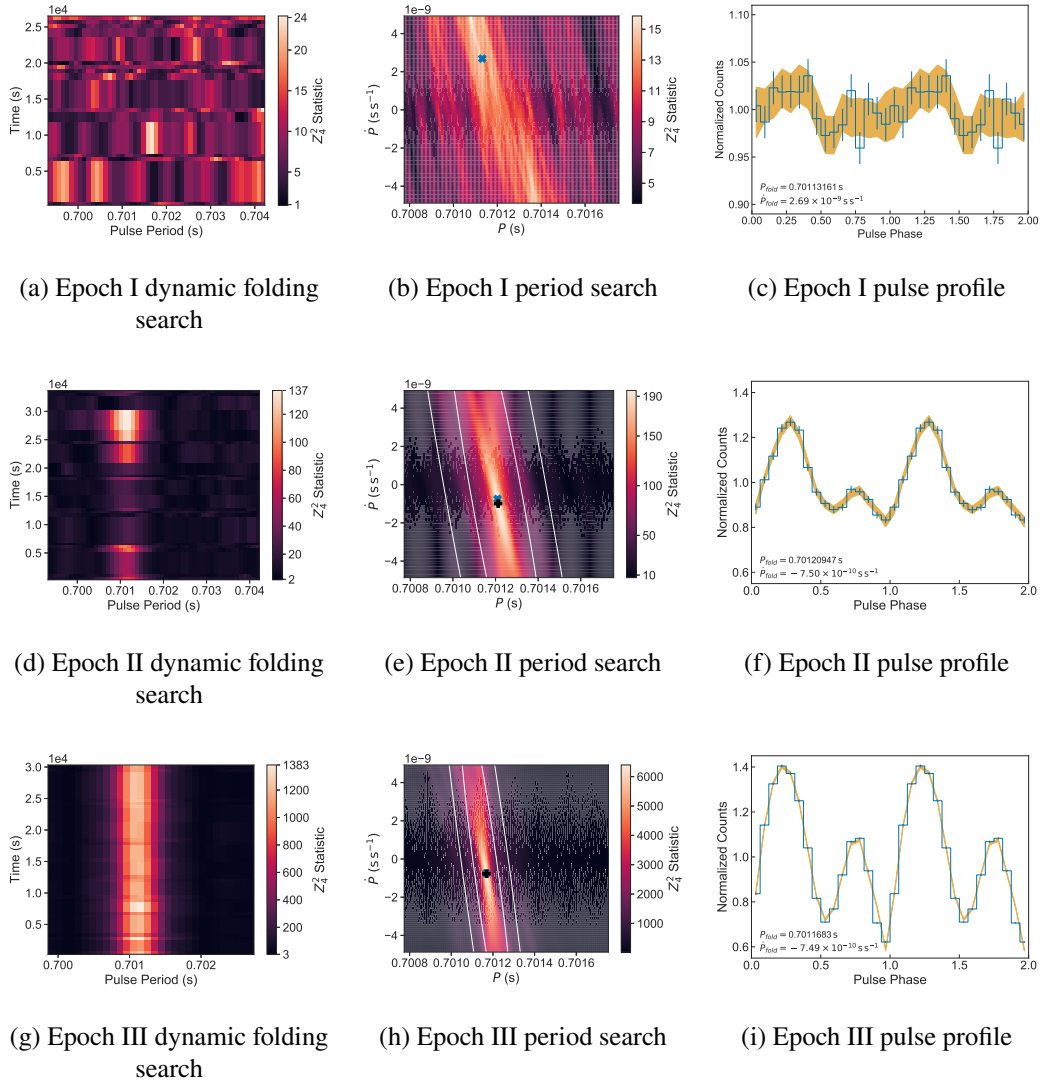


Figure 3.3: Results of pulsation searches applied to each epoch. The left column shows the results of a dynamic folding search. Pulsations are not detected during Epoch I but seem to appear and gradually increase in strength after observation continues during Epoch II. Pulsations are clearly detected in Epoch III and do not appear to vary significantly throughout the epoch. The middle column shows the results of folding searches over both the pulse period and its first derivative. The results of the dynamic searches allowed us to search over a narrower period range. The resulting Z_4^2 distribution (b, e, and h) for each epoch is fitted to a 2-d Gaussian distribution. The mean of the fitted Gaussian is indicated by a black cross while the white contours represent the 1- and 2-sigma confidence regions. The apparent correlation between P and \dot{P} is an artifact of the search itself and is not intrinsic to the source. The maximum Z_4^2 value achieved by each search is indicated by a blue cross and was used to produce pulse profiles shown in blue in panels b, d, and f. In gold are the 90% confidence regions determined by the Monte Carlo procedure described in Section 3.1. When applied to Epoch I, the search produces multiple maxima of relatively low detection probability, resulting in a poor fit which cannot constrain the pulse period and first derivative to within the search bounds. We therefore do not show the fitted Gaussian, and we choose to fold the pulse profile using the maximum nearest the values measured for Epochs II and III. The result is a profile with weak pulsations which are not detected when the last 5000 s of Epoch I are omitted. During Epochs II and III, however, the pulse period is well-constrained, resulting in distinctive pulse profiles, shown in the right column. Note that the scale of the y-axis in panel (c) is narrower than those of (f) and (i) in order to better illustrate the pulse profile during Epoch I.

of the observations. Using the orbital parameters reported by Falanga et al., 2015, we determined the mid-eclipse times which occurred immediately before and after the observations according to the quadratic orbital change function

$$T_n = T_0 + nP_{orb} + \frac{1}{2}n^2P_{orb}\dot{P}_{orb} \quad (3.2)$$

where T_0 is the reference epoch (MJD 52846.6888), n is the number of elapsed orbits, P_{orb} is the orbital period measured at T_0 (3.8919232 days), and \dot{P}_{orb} is the time derivative of the orbital period measured at T_0 (-3.77×10^{-8} day day $^{-1}$). Defining the mid-eclipse times preceding and following each observation as orbital phases 0 and 1, respectively, we found that the first observation occurred between orbital phases 0.34 and 0.61, while the second observation occurred between phases 0.52 and 0.61. These orbital phases are determined to better than 10^{-5} and lie far from the eclipse ingress and egress times. Therefore we can be confident that there were no obscuration effects due to the supergiant companion.

We performed pulsation searches on the combined filtered and calibrated FPMA and FPMB events for each of the three epochs. When combining the FPMA and FPMB events for each epoch, we produced common good-time intervals (GTIs) in order to avoid introducing artificial variability due to non-simultaneous observation and differences in sensitivity between the two focal plane modules. We began our pulsation search by performing a dynamic search using the HENDRICS function `dyn_folding_search`. This function steps over time and pulse period, folds the events into a pulse profile with that period, and calculates the Z_4^2 statistic (Buccheri et al., 1983), a measure of the probability of pulsation detection, of the profile produced at each step. The probability density function of the Z_4^2 statistic is equivalent to that of a χ^2 distribution with 8 degrees of freedom. Therefore, one can use the χ^2 cumulative distribution function to determine the probability that a pulse profile with a given value of Z_4^2 has been produced by noise. For example, a profile with $Z_4^2 = 13$ has a 10% probability of being produced by noise, therefore this can be considered a detection at 90% confidence. A 5-sigma detection, corresponding to a probability of 5.7×10^{-7} that a signal has been produced by noise, would yield a Z_4^2 statistic of 44.

The results of the dynamic pulsation search applied to Epoch III (Figure 3.3g) confirm the presence of strong pulsations. The pulsations appear to remain persistent throughout the observation with a period around 0.701 s and without a large period derivative. The results of this test are less striking upon application to Epochs I and

II (Figures 3.3a and 3.3d). The Z_4^2 statistic reaches only a fraction of the maximum value measured during Epoch III, and during Epoch I, there is no sign of pulsations. However, during Epoch II, pulsations appear to have begun with a period similar to that observed in Epoch III, reaching a maximum detection probability at the end of the observation.

We next simultaneously searched for the period and first period derivative of the pulsations for each of the three epochs using the HENDRICS function `folding_search`. The results of this search are shown in the second column of Figure 3.3. We were able to measure the pulse period and to put upper limits on the first derivative during Epochs II and III by fitting the resulting Z_4^2 distributions to 2-dimensional Gaussian distributions¹ with mean pulse periods at $P_{\text{II}} = 0.70121(20)$ s and $P_{\text{III}} = 0.70117(9)$ s, respectively. We have obtained upper limits on the instantaneous spin-up rates of $|\dot{P}_{\text{II}}| < 1.2 \times 10^{-8}$ s s⁻¹ and $|\dot{P}_{\text{III}}| < 7.7 \times 10^{-9}$ s s⁻¹. Note that there is a correlation between P and \dot{P} apparent in Figure 3.3. This is not intrinsic to the source itself but is an artifact introduced by the search procedure. In addition to measuring the pulse periods and constraining the instantaneous spin-up rates, we have also placed an upper limit on the secular spin-up rate between Epoch II and Epoch III of $|\dot{P}_{\text{sec}}| < 10^{-10}$ s s⁻¹. After determining the pulse periods and the spin-up rates, we then folded the events into pulse profiles at the Z_4^2 maxima produced by the pulsation searches. These pulse profiles are shown in Figures 3.3f and 3.3i. We observe distinct pulsations in the pulse profiles of Epochs II and III. The probability that these profiles were produced by noise is vanishingly small, being less than 10^{-37} in both cases.

In stark contrast, we were completely unable to constrain the pulse period during Epoch I. There are multiple local maxima of comparable amplitude in the Z_4^2 distribution. We therefore chose to fold the events into a pulse profile (see Figure 3.3c) using the maximum nearest the values measured during Epochs II and III. This corresponds to a pulse period of $P_{\text{fold}} = 0.70113161$ s and a first derivative of $\dot{P}_{\text{fold}} = 2.69 \times 10^{-9}$ s s⁻¹. The resulting profile has a pulse fraction of $< 4.5\%$. This is relatively small compared to the pulse fractions of $21.5\% \pm 1.5\%$ during Epoch II and $40.9\% \pm 0.5\%$ during Epoch III. In addition to the small pulse fraction during Epoch I, the Z_4^2 value of the calculated pulse profile is less than 15 and corresponds to a probability of 7% that the detection is due to noise. Furthermore, when the last 5000 s of Epoch I are omitted from the pulsation search even this weak detection

¹The uncertainties reported for the pulse periods and the upper limits of the spin-up rates were determined using the widths of the fitted Gaussian distributions.

disappears, indicating that pulsations were absent until the very end of Epoch I. Therefore, we refer to Epoch I as the non-pulsing state.

The pulse periods that we have measured during Epochs II and III and the resulting pulse profiles are in line with previous measurements (cf. Moon, Eikenberry, and Wasserman, 2003; Naik and Paul, 2004; Raichur and Biswajit Paul, 2010; Inam, Baykal, and Beklen, 2010). In particular, we have extrapolated previous results by applying an orthogonal distance regression to the pulse frequencies reported by Inam, Baykal, and Beklen. We arrived at a spin up of $\dot{f}_{pulse} = 2.589(8) \times 10^{-11} \text{ Hz s}^{-1}$ during the interval 50093-52988 MJD. When propagated forward to the beginning of Epoch III, a pulse period of 0.70093(2) s is predicted. The discrepancy of $2.39(96) \times 10^{-4} \text{ s}$ is small but nonzero. This is consistent with a piece-wise spin-up evolution, reported by Inam, Baykal, and Beklen, in which the spin-up rate is variable. We also note that, although the pulse fraction increases with energy, the shapes of the pulse profiles during Epochs II and III do not appear to vary significantly with energy.

3.4 Spectral Analysis

We also performed a spectral analysis of each of the three epochs using Xspec (v.12.10.0 Arnaud, 1996). We simultaneously fit the spectra measured by FPMA and FPMB while including a relative constant to account for small ($< 10\%$) differences in flux between the two focal plane modules. In addition, for all spectral models described in this section, we have included an absorber in the form of the `tbabs` component. This component compensates for absorption due to Galactic material. We fixed the equivalent HI column density of this component at $N_{\text{H}} = 4.58 \times 10^{21} \text{ cm}^{-2}$, determined from the full-sky HI survey, HI4PI (Ben Bekhti et al., 2016). The spectral fits were performed using interstellar medium abundances reported by Wilms, Allen, and McCray, 2000.

The spectra for each epoch are shown in Figure 3.4, and the results of our spectral analysis are presented in Table 3.2. Each panel in Figure 3.4 also includes residuals for three different models, including a simple absorbed power law meant to illustrate additional structure in the spectra. We have found two models that provide fits of similar quality and which result in physically reasonable parameters. Motivated by previous work by, e.g., Woo, Clark, Blondin, et al. (1995), Angelini, Stella, and White (1991), and Pottschmidt et al. (2014), the first model we investigated was an absorbed power law with a phenomenological cutoff, named `fdcut` (Tanaka, 1986)

Table 3.2: Values of spectral parameters determined by χ^2 fitting of observed spectra. Two models are shown: a fully covered power law with a Fermi-Dirac-like cutoff modeled by `fdcut` (top), and a partially covered power law with an exponential cutoff, modeled by `cutoffpl` (bottom).

Component	Parameter	Epoch I	Epoch II	Epoch III
tbabs	N_{H} (10^{22} cm $^{-2}$)	16 ± 5	24^{+5}_{-4}	$1.9^{+1.3}_{-0.9}$
	Γ	1.0^{\dagger}	1.0^{\dagger}	1.0^{\dagger}
fdcut	E_{cut} (keV)	$17.3^{+1.6}_{-2.3}$	$11.0^{+3.2}_{-5.1}$	$9.1^{+2.5}_{-3.0}$
	E_{fold} (keV)	$6.7^{+0.8}_{-0.6}$	$8.7^{+1.0}_{-0.8}$	9.6 ± 0.4
	Norm (10^{-3})	$8.0^{+1.4}_{-0.9}$	$13.8^{+3.2}_{-2.5}$	107^{+29}_{-16}
gauss	$E_{6.4}$ (keV)	6.36 ± 0.04	6.36 ± 0.06	$6.51^{+0.09}_{-0.07}$
	$\sigma_{6.4}$ (keV)	0.24 ± 0.06	0.21 ± 0.10	0^{\dagger}
	Norm (10^{-4})	3.3 ± 0.5	$2.3^{+0.6}_{-0.5}$	1.9 ± 0.7
gauss	$E_{13.5}$ (keV)	13.5^{\dagger}	13.5^{\dagger}	...
	$\sigma_{13.5}$ (keV)	$2.2^{+0.8}_{-0.7}$	$1.7^{+1.8}_{-0.9}$...
	Norm (10^{-4})	$2.3^{+1.6}_{-1.1}$	$1.1^{+1.7}_{-0.7}$...
bbody	kT (keV)	$0.36^{+0.04}_{-0.06}$	$0.31^{+0.03}_{-0.04}$	0.26 ± 0.09
	Norm (10^{-3})	$3.6^{+3.5}_{-1.9}$	$19.6^{+24.6}_{-9.3}$	56^{+195}_{-45}
bbody	kT (keV)	1.46 ± 0.07
	Norm (10^{-3})	2.3 ± 0.4
	Absorbed Flux ^a (10^{-11} erg cm $^{-2}$ s $^{-1}$)	$6.26^{+0.15}_{-0.32}$	$6.67^{+0.06}_{-0.49}$	$99.3^{+0.8}_{-15.4}$
	Unabsorbed Flux ^a (10^{-10} erg cm $^{-2}$ s $^{-1}$)	$1.46^{+0.56}_{-0.33}$	$2.82^{+1.16}_{-0.69}$	$11.6^{+4.0}_{-0.9}$
	Unabsorbed Luminosity (10^{37} erg s $^{-1}$)	$6.43^{+2.48}_{-1.44}$	$12.4^{+5.1}_{-3.0}$	$51.0^{+17.7}_{-4.1}$
	$\chi^2/\text{d.o.f.}$	693/630 (1.10)	681/679 (1.00)	1091/1019 (1.07)
tbpcf	N_{H} (10^{23} cm $^{-2}$)	$7.8^{+1.9}_{-2.1}$	$5.6^{+0.9}_{-1.2}$	26^{+18}_{-10}
	f_{covering} (%)	51^{+7}_{-8}	61^{+2}_{-4}	15^{+7}_{-6}
cutoffpl	Γ	0.5^{\dagger}	0.5^{\dagger}	0.5^{\dagger}
	E_{cut} (keV)	8.4 ± 0.6	$8.9^{+0.4}_{-0.3}$	9.1 ± 0.2
	Norm (10^{-3})	$6.7^{+1.5}_{-1.2}$	$7.5^{+0.7}_{-0.9}$	53 ± 4
gauss	$E_{6.4}$ (keV)	$6.35^{+0.04}_{-0.05}$	$6.34^{+0.06}_{-0.07}$	6.52 ± 0.08
	$\sigma_{6.4}$ (keV)	0.22 ± 0.07	$0.24^{+0.10}_{-0.09}$	0^{\dagger}
	Norm (10^{-4})	$3.6^{+0.7}_{-0.6}$	$2.6^{+0.7}_{-0.5}$	$2.0^{+0.8}_{-0.9}$
gauss	$E_{13.5}$ (keV)	13.5^{\dagger}	13.5^{\dagger}	...
	$\sigma_{13.5}$ (keV)	$4.9^{+1.3}_{-1.1}$	$1.7^{+3.3}_{-1.1}$...
	Norm (10^{-4})	7.8 ± 3.1	$1.0^{+3.0}_{-0.7}$...
bbody	kT (keV)	$0.23^{+0.08}_{-0.07}$
	Norm (10^{-1})	$1.1^{+72.3}_{-1.0}$
bbody	kT (keV)	$1.46^{+0.08}_{-0.09}$
	Norm (10^{-3})	$3.0^{+0.8}_{-0.7}$
	Absorbed Flux ^a (10^{-11} erg cm $^{-2}$ s $^{-1}$)	$6.49^{+0.06}_{-0.24}$	$6.90^{+0.08}_{-0.09}$	105^{+2}_{-18}
	Unabsorbed Flux ^a (10^{-10} erg cm $^{-2}$ s $^{-1}$)	$1.06^{+0.17}_{-0.14}$	$1.18^{+0.08}_{-0.11}$	$12.7^{+1.1}_{-0.6}$
	Unabsorbed Luminosity (10^{37} erg s $^{-1}$)	$4.65^{+0.73}_{-0.62}$	$5.20^{+0.34}_{-0.47}$	$55.8^{+4.8}_{-2.8}$
	$\chi^2/\text{d.o.f.}$	705/632 (1.11)	681/681 (1.00)	1090/1019 (1.07)

^a Fluxes are reported for FPMA in the energy range 2 – 10 keV.

[†] Values marked with a dagger were frozen during fitting and therefore have no error estimates.

for its resemblance to the Fermi-Dirac distribution, which has both a cutoff energy and folding energy and can be written

$$f_{\text{FD}}(E) = \frac{E^{-\Gamma}}{1 + e^{(E-E_{\text{cut}})/E_{\text{fold}}}} \quad (3.3)$$

where Γ is the photon index, E_{cut} is the cutoff energy, and E_{fold} is the folding energy. The absorber in this model is fully covering and is modeled by `tbabs` (Wilms, Allen, and McCray, 2000). The second model consists of a power law with an exponential cutoff, represented by the Xspec model `cutoffpl`, partially covered by an absorber modeled by `tbpcf`. In addition to these base models, we found that the fits benefited from the addition of secondary components, differing depending on the epoch. Below, we describe each of these models in more detail.

In order to compare the usefulness of additional model components, we use the Bayesian Information Criterion (BIC; Schwarz, 1978). In the case of χ^2 fitting in Xspec, the BIC is given by

$$\text{BIC} = k \ln(n) + \chi^2 \quad (3.4)$$

where n is the number of PHA bins being fitted and k is the number of parameters estimated by a given model. For a given data set, model selection can be achieved by minimizing the BIC, which penalizes models with many parameters. For our analysis, n lies between 600 and 1100 bins, meaning that removing one parameter from a model without a change in χ^2 results in a decrease in the BIC of $\Delta\text{BIC} \approx -7$. In determining the impact of adding or subtracting components, this may be considered one “unit” of model improvement.

The spectra observed during the two observations are qualitatively different, as is visible in Figure 3.4. For Epochs I and II, an absorbed `fdcut` model alone results in significant excess residuals below 4 keV, around 6.4 keV, and above 10 keV. The excess around 6.4 keV is consistent with previous detections of an Fe $K\alpha$ line in SMC X-1, such as those by Woo, Clark, and Levine (1995) and Naik and Paul (2004). We included a Gaussian component at this energy to model the line, allowing both the position and width of the line to vary. To address the low-energy excess, we added a black body component with temperature $kT_{\text{BB}} < 0.5$ keV. Such a component has previously been detected in observations of SMC X-1 by the *Chandra X-ray Observatory* and *XMM-Newton* (Neilsen, Hickox, and Vrtillek, 2004; Hickox and Vrtillek, 2005). Each of these components decreases the BIC by about 100, and adding both of these components results in a combined improvement to the fit of

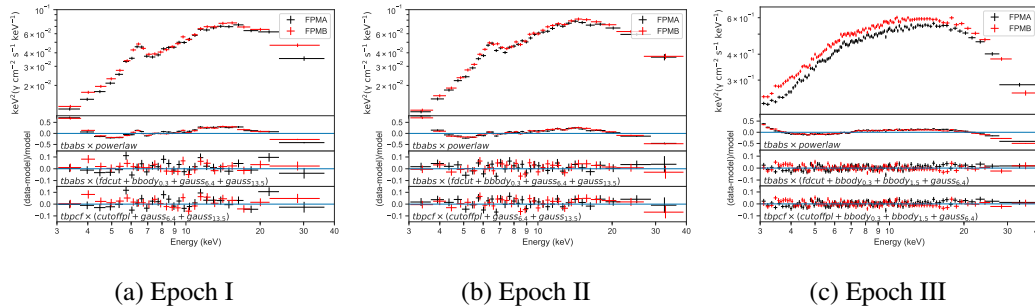


Figure 3.4: Observed spectra for each epoch are shown unfolded against a model with constant (energy-independent) flux in the top panels, and fitting residuals for three different models are shown in the lower panels. The FPMA spectra are shown in black while the FPMB spectra are shown in red. The data is consistently described well by a partially absorbed power law with a high energy cutoff. While the shape of the continuum remains relatively constant, the covering fraction and absorbing column vary between successive epochs, with the covering fraction decreasing significantly between Epoch II and Epoch III.

$\Delta\text{BIC} = -304$ for Epoch I and $\Delta\text{BIC} = -214$ for Epoch II, indicating that the improvement is significant. Adding these components does not resolve the “bump” above 10 keV. This residual resembles the 10 keV feature observed in other accreting pulsars (e.g. Coburn et al., 2002; Mihara, 1995; Santangelo et al., 1998), leading us to include a Gaussian component at $E = 13.5$ keV. We froze the position of this component in order to better constrain other parameters, while the width of the Gaussian was allowed to vary. Adding this component does not result in a significant improvement to the fit, with $\Delta\text{BIC} = -7$ for Epoch I and $\Delta\text{BIC} = +6$ for Epoch II. However, because the residuals are clearly reduced, and this feature is consistent with previous studies of accreting pulsars, the component is included in the final fit.

In the case of Epoch III, the `fddcut` model again requires a low-temperature ($kT_{\text{BB}} < 0.5$ keV) black body in order to explain excess flux below 4 keV, the addition of which improves the fit by $\Delta\text{BIC} = -93$. In addition, although the excess near 6.4 keV is not as prominent as in the previous two Epochs, adding a line at this energy improves the fit significantly ($\Delta\text{BIC} = -46$). However, the width of the line is poorly constrained, leading us to freeze it at $\sigma = 0$. We also found that for Epoch III, adding a $kT \approx 1.5$ keV blackbody component, like the one included by Pottschmidt et al. (2014) in their analysis of this observation, improves the fit by $\Delta\text{BIC} = -46$ while also eliminating an excess of flux above 20 keV. Similar blackbody components with temperatures ranging between 1.2 keV and 3 keV have

proved useful for modeling the spectra of several BeXRBs (e.g. Reig and Roche, 1999; La Palombara et al., 2009; Caballero et al., 2013). In contrast to Epochs I and II, the 13.5 keV bump is not observed during Epoch III, and its addition to the `fdcut` model does not improve the fit nor can this component be easily constrained.

The partially covered cutoff power law provides a similarly good fit to the data as the Fermi-Dirac-like model. However, the secondary components differ somewhat. Adding a line at $E = 6.4$ keV to the base model again improves the fit significantly during Epochs I and II, with $\Delta\text{BIC} = -97$ and $\Delta\text{BIC} = -43$, respectively. Adding this line to Epoch III does not result in a striking improvement (only $\Delta\text{BIC} = -6$), but the position of the Gaussian is constrained to the same value as in the `fdcut` model. The 13.5 keV bump is also added to this model for Epochs I and II, again slightly improving the fits. Unlike the absorbed `fdcut` model, the partially covered cutoff power law does not require a low-temperature black body to resolve excess emission below 4 keV during Epochs I and II. This component, along with the $kT_{\text{BB}} \approx 1.5$ keV black body, remains in Epoch III. Adding each of these black body components individually yields different results. Including only the warm $kT_{\text{BB}} \approx 1.5$ keV black body improves the fit by $\Delta\text{BIC} = -142$, while adding only the low-temperature $kT_{\text{BB}} < 0.5$ keV black body does not improve the fit, yielding $\Delta\text{BIC} = +6$. However, when both components are included, the fit is improved by $\Delta\text{BIC} = -170$. In other words the combination of the low-temperature and high-temperature black body components improves the fit more than each of these components individually.

None of the three spectra can be fit to a simple one-component model, instead requiring several secondary components in order to properly fit the NuSTAR observations. In order to reduce degeneracies resulting from the number of parameters used in the final models, we froze some key parameters at values which are consistent with initial estimates. As mentioned above, the position of the bump above 10 keV was frozen at $E = 13.5$ keV, and the width of the Fe $K\alpha$ -like line in Epoch III was frozen at $\sigma = 0$ keV. In addition to these, we froze the photon indices across all three Epochs at $\Gamma = 1.0$ for the `fdcut` model and $\Gamma = 0.5$ for the `cutoffpl` model.

The final model components, parameter estimates, and fit information are shown in Table 3.2. Here we remind the reader that the uncertainties quoted on spectral parameters represent 90% confidence regions. We found that for both models, the absorption parameters vary between epochs, while the underlying power law models show less variability. In the case of the `fdcut` model, the absorbing column density

decreases by an order of magnitude from $N_{\text{H}} = (2.4_{-0.4}^{+0.5}) \times 10^{23} \text{ cm}^{-2}$ during Epoch II, to $N_{\text{H}} = (1.9_{-0.9}^{+1.3}) \times 10^{22} \text{ cm}^{-2}$ during Epoch III. As we have shown, the pulse fraction simultaneously increases between these two epochs. The shape of the `fdcut` component on the other hand remains consistent between Epochs II and III, with the cutoff energy of $E_{\text{cut}} \approx 10 \text{ keV}$ folding energy of $E_{\text{fold}} \approx 9 \text{ keV}$. However, Epoch I has a slightly higher cutoff energy and lower folding energy: $E_{\text{cut}} = 17.3_{-2.3}^{+1.6} \text{ keV}$ and $E_{\text{fold}} = 6.7_{-0.6}^{+0.8} \text{ keV}$.

On the other hand, in the case of the partially covered cutoff power law, the shape of the `cutoffpl` component stays constant. The exponential cutoff is consistent with $E_{\text{cut}} \approx 9 \text{ keV}$ during all three epochs. The absorption parameters show little variation between Epoch I and Epoch II, but the covering fraction drops by a factor of four from $f_{\text{covering}} = (61_{-4}^{+2})\%$ in Epoch II to $f_{\text{covering}} = (15_{-6}^{+7})\%$ in Epoch III. Between these epochs, the column density appears to increase by a factor of a few, but this parameter is poorly constrained during Epoch III due to the low covering fraction.

In both models, the underlying continuum increases in flux between successive epochs while the flux of the apparent Fe $K\alpha$ line remains constant. Taken together, these observations indicate that the increase in total flux between epochs cannot be attributed solely to the absorption included in the models described above, and that the source of the Fe $K\alpha$ line is likely distinct from the source of the continuum (e.g., originating in the photoionization region surrounding the central X-ray source). In addition, the appearance of the $kT_{\text{BB}} \approx 1.5 \text{ keV}$ black body in Epoch III, observed in both the `fdcut` model and the `cutoffpl` model, may indicate that the emitting region responsible for this component either did not exist or was obscured during Epochs I and II.

3.5 Discussion

Our timing analysis has shown that the source was observed in a non-pulsing state during Epoch I which subsequently evolved into a pulsing state, observed in Epoch II. During Epoch III, about a month after Epoch II, the pulsations had increased in strength, with the pulse fraction increasing by nearly a factor of two. At the same time, our spectral analysis has shown that for all three epochs, the emission of the source can be described by two different models: a fully covered power law with a phenomenological Fermi-Dirac-like cutoff, and a partially absorbed power law with an exponential cutoff. Each of these models requires additional components, but we

found that both models are consistent with variable absorption parameters between the low and high pulse fraction states. In particular, the Fermi-Dirac model exhibits a decrease in absorption column density between Epoch II and Epoch III, and the cutoff power law is consistent with a decrease in the covering fraction (and a poorly constrained increase in column density), between the low and high pulse fraction states. In addition, the luminosity was observed to gradually increase between the non-pulsing Epoch I and the pulsing Epoch II.

In order to synthesize these results, we propose that the pulsing region was observed emerging from behind absorbing material. Given that Epochs I and II took place near the end of the low state, as illustrated in Figure 3.1 and that the super-orbital period has been attributed to a warped precessing accretion disk (Wojdowski et al., 1998; Clarkson et al., 2003; Dage et al., 2018), the absorbing material obscuring the pulsing region is likely part of the accretion disk. In short, the warped accretion disk absorbs and scatters the pulsed emission from the neutron star, leading to the absence of detected pulsations in the low state and a gradual turn-on of pulsations as the disk moves out of the line of sight. This picture is consistent with the opaque inner disk region described by Hickox and Vrtilek (2005) to explain apparent reprocessing of pulsed emission. Their analysis describes the case when both the neutron star and the inner regions of the warped accretion disk are visible to the observer, while ours describes the opposite case when the warped disk lies between the neutron star and the observer, obscuring the pulsing emission regions.

The relatively high absorption column density of the partially covered cutoff power law in Epoch III does not immediately fit within this interpretation. Although this column density is not particularly well constrained, it is still well above the values measured during the first two epochs. This increased column density is accompanied by an increase in the brightness of the power law itself; in other words, the increased flux between the two observations cannot be attributed solely to the absorption included in the models presented here. Thus one interpretation of the combination of a relatively high column density and a relatively low covering fraction is that much of the absorber is completely Compton thick during Epochs I and II. The partially covering absorber represented by `tbpcf`, then, only models the optically thinner regions of the accretion disk leading the covering fraction and column density to be underestimated for the first two epochs. During Epoch III, according to this interpretation, the source is observed through an overall less opaque region of the accretion disk so that a higher column density is measurable.

Pulse fraction variability, including pulse drop-out, has been observed in several other accreting pulsars. In some cases, this variability has been attributed to changes in accretion via the propeller effect (Illarionov and R A Sunyaev, 1975). These include HMXBs Vela X-1 and GX 301–2, which have been shown to exhibit off-states during which the sources drop in luminosity and pulsations are no longer detected (Kreykenbohm et al., 2008; Fürst, Suchy, et al., 2011). LMC X-4, in which pulse drop-out and turn-on have been observed during the high state (Brumback et al., 2018), presents a different case. Still others, such as the low mass X-ray binary Her X-1, exhibit pulse fraction variability attributed to obscuration by warped accretion disks (Kuster et al., 2001). Of these examples, the case of variable obscuration in Her X-1 is most analogous to the behavior we have observed in SMC X-1.

3.6 Conclusions

We have performed spectral and timing analyses of the accreting neutron star binary SMC X-1 for three separate epochs occurring during two NuSTAR observations. Our timing analysis confirmed that the source was observed in the midst of a turn-on of pulsations, which subsequently increased in strength before strong pulsations were observed a month later. Our spectral analysis, which showed variable absorber parameters and luminosity, led us to conclude that the non-pulsing state was due to obscuration of the pulsing region by a warped accretion disk, and that the gradual turn-on was due to the emergence of the pulsing emission from behind the disk.

Similarly to SMC X-1, ULXPs are also known to exhibit variability in their luminosities and pulse fractions. In particular, the gradual change in pulse fraction observed in the beginning of the 2014 observation of M82 X-2 (M. Bachetti et al., 2014) may share the same physical origin as the pulse fraction variability we have observed in SMC X-1. In that case, the super-orbital periods observed in ULXPs may be attributable to precessing accretion disks which periodically obscure the pulsing source, resulting in variability in the observed pulse fractions. Spectral and timing analyses at different points in the super-orbital cycles of known ULXPs, like the analysis we have carried out for SMC X-1, may help to illuminate the accretion mechanism and causes of variability in this recently discovered class of X-ray binary.

Chapter 4

PHOTOSPHERIC RADIUS EXPANSION AND A
DOUBLE-PEAKED TYPE-I X-RAY BURST FROM GRS
1741.9-2853

Pike, Sean N. et al. (Sept. 2021). “Photospheric Radius Expansion and a Double-peaked Type-I X-Ray Burst from GRS 1741.9-2853”. In: *ApJ* 918.1, 9, p. 9. DOI: 10.3847/1538-4357/ac0ef9. arXiv: 2106.13312 [astro-ph.HE].

4.1 Type-I X-ray bursts

Accretion onto compact objects produces an array of phenomena, the study of which can illuminate the nature of these objects and the process of accretion itself. Type-I X-ray bursts represent a particularly dramatic consequence of accretion, wherein the flux of an accreting neutron star (NS) is observed to increase by an order of magnitude or more in the span of only a few seconds or less. In a typical type-I burst, this fast rise in flux is followed by an exponential decay which can take anywhere from tens to thousands of seconds to return to a persistent flux level. Type-I X-ray bursts can provide a wealth of information about the compact stellar remnants from which they originate. The observed fast-rise exponential-decay behavior is thought to be due to runaway thermonuclear burning of accreted hydrogen and helium. This is possible only if the accretor has a surface onto which this material can accumulate in a thin shell which is unable to effectively cool during burning. Therefore, the detection of a type-I X-ray burst confirms the nature of an accreting source as a NS rather than a black hole. Additionally, in some cases type-I bursts allow for the measurement of other important parameters such as the distance to the source or the rotation period of the NS. For a recent review of type-I X-ray bursts, refer to Duncan K. Galloway and Laurens Keek (2021).

During a type-I X-ray burst, the source spectrum can be described by the addition of a blackbody component on top of whichever model best describes the persistent emission. Analyzing how the spectrum changes throughout a type-I burst is necessary in some cases to distinguish between changes in flux which are energy-independent and those which vary across different energy ranges, reflecting changes in the blackbody radius and temperature (Tawara et al., 1984). The latter case is often evidence for photospheric radius expansion (PRE). During PRE the blackbody

which models the burst emission is shown to rapidly increase in radius while decreasing in temperature as the luminosity remains constant at the peak of the burst. This behavior has been attributed to radiation pressure lifting material from the NS surface upon reaching the Eddington limit. Due to the relatively narrow range of acceptable values for NS mass and radius, bursts which demonstrate PRE are often considered “standard candles” which can be used to estimate the distance to a bursting source (J. van Paradijs, 1978; W. H. G. Lewin, Vacca, and Basinska, 1984). Some sources show significant scatter in peak luminosity across many PRE events however (Kuulkers, den Hartog, et al., 2003). As such, these events may serve as approximate standard candles, and source properties such as disk inclination and the composition of burning material must be taken into account when calculating the Eddington luminosity.

Additionally, timing analysis before, during, and after type-I bursts can reveal oscillatory behavior related to burning on the NS surface. Coherent high-frequency oscillations have been observed during some type-I bursts, most often during the decay in brightness (Watts, 2012). These oscillations have been attributed to brightness asymmetries induced by burning on the NS surface, implying that the frequency of burst oscillations corresponds to the rotational frequency of a NS. In some systems, quasi-periodic oscillations (QPOs) at mHz frequencies have also been observed in the persistent emission leading up to type-I bursts. This may indicate that as material accumulates, oscillatory nuclear burning occurs on the surface prior to the onset of the runaway burning which causes type-I bursts.

GRS 1741.9–2853 is a low-mass X-ray binary (LMXB) which was first reported to exhibit type-I X-ray bursts in 1999 (Cocchi et al., 1999). The source resides near the Galactic Center, about 10' from Sgr A* at $\alpha = 17^h 45^m 02^s$, $\delta = -28^\circ 54' 50''$ (M. P. Munro, Baganoff, and Arabadjis, 2003). As it accretes matter from its main sequence companion, it transitions between a low-flux hard spectral state during which angular momentum transfer in the cold disk is inefficient, leading to low mass accretion rates, and a high-flux soft spectral state when the accretion disk enters a hot, efficiently accreting state (Lasota, 2001). GRS 1741.9–2853 is a member of the very faint class of transients, meaning that it reaches a peak 2-10 keV luminosity in the range of $10^{34-36} \text{ erg s}^{-1}$ (R. Wijnands et al., 2005). The first detection of GRS 1741.9–2853 was made by the *GRANAT* satellite and reported in 1990, but was attributed to the nearby source 1E 1741.7-2850 (Mandrour, 1990). Later analysis resolved the source (R. Sunyaev, 1990; Syunyaev et al., 1991). GRS 1741.9–2853

undergoes periods of outburst every ~ 2 years, with typical outbursts ranging in duration from 5 to 15 weeks, resulting in a duty cycle of $\sim 10\%$.

An investigation of the bursting behavior of GRS 1741.9–2853 was presented by Trap et al. (2009). The authors analyzed 15 type-I bursts observed during two periods of outburst in 2005 and 2007 by *INTEGRAL* JEM-X, *Swift* BAT and XRT, and *XMM-Newton*. The bursts had a typical recurrence time between 79 ks and 2 Ms. From this analysis they were able to infer a distance to the source of 7 kpc, and they determined that the bursting behavior was consistent with pure He burning. During another period of outburst in 2013, the source was observed serendipitously during two observations by the Nuclear Spectroscopic Telescope Array (NuSTAR) (Barrière et al., 2015). One type-I X-ray burst lasting 800 s was observed which was consistent with mixed H/He burning. It exhibited mild PRE, allowing the authors to infer a distance to the source which was consistent with the previous estimate of 7 kpc.

Again in April 2020, the source was observed by the XRT instrument aboard the Neil Gehrels *Swift* Observatory to be increasing in brightness, rising from $\sim 10^{-2}$ count/s to $\sim 9 \times 10^{-2}$ count/s over the course of two days, indicating that the source was entering a period of outburst (Degenaar et al., 2020). This detection was followed up by NuSTAR on May 7, 2020.

We report on the detection of two type-I X-ray bursts during the May 2020 NuSTAR observation of GRS 1741.9–2853 in outburst, as well as spectral and timing analyses of the persistent emission. We begin by describing the observation and the methods of data reduction and analysis in Section 4.2. Next, we present an analysis of the NuSTAR light curve, including modeling of each of the two type-I bursts in Section 4.3, the first of which is shown to peak twice. In Section 4.4 we present the persistent and burst spectra and demonstrate evidence for PRE during the second burst. For completeness, in Section 4.5 we present an analysis of the timing features of both the persistent and burst emission, including a search for quasi-periodic oscillations and burst oscillations. We end with a discussion of our results in Section 4.6.

4.2 Observation and Data Reduction

NuSTAR, launched in June 2012, is the first high-energy focusing X-ray telescope (Harrison et al., 2013). It is composed of two focal planes, each paired with a set of focusing optics with a focal length of 10 m. The focal planes, FPMA and FPMB, are each composed of 4 Cadmium Zinc Telluride (CZT) detectors attached to custom

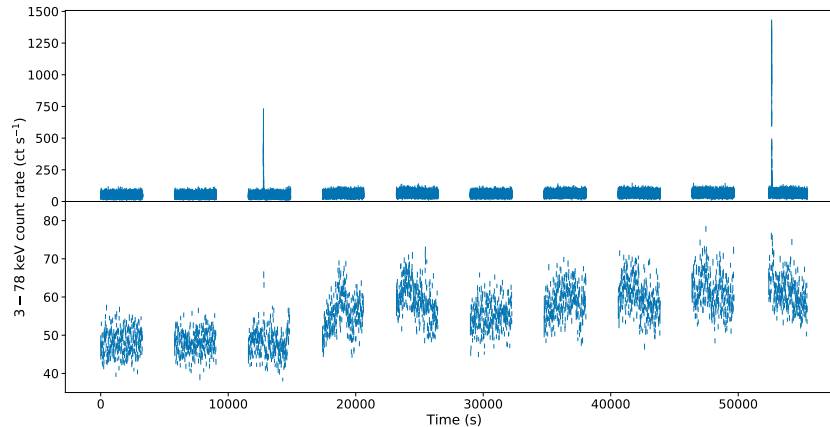


Figure 4.1: The total, background subtracted, livetime corrected NuSTAR light curve is shown twice. The light curve in the top panel shows the entire dynamic range of the light curve and is binned with a resolution of 0.5 s in order to illustrate the bursting behavior. The light curve in the bottom panel is the same as the top, but has been rebinned to a resolution of 10 s and has been restricted along the y-axis in order to illustrate the behavior of the persistent emission.

readout electronics.

GRS 1741.9–2853 was observed by NuSTAR on May 7, 2020, for a total exposure time of 28 ks (OBSID 90601317002). We extracted the data products using NuSTARDAS version 2.0.0 and CALDB version 20200826. Photon arrival times were shifted to the barycenter of the solar system to eliminate residuals due to the orbital motion of NuSTAR. Instrumental effects on the photon arrival times due to changes in the temperature of the on-board clock were corrected using clockfile v110 generated on September 12, 2020. For the production of source spectra as well as cospectra, we used circular extraction regions with radius 100 arcseconds, centered on the source using automatic centroid detection in DS9. To produce background spectra, we used extraction regions of radius 60 arcseconds, residing on the same detector as the source region but sufficiently removed from it so as to exclude source counts. Additionally, we found that in this case, the automated pipeline overcorrected for changes in the Multi Layer Insulation (MLI) (Kristin K. Madsen, Grefenstette, et al., 2020) resulting in inconsistencies between FPMA and FPMB below 5 keV. Therefore, we chose to revert to the previous FPMA ancillary response file.¹

¹For more information on how to determine when this is appropriate, refer to the NuSTAR Science Operations Center homepage.

Timing analyses, such as the production of cospectra and calculation of epoch folding statistics, were performed using the Python package *Stingray* (Daniela Huppenkothen, Matteo Bachetti, Stevens, Migliari, and Balm, 2016). Spectral modeling was performed using the X-ray spectral analysis package *Xspec* (v12.11.1 Arnaud, 1996). Spectra were binned using the variable binning algorithm described by Kaastra and Bleeker (2016) which takes into account both the number of photons in a given energy bin as well as the average energy of the photons in that bin. We note that this binning procedure does not allow one to specify an exact energy range, meaning that the binned spectra may not extend all the way down to 3 keV. We restricted our spectral analysis to an energy range of 3-40 keV for persistent emission, and a range of 3-20 keV for burst emission. At higher photon energies, background counts begin to contribute significantly to the overall spectra. All spectral fitting was performed using the Cash statistic (Cash, 1979), but throughout the paper we present chi-squared fit statistics in order to provide an idea of the quality of various fits using a formalism which is easy to interpret and which gives a clear comparison between models. For the purpose of readability, spectra shown in figures have been further rebinned such that each bin has at least 5-sigma significance. All light curves shown in this paper are the sum of the simultaneous light curves observed by FPMA and FPMB, and have been background subtracted and corrected for variations in the livetimes of the detectors. Errors quoted throughout this paper represent 90% confidence regions unless otherwise stated.

4.3 Light Curve Analysis

The total (3-78 keV) NuSTAR light curve is shown in Figure 4.1, where the top panel shows the light curve binned in 0.5 s increments in order to demonstrate the bursting behavior, and the bottom panel shows the light curve binned in 10 s increments and restricted to count rates below 85 count/s in order to show the persistent flux level. Throughout the observation, GRS 1741.9–2853 showed little variability aside from two dramatic increases in count rate occurring around 12700 s and 52600 s. Additionally, the persistent count rate appeared to increase gradually by about 30% from about 50 count/s to about 65 count/s.

Due to their short duration and dramatic increase in count rate, the features at roughly 12700 s and 52600 s resemble type-I bursts. Indeed upon closer inspection, they exhibit the fast rise followed by an exponential decay which are characteristic of type-I bursts, confirming this classification. Figure 4.2 shows the burst light curves for the entire 3-78 keV NuSTAR band binned into 0.5 s intervals. The bursts not

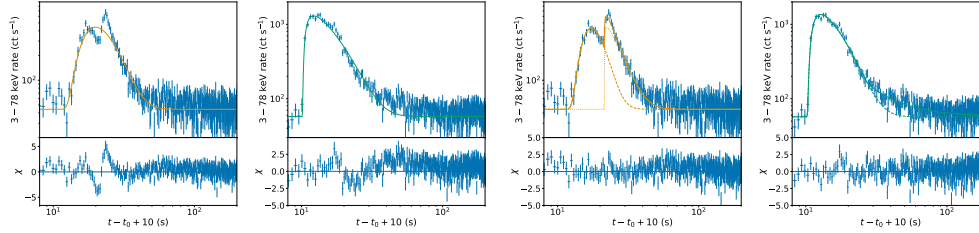


Figure 4.2: Burst light curves along with their best-fit models and residuals. The observed light curves are shown in blue and have been plotted in logarithmic space, where the origin of the x-axis lies 10 s prior to the onset of the corresponding burst, in order to more clearly illustrate the burst structure. The left two panels correspond to Burst 1 and the right two panels to Burst 2. The top panels show the bursts fit to a simple FRED model described by Equation 4.1 and shown by the solid lines. The bottom panels show the bursts fit to more complex models. Burst 1 is fit to a sum of two FRED sub-bursts, the first of which is plotted as a dashed line and second of which is dotted. Burst 2 is modeled by adding a power law component at late times and is described by Equation 4.2. The dashed line shows the FRED component and the solid line shows the total model. Both bursts are described more accurately by their respective augmented models rather than by a simple FRED model.

only differ in maximum count rate, but in their structure as well. The first burst, hereafter Burst 1, appears to have a longer rise time and exhibits two clear peaks in count rate, while the second burst, hereafter Burst 2, exhibits a much faster rise and a single peak.

In order to better understand the structure of the two type-I bursts, we began by fitting the light curves to a simple Fast Rise Exponential Decay (FRED) model, given by

$$f(t) = A \exp \left[-\frac{\tau_R}{t - t_0} - \frac{t - t_0}{\tau_D} \right] + C \quad (4.1)$$

for $t > t_0$, where t_0 is the time at burst onset, τ_R and τ_D are the rise and decay times, respectively, A is a factor which determines the height of the burst, and C is the persistent count rate. From Equation 4.1 it can be seen that the burst peak occurs at $t_{\text{peak}} = \sqrt{\tau_R \tau_D} + t_0$. The height of the burst above the persistent contribution is therefore given by $H \equiv f(t_{\text{peak}}) - C = A \exp \left[-2\sqrt{\frac{\tau_R}{\tau_D}} \right]$. The fits to the simple FRED model, including residuals, are shown in the top panels of Figure 4.2, in which the light curves are plotted in logarithmic space in order to better illustrate the structure of each burst.

Table 4.1: light curve parameters for Bursts 1 and 2. Burst 1 is further broken down into sub-burst 1 and sub-burst 2. The top seven rows were determined via model fitting, while the bottom two rows were calculated based on the fitted parameters. The burst onset times, t_0 , are given relative to the start of the observation, $t_{\text{ref}} = \text{MJD } 58976.305553$.

Model Parameter	sub-burst 1 Value	sub-burst 2 Value	Burst 2 Value	Units
t_0	12752.5 ± 2.3	12763.9 ± 0.2	52614.7 ± 0.1	s
τ_R	$< 52^\dagger$	$< 0.45^\dagger$	1.6 ± 0.3	s
τ_D	2.3 ± 1.3	5.9 ± 0.7	4.9 ± 0.3	s
A	$< 1.4 \times 10^6^\dagger$	556 ± 174	4032 ± 653	count s ⁻¹
$t_{\text{tail}} - t_0$	17.4 ± 1.4	s
γ	1.6 ± 0.2	...
C	44.3 ± 0.3		57.1 ± 0.3	count s ⁻¹
$t_{\text{peak}} - t_0$	7.3 ± 2.4	1.0 ± 0.6	2.8 ± 0.3	s
H	$< 3100^\dagger$	396 ± 69	1298 ± 55	count s ⁻¹

† 90% upper confidence limit.

As expected, Burst 1 shows clear residuals around the peak of the FRED model indicating a double-peaked structure. We therefore proceeded to model Burst 1 as the sum of two ‘‘sub-bursts’’ in quick succession, each modeled as a FRED burst. The fit to this model is shown in the bottom left panel of Figure 4.2. This results in a significantly better fit, eliminating the residuals around the two peaks. Fitting reveals that the first sub-burst has a significantly slower rise time than the second sub-burst but a somewhat faster decay time. It can also be seen in Figure 4.2 that the two sub-bursts have comparable peak count rates. In Section 4.6 we discuss the physical mechanisms by which this double-peaked structure could be realized.

The second burst bears more resemblance to a typical type-I burst. The FRED model describes the shape of the burst well for early times, but excess emission can be seen in the tail of the burst. We therefore adopt a phenomenological model similar to the one used by Barri ere et al. (2015), in which the rise, peak, and beginning of the decay are modeled by a FRED curve, and the late-time emission is modeled as a power law decay rather than an exponential decay. This model can be written as

$$f(t) = \begin{cases} A \exp\left[-\frac{\tau_R}{t-t_0} - \frac{t-t_0}{\tau_D}\right] + C & t \leq t_{\text{tail}} \\ B \left(\frac{t-t_0}{t_{\text{tail}}-t_0}\right)^{-\gamma} + C & t > t_{\text{tail}} \end{cases} \quad (4.2)$$

where t_{tail} is the time at which the emission transitions from an exponential tail to a power law tail, γ is the power law index, and $B \equiv A \exp\left[-\frac{\tau_R}{t_{\text{tail}}-t_0} - \frac{t_{\text{tail}}-t_0}{\tau_D}\right]$ such

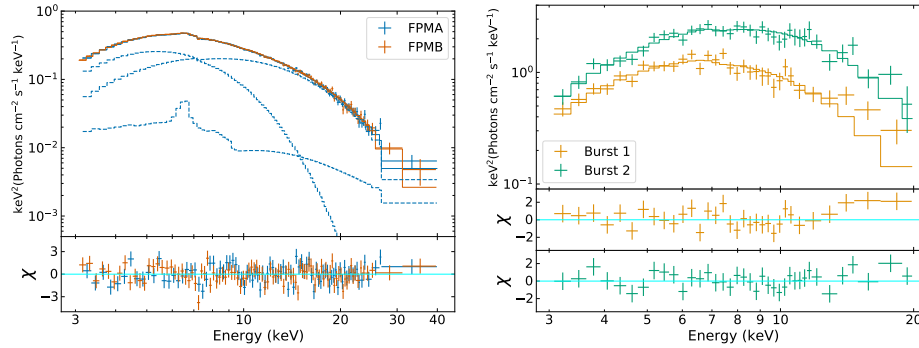


Figure 4.3: Persistent and burst spectra and their best-fit models. The persistent spectra are shown on the left with FPMA in blue and FPMB in red. The solid lines show the best-fit reflection model, and the dashed lines shows the blackbody component, the Comptonized component, and the reflected cutoff power law component. The burst spectra are shown on the right with Burst 1 shown in orange and Burst 2 shown in green. For clarity, only the FPMA spectra are shown. The solid lines show the best-fit models which are dominated by the blackbody component which has been added to the persistent model.

that the exponential tail and the power law tail have the same count rate at $t = t_{\text{tail}}$. This model successfully describes the burst emission both at early and late times, as demonstrated by the bottom right panel of Figure 4.2.

Table 4.1 lists the values of the fitted and calculated parameters for Burst 1 and Burst 2. Both sub-burst 2 and Burst 2 show short rise times and similar decay times. The increase in count rate which is apparent from the the persistent light curve is reflected by the difference in the fitted values of C between Burst 1 and Burst 2. The magnitude of the first sub-burst of Burst 1 is not precisely constrained due to degeneracy with other values and due to the limited number of constraining data points as compared to sub-burst 2, which dominates the light curve beginning about 8 s after the onset of Burst 1. With the onsets of each burst well-constrained, we are able to calculate the recurrence time between Burst 1 and Burst 2, $\Delta t = 39862.2 \pm 2.3$ s. This recurrence time is less than half the shortest recurrence time previously reported for GRS 1741.9–2853 (Trap et al., 2009). Due to the orbital gaps in the light curve, however, it is possible that the two bursts were not consecutive.

4.4 Spectral Analysis

In order to better understand the bursting behavior of GRS 1741.9–2853, it is necessary to characterize both the persistent and burst spectra, as well as to understand

Table 4.2: Spectral parameters determined by fitting the persistent spectra in Xspec. Model 1 corresponds to a Comptonized blackbody without disk reflection, Model 2 corresponds to relativistic disk reflection of an irradiating blackbody, and Model 3 corresponds to relativistic disk reflection of an irradiating cutoff power law.

Component	Parameter	Model 1	Model 2	Model 3
tbabs	N_{H} (10^{22} cm $^{-2}$)	$6.5^{+0.2}_{-0.3}$	$6.6^{+0.5}_{-0.2}$	$7.1^{+0.4}_{-0.3}$
bbodyrad	kT (keV)	1.26 ± 0.01	$1.23^{+0.01}_{-0.02}$	1.24 ± 0.01
	$(R_{\text{km}}/d_{10})^2$	29 ± 2	20 ± 4	26^{+1}_{-2}
nthcomp	Γ	$1.4^{+0.2}_{-0.1}$	$2.0^{+0.2}_{-0.1}$	$1.7^{+0.2}_{-0.1}$
	kT_e (keV)	$2.65^{+0.09}_{-0.08}$	$2.87^{+0.20}_{-0.06}$	$2.66^{+0.09}_{-0.06}$
	Norm (10^{-3})	$4.2^{+1.7}_{-1.2}$	10^{+3}_{-2}	$7.2^{+1.6}_{-0.9}$
gaussian	E (keV)	6.48 ± 0.07
	σ (keV)	$0.24^{+0.10}_{-0.06}$
	K (10^{-4} photon cm $^{-2}$ s $^{-1}$)	4.5 ± 1.0
	Equivalent Width (eV)	39^{+7}_{-4}
relxill/relxillNS	q	...	3.5^{\dagger}	3.0^{\dagger}
	Inclination ($^{\circ}$)	...	13^{+16}_{-7}	17^{+13}_{-11}
	R_{in} (R_{g})	...	61^{+74}_{-15}	44^{+78}_{-18}
	$\log \xi$ (erg cm s $^{-1}$)	...	$2.59^{+0.06}_{-0.23}$	$2.98^{+0.05}_{-0.40}$
	A_{Fe} (Solar)	...	3.0 ± 1.9	$2.1^{+2.1}_{-1.0}$
	Norm (10^{-4})	...	$1.1^{+1.6}_{-0.8}$	$3.1^{+0.9}_{-0.8}$
$\chi^2/\text{d.o.f.}$		293.5/246	284.5/244	274.9/244

† The values of the disk emissivity index were fixed during fitting.

how the spectrum changes during each burst. We began by producing good time intervals (GTI) for the persistent emission as well as for each of the two type-I bursts. For the first burst, we defined the GTI to begin at the onset of the first sub-burst and to end after 5 decay times (τ_D) had elapsed following the onset of the second sub-burst. This results in an interval with length 41 s. For the second burst, we similarly defined the GTI to begin at the onset of the burst and to end after 5 decay times (τ_D) had elapsed, resulting in an interval with length 24 s. The GTI for persistent emission was defined such that it excluded the bursts, with a 100 s buffer prior to the onset of each burst, and a 500 s buffer following the end of each burst's GTI, such that in total 1265 s of the observation was excluded. Using these good time intervals, we were able to extract the persistent and burst spectra. When extracting burst spectra, we loosened the event filters by specifying the status expression “STATUS=b0000xx000xxxx000” when running nupipeline. We therefore were able to avoid removing source photons which would otherwise be mistaken for spurious

Table 4.3: Physical quantities calculated for the persistent emission, based on the non-reflection spectral model.

Quantity	Value	Units
$F_{\text{bol}}^{\text{a}}$	1.20 ± 0.01	$10^{-9} \text{ erg cm}^{-2} \text{ s}^{-1}$
$L_{\text{bol}}^{\text{b}}$	$7.03^{+0.04}_{-0.05}$	$10^{36} \text{ erg s}^{-1}$
\dot{m}^{c}	3.9	$10^3 \text{ g cm}^{-2} \text{ s}^{-1}$
$\dot{m}/\dot{m}_{\text{Edd}}^{\text{d}}$	4.5	%
\dot{M}^{e}	7.8	$10^{-10} M_{\odot} \text{ yr}^{-1}$

^a Bolometric (0.1-100 keV) unabsorbed flux.

^b Bolometric unabsorbed luminosity assuming a distance of 7 kpc.

^c Mass accretion rate per unit surface area as determined by Equation 4.3.

^d Ratio of the mass accretion rate to the Eddington limited rate, $\dot{m}_{\text{Edd}} = 8.8 \times 10^4 \text{ g cm}^{-2} \text{ s}^{-1}$, assuming $M = 1.4 M_{\odot}$ and $R_{\text{NS}} = 10 \text{ km}$.

^e Mass accretion rate assuming a NS radius of 10 km.

events at such high count rates.

Persistent Emission

The persistent spectrum is described well by the standard physical picture of a NS surface or boundary layer emitting blackbody radiation which is Compton upscattered into a powerlaw-like component by a hot corona. In Xspec, we represented the blackbody emission using `bodyrad` and the upscattered emission using `nthcomp` (Zdziarski, Johnson, and Magdziarz, 1996; Życki, Done, and Smith, 1999). The seed photon temperature for `nthcomp` was tied to the temperature of the blackbody. An absorbing column, represented by `tbabs` was also applied to the sum of the model components, with molecular abundances described by Wilms, Allen, and McCray (2000) and cross-sections described by Verner et al. (1996). Fitting with this model resulted in a reduced Chi-squared statistic of $\chi^2_{\nu} = 1.64$ ($\chi^2 = 408.63$; d.o.f. = 249). We observed a clear Fe $K\alpha$ emission feature in the resulting residu-

als, so we also included a Gaussian component at ≈ 6.5 keV. The addition of this component improved the fit significantly, bringing the reduced Chi-squared down to $\chi^2_\nu = 1.19$ ($\chi^2 = 293.5$; d.o.f. = 246), confirming that the component is necessary to accurately describe the observed spectrum.

Additionally, we found that the Fe line emission could be accounted for by replacing the Gaussian component with a relativistic disk reflection model. We found that the spectrum could be described well by the reflection off an accretion disk of a cutoff power law approximating the `nthcomp` component using the `relxill`² model (T. Dauser et al., 2014; J. García, T. Dauser, Lohfink, et al., 2014), or by the reflection of the blackbody component using a modified version of `relxill`, `relxillNS` (García et al., *subm.*). Although reflection of the blackbody using `relxillNS` can account for the line emission, it cannot account for the hard emission on its own, and the `nthcomp` component is still necessary to accurately model the spectrum up to high photon energies.

For both of our reflection models, the disk emissivity index was assumed to be constant throughout the disk, the disk density was fixed at $n = 10^{15} \text{ cm}^{-3}$, the spin parameter was fixed at $a = 0$, and the reflection fraction was fixed at a value of -1 , such that only the reflected component was modeled by `relxill` and `relxillNS` (in other words, we added the reflected component to the non-reflection model described above, rather than replacing the direct blackbody and Comptonized emission with the `relxill` models). In the case of blackbody reflection, the emissivity index of the disk was fixed to $q = 3.5$, corresponding to irradiation of the disk by the NS surface or boundary layer (Wilkins, 2018), and the temperature of the incident blackbody was tied to that of the `bbbodyrad` component. For the case of power law reflection, we fixed the emissivity index at a value of $q = 3$ corresponding to a disk corona geometry. We tied the `relxill` power law index to that of `nthcomp`, and we related the `relxill` cutoff energy to the `nthcomp` electron temperature as $E_{\text{cut}} = 3kT_e - 2 \text{ keV}$ such that the shape of the incident power law roughly approximated the component described by `nthcomp`.

The best-fit parameters for all three models are listed in Table 4.2, where the non-reflection model is referred to as Model 1, the reflected blackbody (`relxillNS`) is referred to as Model 2, and the reflected cutoff power law (`relxill`) is referred

²We note that although the alternative reflection model `relxillCp` models the incident power law using `nthcomp`, that model assumes that the Comptonized blackbody has a disk geometry with fixed temperature of $kT_e = 0.05 \text{ keV}$. In order to maintain consistency between model components we therefore chose to use `relxill` rather than `relxillCp`

to as Model 3. We find that the three models provide a similarly good fit: the reduced chi-squared statistics for Models 1, 2, and 3 are $\chi^2_\nu = 1.19$ (d.o.f = 246), 1.17 (d.o.f = 244), and 1.13 (d.o.f = 244), respectively. The observed spectra as well as the residuals and components of the Model 3 are shown in the left panel of Figure 4.3. The three models are largely consistent with one another, showing little change between their shared components. Additionally, the spectral parameters are consistent with previous measurements (Barrière et al., 2015) with somewhat lower column density and blackbody temperature.

From the non-reflection model, we find an apparent blackbody radius of $R = 3.8 \pm 0.1$ km assuming a distance to the source of 7 kpc. Given that the gravitational redshift on the surface of the NS, given by $1 + z = (1 - 2GM/(c^2 R_{\text{NS}}))^{-1/2}$, is significant, the radius measured by fitting to a blackbody is larger than the radius in the emitting frame by a factor of $(1+z)^{3/2}$. Assuming $M = 1.4 M_\odot$ and $R_{\text{NS}} = 10$ km, we get $1+z = 1.31$. This yields an actual blackbody radius of 2.5 km, consistent with accretion onto a small band rather than spherical accretion onto the entire surface of the NS. The relativistic reflection models provide similar values for the ionization of the disk, $\xi \sim 10^3$ erg cm s⁻¹, as well as the iron abundance, A_{Fe} , which is loosely constrained at about 3 times the Solar value. The iron abundance, however, depends strongly on the disk density which cannot be varied using `relxill` and which we could not constrain with `relxillNS`. We therefore advise against interpreting the iron abundance as the true physical value. Both `relxill` and `relxillNS` yield a low inclination of $\sim 15^\circ$, and an inner disk radius consistent with $\sim 50 R_g$, corresponding to about 100 km for a NS mass of $M = 1.4 M_\odot$.

Having modeled the persistent emission, we were able to constrain the persistent flux and corresponding mass accretion rate. From Duncan K. Galloway, Michael P. Muno, et al. (2008), the bolometric luminosity, L_{bol} , is related to the accretion rate per unit area, \dot{m} , by $L_{\text{bol}} = 4\pi R_{\text{NS}}^2 \dot{m} (GM/R_{\text{NS}})(1+z)^{-1}$. Solving for \dot{m} , as in Barrière et al. (2015), gives

$$\begin{aligned} \dot{m} = & 3280 \times \left(\frac{F_{\text{bol}}}{10^{-9} \text{ erg cm}^{-2} \text{ s}^{-1}} \right) \left(\frac{M}{1.4 M_\odot} \right)^{-1} \\ & \times \left(\frac{R_{\text{NS}}}{10 \text{ km}} \right)^{-1} \left(\frac{d}{7 \text{ km}} \right)^2 \left(\frac{1+z}{1.31} \right) \text{ g cm}^{-2} \text{ s}^{-1} \end{aligned} \quad (4.3)$$

where F_{bol} is the bolometric flux, M and R_{NS} are the NS mass and radius, respectively, d is the distance to the source, and z is the gravitational redshift at the surface

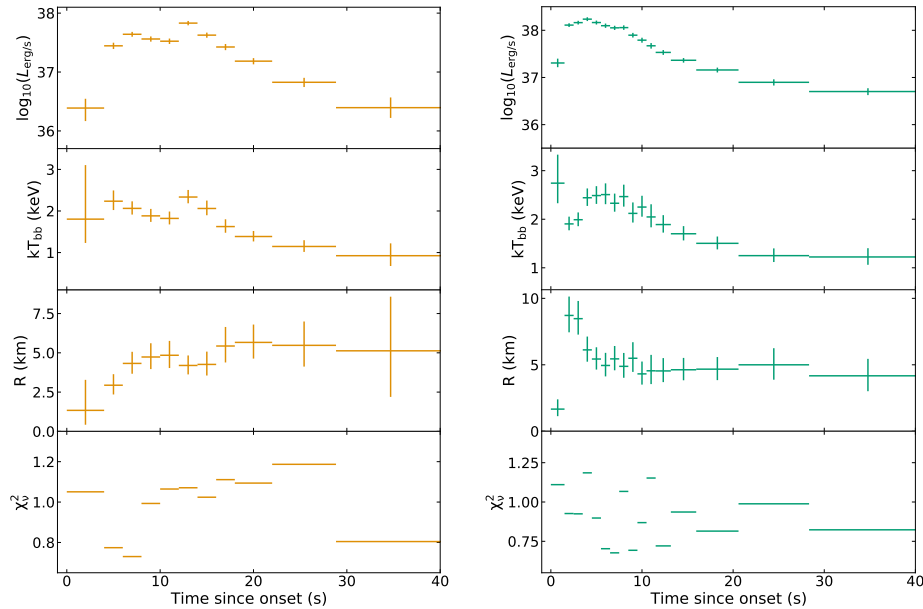


Figure 4.4: Evolution of the blackbody component which describes the emission for each type-I X-ray burst. The apparent unabsorbed bolometric luminosity, temperature, and radius (assuming a distance of 7 kpc) of the blackbody are shown for Burst 1 on the left in orange and for Burst 2 on the right in green. The double-peaked structure of Burst 1 is observed in the intrinsic luminosity, confirming that it is not the result of the spectrum dropping below the NuSTAR bandpass. Burst 2 exhibits a PRE “touchdown” event a few seconds after burst onset in which the blackbody radius contracts rapidly while the temperature increases at constant luminosity.

of the NS. The values which we measured for the bolometric flux and the resulting calculated values of bolometric luminosity and accretion rate, assuming a distance of $d = 7$ kpc, are shown in Table 4.3.

Burst Emission

The burst spectra were modeled by freezing the persistent model (for simplicity, we used the non-reflection model) and adding an additional blackbody component which was allowed to vary in both temperature and normalization.³ Rather than pinning the spectral parameters of the persistent model to the values determined for the full observation, we determined the persistent model parameters relevant to each

³We also tried allowing the total normalization of the persistent model to vary by introducing a multiplicative factor, following the approach of Worpel, Duncan K. Galloway, and D. J. Price (2013) and Worpel, Duncan K. Galloway, and D. J. Price (2015). For Burst 1 we found that this factor was difficult to constrain, and for Burst 2 the factor was consistent with unity and its inclusion resulted in a negligible improvement to the fit statistic. We similarly found that adding a second blackbody component did little to improve the fits and was difficult to constrain.

burst using spectra extracted near the time of that burst, excluding the interval of variability between ~ 15 ks and ~ 35 ks.

For each burst, we produced GTIs of varying length, beginning at the burst onset and ending after several decay times. The GTI lengths were set such that each bin contained a roughly equal number of counts, and so that we could achieve good temporal resolution during the first several seconds of the burst while also maintaining enough photons per time bin to enable robust spectral fitting. For each of these intervals, the spectrum was again extracted and fit to the persistent-plus-blackbody model described above, allowing the blackbody temperature and normalization to vary. The resulting parameters, including the temperature, the unabsorbed bolometric luminosity, and radius of the blackbody (assuming a distance of 7 kpc) are shown in Figure 4.4. Each data point corresponds to a GTI for which spectra were analyzed.

Time-resolved spectroscopy reveals that the double-peaked structure observed in the count rate during Burst 1 is also visible in the luminosity and temperature evolution of the burst. The first sub-burst reached a blackbody temperature of $kT_{\text{bb}} = 2.2$ keV and a luminosity of $L_{\text{bol}} = 4.4 \times 10^{37}$ erg s $^{-1}$, while the second sub-burst reached a blackbody temperature of $kT_{\text{bb}} = 2.3$ keV and a luminosity of $L_{\text{bol}} = 6.8 \times 10^{37}$ erg s $^{-1}$. This analysis confirms that the double-peaked structure is intrinsic to the source. That is, it is not the result of an increase in the fraction of incident photons energies falling below NuSTAR’s lower energy limit of 3 keV due to a softening of the spectrum at a constant luminosity. The available data do not suggest that the NS underwent PRE during either of the sub-bursts which make up Burst 1, but our analysis is limited by our inability to resolve these short sub-bursts into smaller time bins due to insufficient counts.

We showed in Section 4.3 that Burst 2 exhibited a very different structure compared Burst 1. This is borne out in our time-resolved spectroscopic analysis as well. The blackbody luminosity shows a single peak, reaching a bolometric flux of $F_{\text{peak}} = 2.94^{+0.28}_{-0.26} \times 10^{-8}$ erg cm $^{-2}$ s $^{-1}$ ($L_{\text{peak}} = 1.7 \times 10^{38}$ erg s $^{-1}$, assuming a distance of 7 kpc) within a few seconds of the onset of the burst, and a long decay time. On the other hand, the apparent blackbody temperature and radius show variability during the luminosity peak, with the temperature decreasing rapidly from 2.7 keV to 1.9 keV in the first second of the burst, followed by an increase up to 2.5 keV only a few seconds later. This temperature evolution is accompanied by a rapid expansion and contraction of the apparent blackbody radius, which reaches a maximum of 8.7 km

before contracting to about 5 km. We note that the observed values of the blackbody radius and temperature are under- and overestimates, respectively, of their actual physical values. Scattering of the blackbody emission in the NS atmosphere results in a harder emergent spectrum. The overall effect of this scattering is to introduce a color correction factor, f_c , to the effective temperature so that $T_{\text{eff}} \propto T_{\text{obs}} f_c^{-1}$, where T_{obs} is the temperature determined via modeling of the observed spectrum. Similarly, the effective radius is related to the observed radius by $R_{\text{eff}} \propto R_{\text{obs}} f_c^2$. The color correction factor may vary between 1.4 and 1.7 for luminosities approaching the Eddington limit (Suleimanov, Poutanen, and Werner, 2011). Therefore at the peak of Burst 2, the blackbody temperature may be a factor of ~ 0.6 lower than that observed, and the blackbody radius a factor of ~ 3 larger.

The behavior described above is the signature of a “touchdown” event wherein the photosphere undergoes expansion due to radiation pressure, then rapidly falls back down to the surface such that luminosity remains constant while the contraction causes the temperature to increase. We therefore conclude that the NS underwent PRE during Burst 2. Because this phenomenon is generally attributed to the balance of radiation pressure and gravitational force at the Eddington limit ($L_{\text{Edd}} \sim 2 \times 10^{38} \text{ erg s}^{-1}$ for a NS with typical mass $M = 1.4 M_{\odot}$), it is often assumed that PRE allows for the measurement of the source distance. We defer estimation of the distance and further discussion until Section 4.6.

4.5 Timing Analysis

We searched both the persistent and burst emission for timing features including quasi-periodic and coherent oscillations. We began by producing cross-spectra between FPMA and FPMB for $113 \times 256 \text{ s}$ intervals included in the persistent GTI described in Section 4.4. We analyzed the cospectrum, the real part of the cross-spectrum, due to its advantages described by Matteo Bachetti, Harrison, et al. (2015), namely the fact that it eliminates contributions to the power spectrum introduced by Poisson noise and dead time, the latter of which can be significant even for moderate NuSTAR count rates. In order to produce the cospectra, we used Stingray to produce light curves using only events within the $100''$ source extraction region and with energy between 3 and 78 keV. We binned the light curves with a resolution of 2048^{-1} s , and ensured that the light curves were simultaneous between FPMA and FPMB.

We inspected the resulting dynamical cospectrum as well as the averaged cospectrum

to look for coherent signals, particularly around the previously detected signal at 589 Hz (Strohmayer et al., 1997). There is no indication of such a feature, and the cospectrum of the persistent emission does not appear to deviate from a simple power law. We confirmed this visual inspection by performing a chi-squared fit to a power law model, which yielded a reduced chi-squared of $\chi^2/\text{d.o.f.} = 0.98$. Nonetheless, we performed an automated search for QPO features by fitting the average cospectrum to a power law with an added Lorentzian feature, such that the total model is given by

$$f(\nu) = A\nu^\alpha + B \left(\frac{1}{\pi} \right) \left[\frac{\gamma}{(\nu - \nu_0)^2 + \gamma^2} \right] \quad (4.4)$$

where $f(\nu)$ is the rms-normalized spectral power density at frequency ν , A is the normalization of the power law component, α is the power law index, B is the integrated power underneath the Lorentzian component, ν_0 is the frequency at the peak of the Lorentzian component, and γ gives the width of the Lorentzian and is related to the quality factor by $Q \equiv \frac{\nu_0}{2\gamma}$. We scanned ν_0 over the frequency range, bounded on the lower end by the length of the intervals, and bounded on the upper end by the Nyquist frequency, equal to twice the binning frequency. For each value of ν_0 , we fit the average cospectrum to the model described by Equation 4.4, allowing all parameters aside from ν_0 to vary, and compared the resulting χ^2 fit statistic to the statistic attained by fitting the cospectrum to a power law alone. This produced a $\Delta\chi^2$ distribution over the range of allowed frequencies. The greatest fit improvement is $|\Delta\chi^2| < 12$, compared to a baseline statistic of $\chi_0^2 = 2.5 \times 10^5$, indicating that the addition of a Lorentzian signal to the underlying power law spectrum is not warranted. We nonetheless attempted to fit QPO signals at several peaks in the $|\Delta\chi^2|$ distribution, this time allowing ν_0 to vary. We found that none of these signals had significance greater than 1.7σ , where significance is defined as the ratio of the integrated power under the Lorentzian to the error of the power, B/σ_B .

We performed a similar analysis for the burst emission as well as a more focused search for QPOs in two 10 ks intervals preceding each burst. We produced cospectra for 115×1 s intervals during Burst 1 and 98×1 s intervals during Burst 2, and averaged all 213 cospectra together. We note that for the purposes of timing analyses, we extended each of the burst GTIs by 75 s in order to include the burst decays. For the pre-burst emission, we produced a total of 34 cospectra, each corresponding to an interval of 256 s, 18 of which precede Burst 1 and 16 of which precede Burst 2. We

averaged over each of the pre-burst epochs separately, and, prompted by the work of Revnivtsev, Churazov, et al. (2001), we filtered the pre-burst emission to include only photon energies in the range 3-12 keV. Following the QPO search method we described for the persistent emission yields similar results: we do not significantly detect QPOs at any frequency during the bursts nor during the pre-burst intervals.

We also investigated the burst cospectra for evidence of coherent oscillations corresponding to a spin period. Visual inspection of both the dynamical and averaged (across both bursts) cospectra does not indicate the presence of coherent oscillations. We find a 99% confidence upper limit of 16% for the fractional rms integrated between 588 Hz and 590 Hz, exclusive.

We further searched for burst oscillations by performing a dynamical epoch-folding search on the burst emission. We analyzed each burst in 1 second intervals, stepping through the bursts in 0.5 second increments, resulting in overlapping time bins. For each focal plane module we produced pulse profiles corresponding to a range of oscillation frequencies near 589 Hz. We folded only events between 3 and 12 keV, again restricting our analysis to events within the source extraction region used described above. The resulting pulse profiles were further corrected for variations in dead time using the method described in Kristin K. Madsen, S. Reynolds, et al. (2015). For each corrected pulse profile we calculated the Z_2^2 statistic (Buccheri et al., 1983) as well as the corresponding probability that each of these statistics was not produced by noise. For each burst, we were thus left with two distributions, one for FPMA and another for FPMB, of the probability of detection of oscillations over a range of frequencies. We did not find any significant signal at any time during the bursts, and those spurious signals which we did observe only appeared in a single focal plane module.

4.6 Discussion

Explaining the double-peaked burst

Both of the type-I X-ray bursts which we have presented exhibit interesting bursting behavior. Burst 1 does not adhere to the canonical fast-rise exponential-decay structure of most type-I bursts, instead showing a double-peaked structure. In some cases, bursts which show multiple peaks in their observed count rates have been shown to be associated with PRE (W. H. G. Lewin, Vacca, and Basinska, 1984), however we do not observe evidence for PRE during Burst 1, as the bolometric luminosity exhibits the same double-peaked structure as the count rate. Burst 1 is

instead more similar to the multiple-peaked non-PRE bursts observed in sources like 4U 1608–52 (Penninx et al., 1989; Jaisawal et al., 2019), GX 17+2 (Kuulkers, Homan, et al., 2002), and 4U 1636-536 (Sztajno et al., 1985; J. van Paradijs et al., 1986; Bhattacharyya and Strohmayer, 2006).

Even among this class of multiple-peaked bursters there is some inhomogeneity. The burst observed by Jaisawal et al. underwent rebrightening about 5 s after burst onset, resulting in a double-peaked light curve where the second burst reached about half of the count rate as the first peak. The authors presented several possible physical explanations including a stalled burning front, waiting points in the rp-process, and reburning of material. While the double-peaked burst which we have observed bears some dissimilarities with the double-peaked burst of 4U 1608–52, these mechanisms could also explain the behavior of Burst 1.

In the case of GRS 1741.9–2853, we have shown that the sub-bursts were characterized by quite different rise and decay times, and that the second sub-burst actually exceeded the peak luminosity of the first. Additionally, whereas Jaisawal et al. found that the blackbody temperature reached its peak during the dip in brightness between sub-bursts at the same time that blackbody radius reached a minimum, we find that the blackbody temperature closely tracks the luminosity, while appearing to show a slight anti-correlation with the blackbody radius. This is reminiscent of the double- and triple-peaked bursts originating from 4U 1636-536.

Similarly to the scenario presented by Sztajno et al. and van Paradijs et al., the first sub-burst may have been the result of a “failed,” slowly igniting type-I burst which did not manage to spread across the entirety of the NS surface, followed by a second type-I burst which ignited much more quickly and enveloped a larger fraction of the NS surface. Alternatively, the double-peaked structure we observed may be the result of a single burning front which stalled as it traveled from the NS pole towards the equator. Bhattacharyya & Strohmayer have shown that models of burning front propagation are able to reproduce the qualitative features observed during a double-peaked burst in 4U 1636-536. Indeed, the shape and spectral evolution of the burst they present strongly resembles those of Burst 1. A third possibility is the stalling of burning due to waiting points in the process of thermonuclear burning (Fisker, Thielemann, and Wiescher, 2004). Detailed physical modeling is required to compare the viability of these scenarios, however this is beyond the scope of this paper.

Table 4.4: Comparison of PRE bursts presented in this work and in Barrière et al., 2015.

Reference	$F_{\text{pers}}^{\text{a}}$ (10^{-11} erg cm $^{-2}$ s $^{-1}$)	$F_{\text{peak}}^{\text{b}}$ (10^{-8} erg cm $^{-2}$ s $^{-1}$)	X^{c}	$L_{\text{Edd}}^{\text{d}}$ (10^{38} erg s $^{-1}$)	d^{e} (kpc)
Barrière et al., 2015	$8.04^{+0.38}_{-0.35}$	$3.58^{+0.29}_{-0.28}$	0 0.7	3 1.7	8.3 ± 0.7 6.3 ± 0.5
This work	130 ± 2	$2.94^{+0.28}_{-0.26}$	0 0.7	3 1.7	9.0 ± 0.5 7.0 ± 0.4

^a Unabsorbed bolometric flux calculated for the period leading up to the burst. This period corresponds to epoch O4 in Barrière et al., 2015 and to the final four orbits of the observation presented in this work.

^b Unabsorbed bolometric flux calculated for time slice corresponding to the peak of the burst.

^c Hydrogen mass fraction assumed when calculating the Eddington luminosity.

^d Eddington luminosity calculated using Equation 4.6

^e Distance calculated assuming that the peak flux corresponds to the Eddington luminosity.

Photospheric Radius Expansion

Our analysis of the spectral evolution of Burst 2 revealed that the burning material underwent a process of rapid expansion and contraction. We have interpreted this behavior as evidence for PRE, during which the burning material reached the Eddington luminosity and was therefore momentarily lifted from the NS surface by radiation pressure. The evolution of the blackbody radius, temperature, and luminosity strongly resembles the PRE burst observed by Barrière et al. (2015), with the major difference being the overall shorter timescales observed in Burst 2 compared to the Hydrogen-rich burst observed by those authors.

Compared to the burst observed by Barrière et al., the short rise and decay time observed for Burst 2, in addition to the relatively high persistent flux leading up to the burst (see Table 4.4) may indicate that at the time of observation the source was in the stable H-burning regime. In other words, while the accreted material is likely to contain a mixture of H and He, the accreted H burns stably on the NS surface rather than leading to runaway thermonuclear burning. This in turn leads to pure He bursts (Trap et al., 2009). In addition to the burst structure and persistent flux, the recurrence timescale and burst fluence provide further evidence for pure He burning during Burst 2. The recurrence timescale, τ_{rec} , and the mass accretion rate, \dot{m} , can be combined to calculate the ignition column: $y_{\text{ign}} = \dot{m}\tau_{\text{rec}}(1+z)^{-1}$. Next, the energy released per unit mass, ϵ_{nucl} , can be calculated using the relation

$\epsilon_{\text{nuc}} = E_b(1+z)/(4\pi R_{\text{NS}}^2 y_{\text{ign}})$, where E_b is the total energy radiated during the burst and is related to the burst fluence, f_b , by $E_b = 4\pi d^2 f_b$. We may combine the relations listed above with Equation 4.3 to obtain an equation for ϵ_{nuc} which does not depend on the distance to the source but rather on the ratio of the observed burst fluence to the integrated persistent flux:

$$\begin{aligned} \epsilon_{\text{nuc}} = & 2.44 \times \left(\frac{f_b}{10^{-7} \text{ erg cm}^{-2}} \right) \left(\frac{\tau_{\text{rec}}}{10^4 \text{ s}} \right)^{-1} \\ & \times \left(\frac{F_{\text{bol}}}{10^{-9} \text{ erg cm}^{-2} \text{ s}^{-1}} \right)^{-1} \times 10^{18} \text{ erg g}^{-1} \end{aligned} \quad (4.5)$$

for a NS with $M = 1.4M_{\odot}$ and $R_{\text{NS}} = 10 \text{ km}$. Due to the orbital gaps in the observation, we were only able to determine an upper limit on the recurrence timescale, $\tau_{\text{rec}} \lesssim 4 \times 10^4 \text{ s}$. Integrating the blackbody flux during Burst 2 gives a burst fluence of $f_b = (2.8 \pm 0.1) \times 10^{-7} \text{ erg cm}^{-2}$. Thus we arrive at an energy per unit mass of $\epsilon_{\text{nuc}} \gtrsim 1.4 \times 10^{18} \text{ erg g}^{-1}$ or an energy per nucleon of $Q_{\text{nuc}} \gtrsim 1.4 \text{ MeV nucleon}^{-1}$. Given $Q_{\text{nuc}} = (1.35 + 6.05X) \text{ MeV nucleon}^{-1}$ (Goodwin, Heger, and D. K. Galloway, 2019), this corresponds to a H fraction, X , consistent with zero.

With this in mind, we may calculate the distance to the source. The Eddington luminosity as measured by a distant observer is given by (Walter H. G. Lewin, Jan van Paradijs, and Taam, 1993)

$$\begin{aligned} L_{\text{Edd},\infty} = & \frac{4\pi cGM}{\kappa_0} \left[1 - \frac{2GM}{Rc^2} \right]^{1/2} \\ & \times \left[1 + \left(\frac{kT}{39.2 \text{ keV}} \right)^{0.86} \right] (1+X)^{-1} \end{aligned} \quad (4.6)$$

where κ_0 is the opacity for pure He and is given by $\kappa_0 = 0.2 \text{ cm}^2 \text{ g}^{-1}$, M is the mass of the accretor, R is the radius at which the Eddington luminosity is being calculated, T is the temperature of the material at touchdown, and X is the hydrogen mass fraction of the material, which we assume to be zero. We assume a typical NS mass of $M = 1.4M_{\odot}$, and because the peak flux is achieved at the time of touchdown when the burning material is assumed to have returned to the NS surface, we similarly assume a typical NS radius of $R = 10 \text{ km}$. The temperature, T , that appears in Equation 4.6 is that of the material in the emission reference frame. In reality, the temperature measured by a distant observer via fitting to a blackbody differs from the temperature in the frame of the emitting material, $T_{\text{emit}} = (1+z)f_c^{-1}T_{\infty}$. Given a

temperature at touchdown of $kT_\infty = 2.44$ keV, a redshift of $(1+z) = 1.31$ (see Section 4.4), and a color correction factor of $f_c = 1.7$, we arrive at an Eddington luminosity of $L_{\text{Edd},\infty} = 3 \times 10^{38}$ erg s⁻¹. Combined with our measured peak unabsorbed, bolometric flux of $F_{\text{peak}} = 2.94^{+0.28}_{-0.26} \times 10^{-8}$ erg cm⁻² s⁻¹, this corresponds to a distance to the source of $d = 9.0 \pm 0.5$ kpc.

This result is consistent with previous estimates which have placed the source at distances ranging from 5 kpc to 9 kpc depending upon the assumed material composition and the method of calculating the Eddington luminosity (Cocchi et al., 1999; Duncan K. Galloway, Michael P. Muno, et al., 2008; Trap et al., 2009; Barrière et al., 2015). Our measurement lies on the most distant end of these estimates. This could be the result of a number of effects. As we have shown, the material composition has a significant effect on the Eddington luminosity and therefore on any measurement of the distance. For example, if we assume solar composition, $X = 0.7$, rather than pure He burning, the resulting distance is $d = 7.0 \pm 0.4$ kpc. In order to remain consistent with our measurements of the burst fluence, this would require a recurrence time which is a factor of ~ 4 smaller than the time which elapsed between Burst 1 and Burst 2. This in turn would imply that an additional burst took place during one of the orbital gaps of the observation. It is interesting to note that the peak flux we have observed is nearly consistent with the peak flux presented by Barrière et al., while the structures of the corresponding bursts are very different. This may represent a challenge to the method of inferring the composition of burning material via light curve analysis alone.

Throughout this paper we have assumed isotropic emission when calculating burst and persistent fluxes. However, the inclination of the system can have a significant effect on the actual values of these quantities (Duncan K. Galloway, Psaltis, et al., 2003). Spectral modeling of the persistent emission suggests that the inclination of the inner disk is less than 30°. Depending upon the disk geometry, this may result in an overestimate of the burst flux by a factor of 1.5 – 2, and of the persistent flux by up to a factor of 2.5 (He and L. Keek, 2016). Therefore, the distance may be underestimated, both in this work and in previous work which also assumed isotropic emission, by a factor of up to $\sqrt{2}$. The bursting behavior presented by Trap et al. (2009) indicates a possible correlation between peak flux and burst fluence. We therefore speculate that those bursts could actually have achieved the same peak luminosity (modulo composition effects) which only appeared to vary due to changes in inclination. However, because Trap et al. are unable to claim that the

bursts undergo PRE, it may not be appropriate to assume that the bursts reached the Eddington luminosity, meaning that this interpretation may not be accurate. Future investigations of the long-term variability of GRS 1741.9–2853 could reveal whether changing disk inclination has a significant impact on the measured peak flux of PRE bursts.

4.7 Summary and Conclusions

We have presented light curve, spectral, and timing analyses of two type-I X-ray bursts as well as persistent emission originating from the source GRS 1741.9–2853 during a period of outburst observed by NuSTAR. This represents the first time the source has been observed by NuSTAR at such a high persistent flux — the source was over 15 times brighter than during the previous NuSTAR observation which took place in 2013 — which allowed us to analyze the bursting behavior in an accretion regime previously unexplored by NuSTAR for this source. Additionally, because we observed two bursts, we were able to obtain an upper limit on the recurrence timescale between the bursts, $\tau_{\text{rec}} \lesssim 4 \times 10^4$ s. This upper limit is half of the shortest recurrence time previously reported between bursts originating from GRS 1741.9–2853 (Trap et al., 2009), and the measurement of the recurrence time served as an additional piece of evidence that the burning material was H-deficient. Aside from the two bursts, the source appeared to show only slight variability. We confirmed this by analyzing the cospectra taken between light curves observed by the two focal plane modules. In all cases we found the cospectra to be relatively featureless, being described well by a single power law model. Additionally, we performed an epoch-folding analysis which did not produce evidence for coherent burst oscillations.

We found that the spectra of the persistent emission were modeled well by an absorbed blackbody plus upscattered emission originating from a hot corona or accretion flow, in addition to Fe $K\alpha$ emission which can be modeled either phenomenologically using a simple Gaussian emission line or self-consistently using relativistic disk reflection models. Having modeled the persistent emission, we were able to perform a time-resolved spectroscopic analysis on each of the type-I bursts. We found that the first burst exhibited a double-peaked structure, and we showed that the structure we observed did not appear to result from the rebrightening of an ongoing burst but rather could be described as two “sub-bursts” occurring in quick succession. This is the first confirmed case of such a burst originating from GRS 1741.9–2853, placing it within a population of only a handful of multiple-

peaked bursters.

The first burst was significantly less bright and energetic than the second burst, which exhibited a canonical fast-rise exponential decay structure in addition to an extended tail. Spectroscopic analysis showed that the blackbody describing the emission during the second burst underwent a period of rapid contraction accompanied by a rise in temperature, all occurring at a constant luminosity. We therefore inferred that the source had undergone photospheric radius expansion, or PRE, which typically implies that the source has reached the Eddington luminosity. Based on this assumption, we calculated a distance to the source of $d = 9.0 \pm 0.5$ kpc, which is somewhat larger than, but still consistent with, previous estimates. However, the value of the Eddington luminosity depends strongly on the composition of the burning material. While the observed properties of the burst as well as the persistent flux and recurrence timescale are consistent with pure He burning, it is not possible to determine the composition with absolute certainty. Future observations type-I X-ray bursts originating from GRS 1741.9–2853 may provide additional opportunities to determine how the composition of burning material varies with persistent flux and how this affects bursting behavior, as well as whether changing disk inclination is responsible for variation in peak flux between PRE bursts at different times.

*Chapter 5***MAXI AND NUSTAR OBSERVATIONS OF THE FAINT X-RAY TRANSIENT MAXI J1848–015 IN THE GLIMPSE-C01 CLUSTER**

Pike, Sean N. et al. (Mar. 2022). “MAXI and NuSTAR Observations of the Faint X-Ray Transient MAXI J1848-015 in the GLIMPSE-C01 Cluster”. In: *ApJ* 927.2, 190, p. 190. DOI: 10.3847/1538-4357/ac5258. arXiv: 2202.02883 [astro-ph.HE].

5.1 An unknown X-ray transient in outburst**X-ray binaries in outburst**

Compact objects, such as neutron stars (NS) and black holes (BH), orbiting main sequence stars often undergo cycles of outburst and quiescence due to modulation in the rate at which matter from the companion star accretes onto the compact object. Matter falls from the surface of the companion into the orbit of the compact object via Roche-lobe overflow or stellar winds (also known as Bondi-Hoyle accretion). According to the Disk Instability Model (Lasota, 2001), this material eventually reaches a critical density at which angular momentum can be transported efficiently outward, resulting in the formation of an accretion disk (Shakura and R. A. Sunyaev, 1973). This disk may reach all the way down to the surface or inner-most stable circular orbit (ISCO) of the compact object. As the gravitational potential energy of the accreting material is converted into heat, the innermost regions of the disk can reach temperatures of order 10^7 K, emitting photons with energy exceeding thousands of electron volts, hence these systems are referred to as X-ray binaries. This cycle of transient disk accretion leads to a variety of observable phenomena. The X-ray spectra of accreting NSs and BHs vary between a low-luminosity hard state and a brighter soft state, with intermediate states in between. During the hard state, emission is dominated by a power-law-shaped component which originates from a region of hot plasma near the central accretor known as the corona, while the soft state spectrum is dominated by thermal emission from the inner regions of the disk.

Additional spectral features result from the disk geometry in an X-ray binary. Iron in the disk may be irradiated by coronal emission and fluoresce, giving rise to emission lines around 6.4 keV. Line emission originating from the inner regions of the disk

may be blurred by Doppler shifts due to the rapid orbital motion of the disk material and by the strong gravitational potential near the central compact object. Furthermore, soft photons from the corona may undergo Compton upscattering resulting in a “Compton hump” in the spectrum at high energies. These “reflection” features encode information regarding the inner disk radius, R_{in} , and the spin parameter, a , of the central accretor. Spectral models such as `relxill` (T. Dauser et al., 2014; J. García, T. Dauser, Lohfink, et al., 2014), which self-consistently model relativistic disk reflection, are therefore important tools for probing the properties of X-ray binaries, and can help us to differentiate between NS and BH accretors.

MAXI J1848–015

Each year, the Monitor of All-sky X-ray Image, or MAXI (Matsuoka et al., 2009), discovers dozens of X-ray sources. Among these sources are accreting black holes, neutron stars, and white dwarfs. Follow-up with other X-ray observatories can help to elucidate the nature of these sources and lays the groundwork for their future study.

One such source, MAXI J1848–015, was discovered with the MAXI/GSC on December 20, 2020 (Takagi et al., 2020). The MAXI/GSC nova alert system (Hitoshi Negoro et al., 2016) triggered on the source at 05:04 (all times are given in UT), and the source flux was found to be increasing. The average X-ray flux on eight scan transits from 00:25 to 11:16 on December 20 was 63 ± 10 mCrab in the 4–10 keV band. The MAXI 90% confidence region had a radius of about 0.3 deg and was consistent with the previously detected ASCA source AX J1848.8-0129 (Sugizaki, Mitsuda, et al., 2001). Since the source had an angular separation of 26 deg from the Sun at the time of detection, neither the Neil Gehrels Swift Observatory X-ray Telescope (Swift/XRT, Gehrels et al., 2004; Burrows et al., 2005b) nor the Neutron Interior Composition Explorer Mission (NICER, Gendreau and Arzoumanian, 2017) could observe the source.

However, the Nuclear Spectroscopic Telescope Array, or NuSTAR (Harrison et al., 2013), was able to perform follow-up observations of the source despite its angular proximity to the Sun. NuSTAR performed tiling observations to search the MAXI error region, and the source was detected during the first pointing. The source exhibited a soft spectrum, and although the source position was further refined to a region with radius $\sim 90''$, it could still not be distinguished from AX J1848.8-0129 with certainty (Pike, Harrison, Forster, et al., 2020). Soon after the NuSTAR ToO

observations, on December 23, the 2–10 keV source flux rapidly decreased in a day from about 40 mCrab to less than 15 mCrab (H. Negoro et al., 2020). About a week later, the source was again observed by NuSTAR, this time exhibiting a much harder spectrum (T. Mihara et al., 2021).

By the end of February 2021, MAXI J1848–015 was far enough from the Sun that it could be observed by other instruments. Thereafter, the source was localized by both Swift/XRT and the Chandra X-ray Observatory (Chandra, Weisskopf et al., 2000b) to 90% confidence regions of $\pm 2.3''$ (Kennea et al., 2021) and $\pm 0.8''$ (Chakrabarty et al., 2021), respectively, while radio observations further refined the source position to $\alpha(\text{J2000}) = 18\text{h } 48\text{m } 49.824\text{s} \pm 0.003\text{s}$, $\delta(\text{J2000}) = -01^\circ 29' 49.99'' \pm 0.05''$ (Tremou et al., 2021).¹ Interestingly, the radio position is coincident with a relatively bright NIR counterpart (Hare, Yang, et al., 2021). Around the same time, NICER observations of the source were performed and Miller, Sanna, et al. (2021) reported a number of emission lines in the Fe K band and a flux of about 1 mCrab.

Importantly, the precise localization of the source confirmed that MAXI J1848–015 is not consistent with the previously reported position of AX J1848.8-0129, and that it is spatially coincident with, and likely resides in, the core of the Galactic cluster GLIMPSE-C01 (GC01 hereafter). This cluster was originally discovered by Kobulnicky et al., 2005, who suggested that the cluster was an old globular cluster passing through the Galactic disk at a distance of 3.1 – 5.2 kpc. Several subsequent studies have alternatively suggested that GC01 is a young or intermediate age massive cluster candidate with an age between 0.3 – 2.5 Gyr (Davies et al. 2011; Davidge et al. 2016). More recently, Hare, Kargaltsev, and Rangelov, 2018 reported on Hubble Space Telescope observations of GC01, which they used to estimate a cluster distance of ~ 3.3 kpc and a cluster age of > 2 Gyr by studying the absolute magnitudes of red clump stars in the cluster. Unfortunately, the cluster’s large source density, strong differential reddening across the cluster (ranging between $A_V = 14 - 22$), and unknown metallicity make it difficult to more precisely constrain the cluster’s age (Hare, Kargaltsev, and Rangelov, 2018).

In this paper, we present the results of MAXI monitoring of MAXI J1848–015 as well as spectral and timing analysis of the two NuSTAR observations performed following the detection of the source by MAXI. In Section 5.2, we describe the MAXI observations in detail, including the shape and duration of the outburst. In Section 5.3, we discuss the NuSTAR observations of the source, beginning

¹The authors do not specify whether the uncertainties represent 1σ or 90% confidence regions.

with a description of the observations and data reduction and continuing onto an investigation of the source spectra as well as the results of reflection modeling applied to these spectra in Section 5.3. Next, we present an analysis of the timing properties of the NuSTAR light-curves in Section 5.3. Finally, in Section 5.4, we discuss what our results mean in regards to the questions of whether the source is a neutron star or a black hole accretor and how its particularly low luminosity can be understood in the context of disk accretion.

5.2 MAXI Observations

Observations and data reduction

MAXI has been monitoring about 85% of sky every 92 minutes with the Gas Slit Cameras, GSCs, in the 2–20 keV band since August 2009 (Tatehiro Mihara et al., 2011; Sugizaki, Tatehiro Mihara, et al., 2011). The GSCs have two wide fields of view of $1.5^\circ \times 160^\circ$ to the horizontal and zenith directions, and typically observe a source for 40–100 seconds every 92 minutes as the International Space Station (ISS) orbits Earth.

In December 2020, the GSC_1, GSC_2, GSC_4, GSC_5, and GSC_7 cameras and the degraded GSC_3 and GSC_6 cameras were operating. The source was detected by all these detectors, but in these analyses we only used those obtained with the well-calibrated GSC_4 and GSC_5 cameras with a high voltage of 1650 V and GSC_2 and GSC_7 cameras with 1550 V.

We employed a point-spread function (PSF) fit method to obtain MAXI/GSC light-curves with the best signal-to-noise ratios (Morii et al., 2010). The count rate in each light-curve bin was obtained by fitting an image with the PSFs of the GSCs taking into account the presence of nearby sources such as the high-mass X-ray binary AX J1846.4-0258 (1.60 degree separation) and the Super-giant Fast X-ray Transient IGR J18483–0311 (1.68 degree separation). On the other hand, the nearby transient sources in quiescent states, including Swift J185003.2–005627 (0.64 deg), GS 1843–02 (0.93 deg), and Swift J1845.7–0037 (1.11 deg), were ignored. AX J1848.8–0129 (0.012 deg \approx 0.74 arcmin) was also excluded. We note that AX J1848.8–0129 is originally named as AX J184848–0129 (Sugizaki, Mitsuda, et al., 2001), and its position has about 1 arcmin uncertainty. We first produced 1-scan, 6-hr, and 1-day bin light-curves in the 2–4 keV and 4–10 keV bands, respectively. The 6-hr and 1-day bin data were obtained by fitting 4-scan and 16-scan image data, respectively. We then subtracted constant background components, mainly

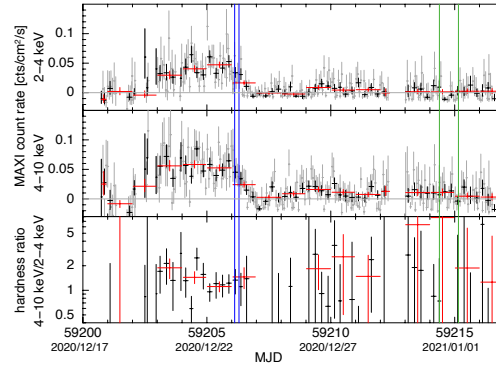


Figure 5.1: 2–4 keV and 4–10 keV light-curves (upper and middle panels) and their ratios (lower) of MAXI J1848–015 obtained with MAXI/GSC. Average fluxes in 1 scan (grey), 6 hours (black), and 1 day (red) are shown (1 scan data are omitted in the lower panel). The average 2–4 keV and 4–10 keV count rates for Crab are 1.065 and $1.172 \text{ ct cm}^{-2} \text{ s}^{-1}$, respectively. The blue and green lines are the start and end time of the first and second NuSTAR observations, respectively.

originating from the galactic ridge X-ray emission, as the average count rates from MJD 58000 (2017 September 4) to 58599 (2019 April 26) were consistent with zero. Finally, we obtained 2–10 keV curves by summing the background subtracted 2–4 keV and 4–10 keV curves.

As shown later, every ~ 92 days (the ISS precession period), when the source was at the right side of the GSC_2 and GSC_5, the source was obscured by the Space-X Crew-1 spacecraft attached on the Harmony module of the ISS for several days. We did not use data during the periods shown in the current calibration database (CALDB) and we also excluded data from 1 day before and after this period due to some ambiguity regarding the shape of the spacecraft shadow.

Long-term light-curve

Figure 5.1 shows the MAXI/GSC 2–4 keV and 4–10 keV light-curves and their ratio for MAXI J1848–015 obtained by the PSF-fit method. In the seven scan transits from 18:37 on December 18 to 01:12 on December 19 (MJD 59201.7763 – 59202.0501), the source was not visible on GSC images (Takagi et al., 2020). No count excess is recognized in each scan curve. The PSF-fit method provides two-sided 1σ errors based on the likelihood method (Morii et al., 2010). Fitting eight one-scan data points during the period with a constant model gives the average count rate of $-0.094 \pm 0.0128 \text{ ct cm}^{-2} \text{ s}^{-1}$. Using the size of this error, we estimate a

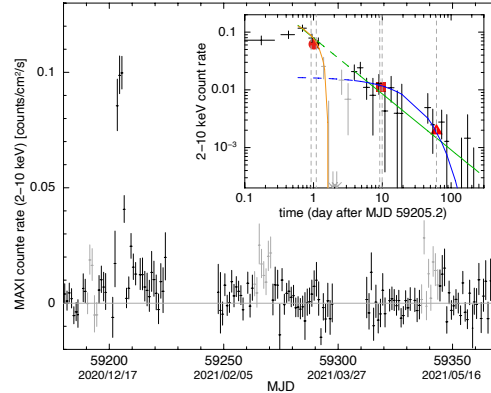


Figure 5.2: Long-term 2–10 keV light-curve of MAXI J1848–015 from MAXI. Unused data during interference with the Space-X Crew-1 spacecraft are also shown in grey. A logarithmically rebinned curve and the best fitting curves are also shown in the inset panel. The data during a dip shown in grey are not used in the fits (see Section 5.2). Observed fluxes for the two NuSTAR and Swift observations are indicated with the red filled circle, rectangle, and triangle, respectively, between the dashed lines showing the observation periods. The orange line shown in the inset represents a linear fit to the initial rapid decay, while the blue and green lines represent exponential and power law fits, respectively, to the observed second decay.

1σ upper limit of $0.0128 \text{ ct cm}^{-2} \text{ s}^{-1}$, $\sim 5.7 \text{ mCrab}^2$. This is consistent with a value 12 mCrab of a typical 3σ detection limit of 1 day of ~ 16 scans (Hitoshi Negoro et al., 2016). After the scan transit at 01:12 until 22:52 on December 19 (MJD 59202.05–59202.95), the GSC did not fully observe the source region due to Sun avoidance. During the three scan transits from 11:59 to 15:05, however, some count excess was recognized at the edge of the detectors, which suggests the outburst started between 02:22 and 11:59.

The light-curves and hardness ratios in Fig. 5.1 show that the 4–10 keV flux reached the peak in almost one day on December 20 (MJD 59203) followed by gradual spectral softening. On December 23, the 2–10 keV flux rapidly decreased to below the detection limit in one day (H. Negoro et al., 2020) from $0.117 \pm 0.016 \text{ ct cm}^{-2} \text{ s}^{-1}$ at MJD 59205.89 (the center time of the 6-hr bin) to $-0.003 \pm 0.009 \text{ ct cm}^{-2} \text{ s}^{-1}$ at 59206.86 (we note that background subtraction may result in nonphysical negative count rates). However, we note that the light-curve obtained during the first NuSTAR observation performed on December 23 indicates a flux increase during the 4 hour observation (see §5.3). This suggests that the rapid decrease observed by MAXI

²We adopt the 2–10 keV count rate and the flux for Crab as $2.237 \text{ ct cm}^{-2} \text{ s}^{-1}$ and $2.4 \times 10^{-8} \text{ erg cm}^{-2} \text{ s}^{-1}$, respectively.

Table 5.1: Log of NuSTAR observations presented in this paper.

Observatory	Observation ID	Start time (UTC)	Stop time (UTC)	Exposure (s)
NuSTAR	90601340002 (NuObs 1)	2020-12-23 02:53:36	2020-12-23 07:06:26	9805
NuSTAR	90601341002 (NuObs 2)	2020-12-31 09:08:34	2021-01-01 03:40:01	36395

on December 23 is not simply due to the occultation by the companion. This flux drop continued until around December 26.0 (MJD 59209.0), and the 4–10 keV flux increased again, possibly prior to an increase in the 2–4 keV flux.

We plot long-term variations in the flux of MAXI J1848–015 in Figure 5.2. The data when the source is hidden by the Space-X Crew-1 spacecraft are not used and shown in grey. GIS images for the duration show extended enhancement around the source region. The origin of the enhancement is unknown, but it is difficult to consider that it is intrinsic to the source because of the periodicity closely connected with the interference and the extended image even though there is still some ambiguity in the shadow shape of the spacecraft.

We also show the 2–10 keV light-curve with a logarithmic time axis from the time December 22 04:48 (MJD59205.2 $\equiv T$) in the inset panel in Fig. 5.2. We fit the decay with three different models: a linear decay, an exponential decay, and a power law decay. The linear fit to the putative rapid decay starting at $t_0 (\equiv t - T) = 0.69$ d (=MJD 59205.89) is shown by the orange solid line. After $t_0 = 3.92$ d the flux exhibited an exponential (blue curve) or a power law (green) decay. Fitting the data for $t_0 \geq 3.92$ d with an exponential function gives a time constant of 28.0 ± 9.4 d (shown by the blue solid line and its extrapolation by the dotted line). Fitting the flux decrease from $t_0 \geq 0.69$ d to a power law function, we obtained a power law index of -0.97 ± 0.08 , shown by the green solid and dotted line, however we note that the result of the power law fit depends strongly on the choice of T .

5.3 NuSTAR Observations

NuSTAR, launched in June 2012, is the first high-energy focusing X-ray telescope (Harrison et al., 2013). It is composed of two focal planes, FPMA and FPMB, each paired with a set of focusing optics with a focal length of 10 m. The focal planes are each made up of 4 pixelated Cadmium Zinc Telluride (CZT) detectors, bonded to a set of custom readout electronics. NuSTAR has a resulting bandpass of 3–78 keV, making it a uniquely powerful tool for studying hard X-ray emission.

MAXI J1848–015 was first observed by NuSTAR on 2020 December 23. This

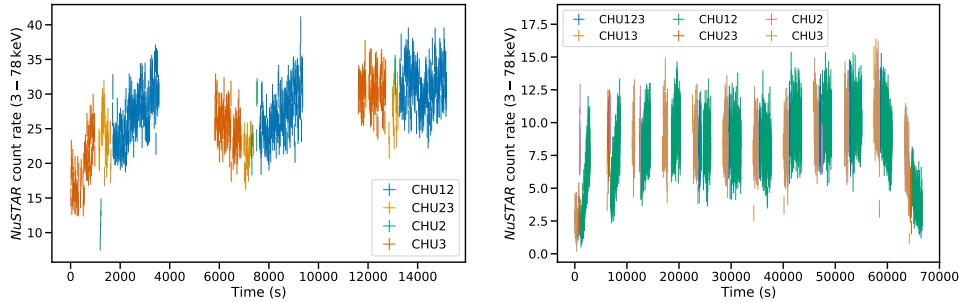


Figure 5.3: Background-subtracted 3-78 keV NuSTAR light-curve for each of the two observations, NuObs 1 (left) and NuObs 2 (right). The light-curves have been split into different CHU combinations. Time is measured in seconds since the observation start times listed in Table 5.1.

observation was taken with the goal of localizing the source, and was therefore broken down into 5 pointings, forming a mosaic which tiled the error region reported by MAXI. The source was detected by NuSTAR in the first of these pointings (OBSID 90601340002, PI Fiona Harrison), which had an exposure time of 9.8 ks. NuSTAR followed up on MAXI J1848–015 about a week later on 2020 December 31 (OBSID 90601341002, PI Fiona Harrison), after the source had dimmed. This observation had an exposure time of 36 ks. Hereafter we refer to these observations as NuObs 1 and NuObs 2, respectively. Table 5.1 lists the NuSTAR observations as well as their start and stop times and their total exposure times.

During both NuSTAR observations, MAXI J1848–015 was in close angular proximity to the Sun. This limits the aspect reconstruction as the primary Camera Head Unit (CHU) that NuSTAR uses to project counts onto the sky is blinded by the Sun. Instead, the ground software must make use of CHUs 1, 2, and 3 which are attached to the spacecraft bus. As a result, Mode 1 scientific data was unavailable. Instead, we analyzed Mode 6 scientific data, with which the source image cannot be perfectly reconstructed. This produces a source image with multiple centroids, each corresponding roughly to a different combination of CHUs. We reprocessed the unfiltered event files using NuSTARDAS v2.0.0 and CALDB v20200826. Next, we split the cleaned Mode 6 event files into event files corresponding to different combinations of CHUs 1, 2, and 3 using `nusplitsc` in the strict splitting mode. Figure 5.3 shows the background-subtracted light-curve for each NuSTAR observation, split into different CHU combinations.

For the purpose of extracting spectra, we used DS9 (Joye and Mandel, 2003b) to

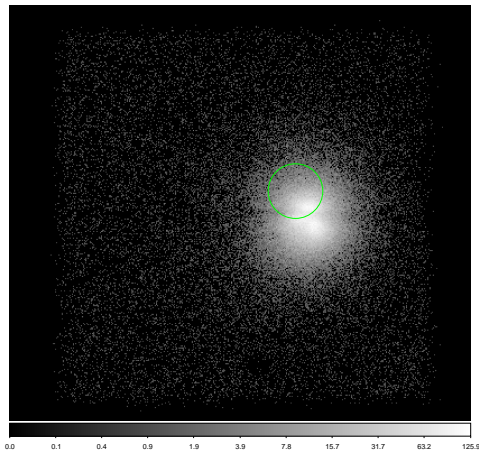


Figure 5.4: Summed Mode 6 data (all CHU combinations) from NuObs 1. The color bar is shown in units of counts. The source landed on the gap between detectors, and due to poor image reconstruction, multiple peaks in the count distribution are apparent. The green circle, which has a radius of $1'$, represents the ASCA error region for source AX J184848–0129 as reported by Sugizaki, Mitsuda, et al. (2001).

select circular source and background regions for each CHU combination. For NuObs 1, we chose source regions with radii equal to $60''$ and background regions with radii equal to $90''$. The centers of the source regions were determined using the automated centroid detection algorithm provided by DS9. During this observation, the source fell on the gap between detectors. Therefore, the source centroid fell on a different detector for different CHU combinations (see Figure 5.4). We chose background regions which fell on the same detectors as the source centroid for each CHU combination. This was not a concern when choosing source and background regions for NuObs 2 because the source did not fall near the chip gap. Due to the lower count rate and better pointing during this observation, we chose source regions with radii of $45''$ in order to reduce the contribution of background counts, and we again chose background regions with radii of $90''$.

Using `nuproducts` we extracted scientific products for each of these CHU combinations, essentially treating each as a separate observation. We then used the routine `addarf` to sum the resulting Ancillary Response Files, and the routine `addspec` to sum the resulting source spectra, background spectra, and Response Matrix Files. The final result for each observation was a single source spectrum, background spectrum, RMF, and ARF for each focal plane module. We used the spectral fitting package `Xspec` (v12.11.1 Arnaud, 1996) to analyze the spectra. In order to

determine best fit models, we used the W fit statistic (Wachter, Leach, and Kellogg, 1979), and the full NuSTAR band, 3–78 keV, was used for spectral fitting. Spectra were binned using the optimal binning procedure described by Kaastra and Bleeker, 2016. Spectra shown in figures have been further rebinned for clarity such that each bin has a significance of at least 5σ , with the exception of the highest-energy bins, each of which has a significance between 3σ and 4σ . All errors quoted represent 90% confidence intervals, and upper/lower limits represent 99% confidence intervals, unless otherwise stated.

We made significant use of the Python modules Scipy (Virtanen et al., 2020), Astropy (Astropy Collaboration, Thomas P. Robitaille, et al., 2013; Astropy Collaboration, Price-Whelan, Sipőcz, Günther, Lim, Crawford, Conseil, Shupe, Craig, Dencheva, Ginsburg, VanderPlas, et al., 2018b), Matplotlib (Hunter, 2007), Corner (Foreman-Mackey, 2016), and Stingray (Daniela Huppenkothen, Matteo Bachetti, Stevens, Migliari, Balm, et al., 2019). We used Astropy to easily read and write NuSTAR event and light curve files, we used Scipy to perform various calculations and curve fitting, and we used Stingray to calculate and analyze power density spectra. We used Matplotlib and Corner to produce plots of spectra, light-curves, power density spectra, and parameter distributions.

Spectral variability

NuSTAR revealed a stark spectral change between the first and second observations. The spectra are shown in Figure 5.5 along with their best-fit models. We found that the spectrum during NuObs 1 was significantly softer than that observed during NuObs 2. We therefore refer to the former as the “soft state” and the latter as the “hard state”. The spectra are described remarkably well by models which are frequently used to model the soft and hard states of accreting black holes and neutron stars: the continuum emission during the soft state is described well by an absorbed disk blackbody (`diskbb`) and a power law with index Γ , while the continuum emission during the hard state is described well by an absorbed power law with a high-energy cutoff, E_{cut} , which we modeled using `cutoffpl`. We modeled absorption using the `tbabs` model. We used cross-sections provided by Verner et al. (1996) and abundances provided by Wilms, Allen, and McCray (2000).

Each of the spectra exhibits broad emission lines around 6.4 keV corresponding to Fe $K\alpha$. Figure 5.6 shows the Fe line profiles which result from fitting the continuum emission while ignoring data bins between 5 and 8 keV. The broad,

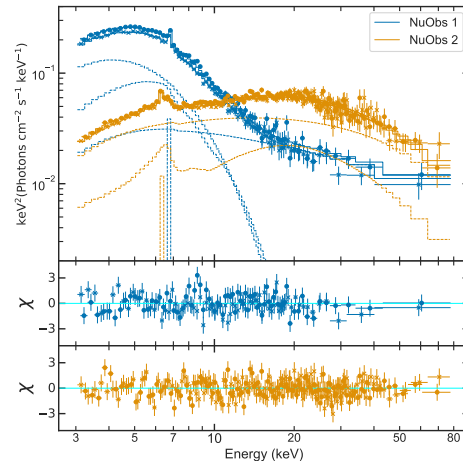


Figure 5.5: Soft state (blue) and hard state (orange) spectra with best fit models and model components shown with solid and dashed lines, respectively. FPMA spectra are shown with x's while FPMB spectra are shown with filled circles. The soft state spectrum is described well by a Comptonized disk blackbody, while the hard state spectrum does not require a disk component. Instead, the hard state spectrum is described well by a power law with a high energy cutoff. Both models are improved by the addition of relativistic disk reflection as well as a narrow Fe line component. The lower two panels show the residuals resulting from the model fits in units of $\chi = (\text{data} - \text{model})/\text{error}$.

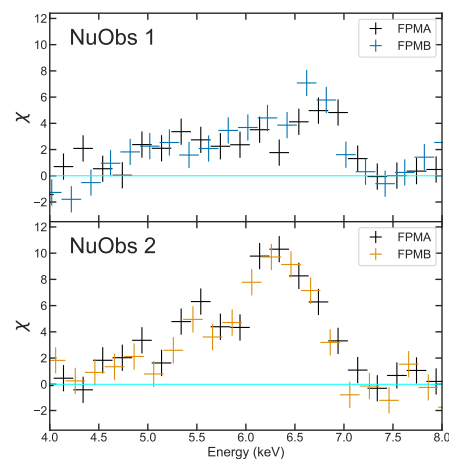


Figure 5.6: Broad Fe emission profiles in the soft state (top) and hard state (bottom) spectra. These residuals were produced by fitting the spectra to a simplified continuum model while ignoring data points in the range 5 – 10 keV. Significant changes to the shape of the profile can be seen between the two states with the peak growing stronger and shifting to lower energies during the hard state.

Table 5.2: Spectral parameters determined by performing a joint fit of the soft and hard state spectra in Xspec.

Model component	Parameter	Soft State (NuObs 1)	Hard State (NuObs 2)
tbabs	N_{H} (10^{22} cm $^{-2}$)	$4.2^{+0.2}_{-0.1}$	6.1 ± 0.2
gauss	μ (keV)	6.8 ± 0.1	6.3 ± 0.1
	K (10^{-5} Photon cm $^{-2}$ s $^{-1}$)	17.7 ± 0.4	$6.26^{+0.05}_{-0.07}$
	Equivalent Width (eV)	42 ± 3	42 ± 1
diskbb	kT_{in} (keV)	$1.38^{+0.02}_{-0.03}$...
	$(R_{\text{km}}/D_{10})^2 \cos i$	$6.4^{+0.2}_{-0.3}$...
nthcomp/cutoffpl	Γ	2.42 ± 0.04	$1.58^{+0.01}_{-0.02}$
	E_{cut} (keV)	...	28.9 ± 0.4
	Norm (10^{-3})	9.6 ± 0.4	$21.3^{+0.7}_{-0.8}$
relxillNS/relxilllp	h (R_{g})	...	5.7 ± 0.2
	a	0.967 ± 0.013	
	Inclination (deg)	26.4 ± 0.5	
	R_{in} (R_{g})	2.9 ± 0.2	$7.90^{+0.15}_{-0.16}$
	$\log(\xi/\text{erg cm s}^{-1})$	2.58 ± 0.06	$2.77^{+0.04}_{-0.02}$
	A_{Fe} (Solar)	$0.77^{+0.02}_{-0.01}$	
	$\log(N)$ (cm $^{-3}$)	< 15.3	...
	$f_{\text{refl}}^{\text{a}}$	0.61 ± 0.01	$0.83^{+0.02}_{-0.03}$
F_{bol} (10^{-10} erg cm $^{-2}$ s $^{-1}$) ^b		6.9 ± 0.1	2.85 ± 0.04
L_{bol} (10^{35} erg s $^{-1}$) ^c		9.1 ± 0.1	3.73 ± 0.05
W/d.o.f.		834/695	

^a We determined the reflection fraction by first fitting with the direct emission components included in the relxill models (i.e. with a positive value of f_{refl}), then we determined the normalizations of the direct components by freezing the reflection fractions and separating the direct and reflected components (with a negative value of f_{refl}).

^b Unabsorbed bolometric (0.1 – 100 keV) flux.

^c Bolometric (0.1 – 100 keV) luminosity assuming a distance of 3.3 kpc.

asymmetrical structure of the Fe line profiles led us to add relativistic disk reflection to the continuum models described above. We added a reflected component using relxilllp (T. Dauser et al., 2014; J. García, T. Dauser, Lohfink, et al., 2014) in order to self-consistently model emission originating from a hot corona with a lamppost geometry which irradiates and is reprocessed by a thin disk. We tied the power law index and high energy cutoff³ of each power law component to those of relxilllp. We found that this model was able to describe the the spectrum well, achieving a fit statistic of $W/\text{d.o.f.} = 449/323$ and $W/\text{d.o.f.} = 420/373$ (and a reduced Chi-squared test statistic of $\chi^2_{\nu} = 0.98$ and $\chi^2_{\nu} = 1.01$) for the soft and

³Because the soft state does not require a high-energy cutoff, we fixed the cutoff energy at 1000 keV, far beyond the upper edge of the NuSTAR bandpass.

hard states, respectively. However, the Fe line emission could not be fully accounted for, and residuals indicated the presence of a narrow line component. We therefore added a Gaussian component near 6.4 keV, and we froze its width at $\sigma = 10^{-5}$ keV, much narrower than the instrumental energy resolution. We allowed the strength and the centroid of the line to vary while fitting, and we found that the addition of this narrow line improved the fit by $\Delta W = -17.5$ and $\Delta W = -10.6$ for the soft and hard states, respectively, while decreasing the number of degrees of freedom by 2. We also found that the addition of this component led to better constraints on other parameters, such as the spin and the inclination, while still remaining consistent with their previous estimates.

In order to determine the statistical significance of the narrow components, we simulated 5000 spectra each for the soft and hard states, originating from the reflection models without narrow components. We then added a narrow component, again leaving the centroid energy and line strength free and fixing the width at $\sigma = 10^{-5}$ keV. By calculating the resulting improvement in the fit statistic for each simulation, we arrived at a false positive rate for the addition of a narrow component. We found that for the soft state, only one of these simulations was improved by more than $\Delta W = -17.5$, and for the hard state, 23 out of the 5000 simulations were improved by more than $\Delta W = -10.6$. In other words, we estimate a statistical significance of 3.7σ and 2.8σ for the addition of a narrow Fe component in the soft and hard state observations, respectively.

Finally, prompted by the clear presence of a hot thermal component, when modeling the soft state spectrum we replaced `relxilllp` with the sum of `nthcomp` (Zdziarski, Johnson, and Magdziarz, 1996; Życki, Done, and Smith, 1999), which models Comptonization of seed photons originating from a blackbody, and `relxillNS` (J. A. García, Thomas Dauser, et al., 2022), which models reflection of a blackbody spectrum rather than a power law. We tied the disk blackbody temperature to that of the seed photon temperature for both `nthcomp` and `relxillNS`, and we fixed the electron temperature of `nthcomp`, kT_e , at 1000 keV. We found that the fit was not affected by the type of seed blackbody specified for `nthcomp`, so for consistency we used a disk blackbody seed spectrum. We found that this model improved the fit ($\Delta W = -10$, $\Delta \text{d.o.f.} = 1$) when compared to the `relxilllp` model. We also tried modeling the hard state spectrum using a combination of a Comptonized disk blackbody with a reflected Fe line (`diskbb + nthcomp + relline1p`). We found that this model struggled to describe the hard state spectrum ($W/\text{d.o.f.} = 472/372$),

particularly at high photon energies (> 20 keV). It resulted in a photon index of $\Gamma = 1.8$ and an electron temperature of $kT_e = 9.1$ keV.

Having arrived at a suitable model for the spectra during both the soft (diskbb + nthcomp + relxillNS + gaussian) and hard (cutoffpl + relxillp + gaussian) states, we performed a Markov Chain Monte Carlo analysis in Xspec in order to explore the parameter space in detail. We used the Goodman-Weare algorithm (Goodman and Weare, 2010) with a chain length of 10^6 and a burn-in length of 10^5 . We initialized all walkers in a Gaussian distribution about the best fit parameters, with σ defined by the covariance matrix resulting from least-squares fitting. All spectral parameters are therefore given as the median values of the final posterior distributions, and the errors represent the bounds between which 90% of the samples lie.⁴ We found that both models recovered a high spin, $a > 0.7$, and an inner disk inclination angle around 25 deg. However there was significant degeneracy such that each model had valid solutions with different values for spin, disk inclination, inner disk radius, and other key parameters (see Appendix A for details regarding the individual fits). In order to break this degeneracy, we performed a joint fit wherein the inner disk inclination, the spin parameter, and the iron abundance were tied between the two spectral states.

Table 5.2 lists the median parameters for the joint fit resulting from the MCMC analysis described above, as well as the W -statistic of the best fit. Figure 5.5 shows the spectra as well as the best fit models and residuals for both the soft and the hard states. By performing a joint fit, we successfully narrowed the parameter space, resulting in a consistent solution across both the soft and hard states with a spin of $a = 0.967 \pm 0.013$ and an inclination of $i = 26.4 \pm 0.5$ deg.

The Fe $K\alpha$ emission line profile (Figure 5.6) shows clear evolution of the region responsible for this emission, with the peak shifting towards lower energies by about 0.5 keV and the overall profile becoming more pronounced as the source evolved from the soft to the hard state. Interestingly, we found that the centroid of the narrow Fe line during the hard state was less than 6.4 keV at the 95% confidence level. In other words, we detect a redshift in the narrow component at a significance of about 2σ . We also fit the data while freezing the centroid at 6.4 keV given that this is still consistent with our measurement of $\mu = 6.3 \pm 0.1$ keV, but this resulted in a somewhat degraded fit ($\Delta W = 3$; Δ d.o.f. = 1), and it led to significantly looser

⁴See Hogg and Foreman-Mackey (2018) for a discussion of best practices when interpreting the results of MCMC analyses.

constraints on parameters such as spin, inclination, and lamppost height.

The evolution of the accretion disk is further reflected in the best-fit relativistic reflection models, which suggest a significant increase in the inner radius of the accretion disk. This could constitute evidence for disk truncation in the hard state. In order to determine whether the choice of spectral model affects the apparent evolution of the inner disk radius, we performed a joint fit wherein the disk reflection features of both the soft and hard state spectra were modeled using `relxilllp` (rather than using `relxillNS/relxilllp` for the soft/hard states, respectively). For this fit, we tied the spin parameter, the inner disk inclination, and the Fe abundance between the soft and the hard states. This resulted in a slightly larger value for the inner disk radius in both states — $R_{\text{in}} = 3.4 \pm 0.2 R_g$ (where $R_g = GM/c^2$) for the soft state and $R_{\text{in}} = 8.6^{+0.5}_{-1.1} R_g$ for the hard state — but the radii remained significantly different, indicating that the evolution of the inner disk radius which we observe is independent of the choice of `relxillNS` or `relxilllp`.

The narrow Fe line components may be interpreted as distant disk reflection. Therefore we investigated whether non-relativistic reflection modeling could describe this component. We chose to use another member of the `relxill` suite, `xillver` (J. García and Kallman, 2010; J. García, T. Dauser, C. S. Reynolds, et al., 2013) for this component. In this model, the `relxill` and `xillver` components can be interpreted as reflection from the inner and outer regions of the disk, respectively. In the soft state, distant reflection, using either `xillver` or `xillverNS` to model reflection of the power law component or the blackbody component, respectively, is not able to fit the data as well as a simple Gaussian and results in a change in the fit statistic of $\Delta W = 10$.

For the hard state, replacing the Gaussian emission line with the distant reflection model did not change the fit statistic appreciably, but we found that the resulting parameters show significant degeneracies, such as between the disk inclination, the power law photon index, and the lamppost height. We tied the photon index, Γ , and the cutoff energy, E_{cut} , of the distantly reflected power law to those of the power law reflected from the inner disk, and we tied the iron abundance of the inner and outer disk but we allowed the ionization of the two components to vary independently. Given that we measured a centroid of $\mu = 6.3 \pm 0.1$ keV, slightly lower than the rest frame energy of the neutral Fe $K\alpha$ line, when modeling the narrow emission component using a Gaussian component, we also allowed the redshift of the outer disk component represented by `xillver` to vary.

Table 5.3: Timing properties of the source during each NuSTAR observation.

Observation	rms (10^{-3} – 10^{-1} Hz)	rms (0.1–10 Hz)	γ
NuObs 1	< 8%	< 15%	...
NuObs 2	$12 \pm 2\%$	< 14%	-2.1 ± 0.1

We found that this model was not sensitive to the inclination of the outer disk. When allowed to vary independently of the inner disk inclination the model preferred a high outer disk inclination of $i_{\text{out}} = 79_{-11}^{+6}$ deg ($\Delta i \equiv i_{\text{out}} - i_{\text{in}} = 57 \pm 10$ deg), but tying the inner and outer inclinations did not affect the fit statistic and resulted in an inclination which was closer to that resulting from the joint fits, $i = 22_{-5}^{+4}$ deg. In addition to a slightly smaller inclination angle, adding the `xillver` component while tying the inner and outer disk inclinations also resulted in an increased inner disk radius ($R_{\text{in}} = 14_{-5}^{+6} R_{\text{g}}$).

We also found that allowing the redshift of the `xillver` component to vary improved the fit by $\Delta W = -4$ compared to the same model with the redshift frozen at a value of zero. We measure a redshift of $z < 3.4 \times 10^{-2}$ at the 99% confidence level, corresponding to an upper limit on the line-of-sight velocity of the emitting region of $v < 10000 \text{ km s}^{-1}$, assuming a rest frame energy of 6.4 keV. We found that performing the same calculations using the posterior distribution of Gaussian centroids resulting from the joint fit produces upper and lower limits differing from these by less than 10%. The fit is slightly degraded by fixing the redshift to zero, but the main effect on the parameters is a decrease in the inner disk inclination by a few degrees. We note that the source is unlikely to experience a strong redshift due to the motion of the binary system, and it certainly does not experience cosmological redshift, but rather any observed strong redshift is more likely to be caused by motion of the emitting region itself. In Section 5.4, we discuss one scenario — that of ionized outflows — which could result in red- and blue-shifting of narrow emission.

Timing analysis

We investigated the source variability by producing cospectra (Matteo Bachetti, Harrison, et al., 2015) for each of the NuSTAR observations. We first corrected the photon times of arrival for the motion of NuSTAR using `barycorr`. We specified the *Chandra* source position reported by (Chakrabarty et al., 2021), and we used the JPL planetary ephemeris DE-430. In order to minimize the impact of the

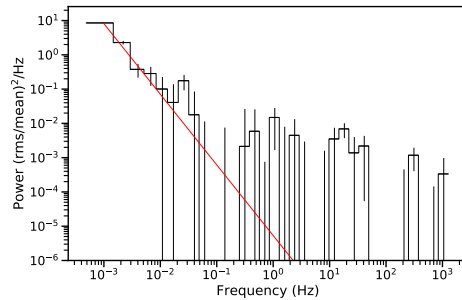


Figure 5.7: Averaged cospectrum calculated for the hard state NuSTAR observation, NuObs 2, using only CHU12 data. The cospectrum has been rebinned for clarity. The best-fit power law is shown in red. We did not find evidence for QPOs or pulsations.

motion of the source on the detectors on our timing analysis, we analyzed each of the CHU combinations separately. We split the event files into segments of length 1024 s, then binned the events with a time resolution of 2048^{-1} s in order to probe variability between 10^{-3} Hz and 10^3 Hz⁵. This range of frequencies allowed us to investigate both the low-frequency noise, and to search for any hint of pulsations potentially arising from a neutron star source. For each segment, we calculated the cospectrum between FPMA and FPMB. We found that for both observations, only CHU combination CHU12 contained continuous good time intervals of length greater than 1024 s, and therefore this was the only CHU combination for which we calculated cospectra. For each observation we then averaged all of the cospectra. Finally, we applied deadtime and background corrections by multiplying the averaged fractional rms normalized power by $(1 - \tau(\overline{S+B}))^{-2}(\overline{S+B}/\overline{S})^2$, where $\tau = 25$ ms is the deadtime per event, S and B are the source and background rates, respectively, calculated from the event list, and bars indicate the geometric mean of the FPMA and FPMB count rates.

Table 5.3 shows the timing properties of the source during both observations. Because the source landed on the gap between detectors during NuObs 1, which is sure to exacerbate any systematic variability due to motion of the source on the focal plane, we do not present the cospectrum here. The quality of the data was not sufficient to perform modeling of the cospectrum, but we did not observe a clear flattening in the low frequency noise of the source. We were able to place an upper limit on the low-frequency noise of rms $< 8\%$ by integrating the measured power

⁵Recent improvements to the calibration of NuSTAR have greatly improved its timing capabilities, allowing for precision down to the $\sim 65 \mu\text{s}$ level (Matteo Bachetti, Markwardt, et al., 2021)

in the range $10^{-3} - 10^{-1}$ Hz. In order to estimate the continuum rms variability, we produced an averaged cospectrum with segment length 64 s (due to the shorter segment length, we were able to utilize the data from all CHU combinations except for CHU2) and sampled the resulting error distributions for the power in the range 0.1 – 10 Hz. We produced 10^5 sample cospectra in this range, and calculated the total rms for each. The result was an upper limit, defined as the 99th percentile of this sample, of rms $< 15\%$.

The source did not fall on the chip gap during NuObs 2, and we therefore present the averaged, logarithmically rebinned cospectrum in Figure 5.7. Although there is clear red noise, similar to the previous observation we do not observe a low frequency turnover. We fitted the low-frequency (< 0.1 Hz) noise to a power law and found an index of $\gamma = -2.1 \pm 0.1$. This is consistent with the tail of a zero-centered Lorentzian, which is often used to describe the low-frequency noise in accreting black holes and neutron stars (T. Belloni, Psaltis, and Michiel van der Klis, 2002). We integrated the low-frequency noise and obtained rms = $12 \pm 2\%$, and we obtained an upper limit on the power integrated between 0.1 – 10 Hz of rms $< 14\%$ using the same method as described for the previous observation (in this case only CHU13 was excluded).

Noting a potential feature in the cospectrum at $\sim 2 \times 10^{-2}$ Hz, we performed a search for quasiperiodic oscillations (QPO) by stepping logarithmically from 10^{-3} Hz to 1024 Hz and fitting the unbinned hard state cospectrum to the power law described above plus a Lorentzian centered at each frequency step. For each frequency, we recorded the change in the χ^2 fit statistic compared to the power law alone. Using this method, we did not find any significant QPO candidates. To determine whether the potential feature could be due to coherent pulsations, we also folded the events for each observation, summing all CHU combinations, at 10000 pulse frequencies between 2×10^{-2} Hz and 3×10^{-2} Hz and calculating the Z_1^2 statistic (Buccheri et al., 1983) for each candidate frequency. For the soft state observation, NuObs 1, we found a peak in the Z_1^2 distribution at ~ 44 s with a significance of 2.1σ , and for the hard state observation, NuObs 2, the highest peak was at ~ 42 s and had a significance of only 0.7σ . We further searched for pulsations in each observation by producing cospectra for the frequency range 0.008–2048 Hz, again using the sum of all CHU combinations. We did not observe any significant peaks during either observation.

5.4 Discussion

The nature of the accretor

While there is no “smoking gun” evidence for one particular type of compact object (for example, the detection of pulsations would prove the presence of a neutron star), the evidence we have presented thus far favors the case of a black hole X-ray binary.

The soft state spectrum is described well by a Comptonized multi-temperature disk blackbody with relativistic reflection features, which may represent returning radiation (c.f. Connors, J. A. García, Thomas Dauser, et al., 2020; Connors, J. A. García, J. Tomsick, et al., 2021; Lazar et al., 2021), and the hard state spectrum is described by a reflected power law alone. Joint modeling using `relxilllp` and `relxillNS` indicates that the accreting object has a high spin, $a \approx 0.97$. Given the relation $a = cJ/GM^2$, where J is the angular momentum of the spinning compact object, and M is its mass, and assuming a moment of inertia $I = \frac{2}{5}MR^2$ for a neutron star, we may estimate the maximum spin that a neutron star can attain. Assuming a canonical neutron star with $M = 1.4M_\odot$ and $R = 10$ km, we arrive at a spin of $a \approx 0.4 \frac{v_{\text{spin}}}{\text{kHz}}$, meaning that even the most rapidly rotating neutron stars will not achieve spin parameters approaching that which we have measured. We consider this a compelling piece of evidence which favors the classification of MAXI J1848–015 as an accreting black hole — explaining the broad Fe line in the case of an accreting neutron star would prove difficult.

Additionally, using archival Chandra observations of the GC01 cluster, Hare, Yang, et al. (2021) were able to place an upper limit of $\sim 3.3 \times 10^{30} \text{ erg s}^{-1}$ on the quiescent luminosity in the 0.5–10 keV band. Whereas accreting neutron stars tend to have quiescent luminosities around $10^{33} \text{ erg s}^{-1}$ (Sergey S. Tsygankov et al., 2017), the luminosity of MAXI J1848–015 prior to outburst is more in line with those measured for black holes, perhaps due to the presence of an event horizon rather than a boundary layer (Garcia et al., 2001).

The initial outburst observed by MAXI was very short-lived compared to many black hole X-ray binaries, which tend to show exponential decays with e-folding times of tens of days (McClintock and Remillard, 2006), however similarly rapid outbursts are not unheard of (c.f. Maitra and Bailyn, 2006). Of course, the count rate in the limited energy band does not always reflect the mass accretion rate, especially in cases where the source spectrum changes significantly. It is, however, interesting to note that some objects, e.g. gamma-ray bursts, exhibit power law decays similar to the flux decrease observed for MAXI J1848–015 by NuSTAR, MAXI, and Swift

(Miller, Sanna, et al., 2021).

Disk accretion at low apparent luminosity

MAXI J1848–015 reached an unabsorbed bolometric luminosity of $\sim 10^{36}$ erg s $^{-1}$ during the soft state, and dropped to a luminosity of $\sim 4 \times 10^{35}$ erg s $^{-1}$ in the hard state. The general shape of the spectrum observed during each of these states is consistent with accretion onto a neutron star or a black hole, and despite the low luminosities, observations of broad emission features around 6.4 keV indicate the presence of an optically thick accretion disk which extends close to the central accretor and reaches a high temperature of ~ 1.4 keV. Models of accretion onto black holes predict the formation of an advection-dominated accretion flow, or ADAF, at mass accretion rates below a few percent of the Eddington limit, resulting in truncation of the disk at large radii (Esin, McClintock, and Narayan, 1997). Indeed, observations have demonstrated that X-ray binaries tend to undergo state transitions at $\sim 2\%$ of the Eddington limit (Maccarone, 2003; Vahdat Motlagh, Kalemci, and Maccarone, 2019). Given the inconsistency we observe between the low source luminosity and evidence for a small disk radius, we consider two effects which could suppress the observed luminosity: disk inclination and obscuration.

Reflection features — the broad Fe line profile and excess “Compton hump” above 10 keV — allowed us to constrain the inclination of the inner regions of the disk as well as the inner disk radius. Reflection modeling of the soft state spectrum resulted in an inner disk radius of $R_{\text{in}} = 2.9 \pm 0.2 R_{\text{g}}$. Even for a neutron star accretor with mass $M = 1.4 M_{\odot}$, this implies an inner disk radius of about 6 km, whereas the flux of the disk blackbody implies an effective inner disk radius of $R_{\text{in}} \sqrt{\cos i} = 0.8$ km, assuming a distance to the source of 3.3 kpc. Several effects, including gravitational redshift, Compton scattering of disk photons (Kubota and Makishima, 2004), spectral hardening (Shimura and Takahara, 1995), and boundary condition corrections (Kubota, Yasuo Tanaka, et al., 1998), will increase or decrease the actual value of the inner disk radius compared to the apparent radius, but in total these effects are unlikely to introduce a factor of more than order unity.

Thus we are left with a contradiction between inner disk radius measurements which could presumably be resolved by assuming a high inclination, i , of the inner disk, resulting in a smaller projected disk flux from the point of view of an observer. While reflection modeling appears to rule this out, preferring an inclination between 20 and 30 degrees, it has been shown that the inclination inferred from reflection

modeling can conflict drastically from the actual inclination of a system, possibly due to obscuration of the blue wing of the broad Fe line (Connors, J. A. García, Steiner, et al., 2019).

High inclination of the inner disk alone may not be able to explain the low flux of MAXI J1848–015. We therefore also consider obscuration of the inner regions of the disk by the outer disk. In this scenario, the outer regions of the disk intercept the line of sight between the observer and the inner disk. If the outer regions of the disk have a clumpy structure, this will result in an effective partial coverer, and may be consistent with the change in column density we have measured between the soft and hard states. Alternatively, we may be observing emission from the inner disk which has been scattered off the outer regions of the disk on the side opposite the observer.

A combination of these two effects has been proposed for the high mass X-ray binary, V4641 Sgr (Koljonen and J. A. Tomsick, 2020), which has similarly been shown to exhibit evidence for a disk extending close to the central black hole despite a low Eddington ratio (Miller, Fabian, et al., 2002). In fact, the hard state of MAXI J1848–015 shares a number of similar characteristics with V4641 Sgr. Both exhibit power law spectra with indices between 1 and 2 and relatively low cutoff energies (< 30 keV). Additionally, both systems undergo short outbursts with durations of tens of days or less (Rudy Wijnands and Michiel van der Klis, 2000; Revnivtsev, Gilfanov, et al., 2002), and on shorter timescales they both exhibit relatively featureless power spectra with red noise components described by a power law of slope ~ -2 (Maitra and Bailyn, 2006). However, the amplitude of variability in the 0.1–10 Hz range that we have observed, while poorly constrained, is somewhat lower than that of V4641 Sgr (Maitra and Bailyn, 2006). In both of these systems, reprocessing of emission from the central regions of the accretor could help to explain this behavior by “smearing out” variability on short timescales.

Given the low luminosity as well as the very short outburst duration, we also suggest the possibility that the source may reside in a compact binary. A smaller-than-usual disk could lead to short outbursts, and depending upon the orbital period, the mass accretion rate may be low (Deloye and Bildsten, 2003). It is interesting to note that black hole binaries undergoing mass transfer in globular clusters are likely to harbor both low-mass donors and relatively low-mass black holes (Kremer et al., 2018). Because we are unable to detect the orbital period, and due to the fact that a compact binary would imply a small companion, which is contradicted by the potential NIR

counterpart of the system, we consider this case speculative. However, given the rarity of known black holes in compact binaries, it is an interesting possibility nonetheless and one which warrants further observations of the source.

Evolving narrow line emission

We found that the narrow Fe lines observed in the soft and hard state spectra have different centroid energies, evolving from ~ 6.8 keV in the soft state to ~ 6.3 keV in the hard state. This change likely corresponds to a change in the ionization of the emitting region, perhaps originating from the outer regions of the accretion disk, with neutral or lowly-ionized Fe I–XVII responsible for the line in the hard state and highly ionized Fe XXV–XXVI responsible for the line in the soft state (J. García, T. Dauser, C. S. Reynolds, et al., 2013). Indeed, the significantly higher thermal X-ray flux in the Fe $K\alpha$ complex energy range during the soft state would lead to a higher ionization.

Rather than an evolution of the emitting region, it is also possible that narrow emission from neutral Fe was actually present during both states, but that it did not increase drastically in flux during the soft state and was therefore not detectable above the thermal-dominated continuum, which was significantly higher in flux around 6.4 keV as compared with the hard state. Indeed, when MAXI J1848–015 was observed by NICER during a second, less pronounced increase in flux, Miller, Sanna, et al. (2021) not only reported that the spectrum was described well by a blackbody with temperature $kT = 1.0$ keV, indicating that the source had again entered the soft state, but the authors also reported both the detection of a prominent, narrow emission line at 6.7 keV with flux $K = 1.5 \times 10^{-5}$ photon $\text{cm}^{-2} \text{s}^{-1}$, as well as a tentative detection of a weaker line at 6.4 keV.

In order to test whether the lower-energy line could have been present but undetected during the NuSTAR observation of the soft state, we added a second Gaussian component to the soft state in our joint spectral model. We froze the centroid at $\mu = 6.4$ keV and the width at $\sigma = 10^{-5}$ keV. We allowed the flux of this component to vary, then we calculated the 99% confidence upper limit as defined by a change in fit statistic of $\Delta W = 6.63$. The resulting upper limit was $K < 7.7 \times 10^{-5}$ photon $\text{cm}^{-2} \text{s}^{-1}$. In other words, we cannot rule out the possibility that neutral Fe emission was present in the soft state at a similar flux level to that observed in the hard state.

One alternative scenario to that of differing ionization is an ionized outflow. Given

that we do not observe clear absorption features which might indicate disk winds, such an outflow may instead take the form of a jet launched during the short outburst observed by MAXI. In this case, the narrow emission lines may originate from fast-moving, ionized blobs of plasma on opposite sides of the accretor along the jet axis. One would then expect to see a pair of components, one of which represents the blue-shifted jet component moving towards the observer, and the second of which originates from the red-shifted jet component moving away from the observer. Due to relativistic beaming, the blue-shifted component would have a higher observed flux than that of the red-shifted component. Additionally, depending on the orientation of the system one may expect a delay between the appearance of the blue component and that of the red component due to the difference in light-travel time from each of the emitting blobs. Migliari, R. Fender, and Méndez (2002) observed a pair of Fe lines during Chandra observations of SS 433, which they were able to spatially associate with extended jet emission. They determined that the Fe line emitting regions were located at a distance of $> 10^{17}$ cm from the central accretor. For a source with low or moderate inclination, this would result in a light-travel time between the two lobes of 30–40 days.

Indeed, we have shown that the 6.8 keV line had a higher flux than, and was observed prior to, the 6.3 keV line. If the two lines originated from regions with similar ionization states, and the difference in energy is solely due to blue- and red-shifting, then we may calculate the velocity of the narrow line emitting regions:

$$\frac{E_{\text{obs}}}{E_{\text{rest}}} = \frac{1}{\gamma (1 - \beta \cos \theta)} \quad (5.1)$$

where E_{obs} is the energy of the line in the frame of the observer, E_{rest} is the energy of the line in the rest frame of the emitting region, β is the ratio of the velocity of the emitting region to the speed of light, γ is the Lorentz factor, and θ is the angle at which the emitter is moving with respect to the line of sight. If we assume that the velocities of the red and blue components are equal in magnitude, the result is $\beta \cos \theta \approx 0.038$. Given that we have measured a moderate inclination via spectral analysis, we arrive at a deprojected velocity of $\beta \approx 0.043$ and a rest frame energy of $E_{\text{rest}} \approx 6.55$ keV, which corresponds to Fe XXII–XXIII.

Assuming a delay of about a week in the appearance of the red-shifted line, we arrive at a distance of $\sim 10^{16}$ cm between the central accretor and the narrow line emitting regions. This distance is difficult to square with a velocity of $0.04c$ in the case that

the putative jets were launched during the initial outburst of MAXI J1848–015, but as we have shown, the 6.3 keV line may have gone undetected early in the outburst. While the evidence we have presented may be consistent with emission from an outflow, we are unable to meaningfully distinguish this case with the simpler case of different ionization states. The jet model may be probed by future observations of the source by observatories, such as Chandra, with high spatial resolution and high spectral resolution in the Fe $K\alpha$ complex.

5.5 Summary and Conclusions

We have presented MAXI and NuSTAR observations of the low-luminosity transient MAXI J1848–015, residing in the GC01 cluster. The source was observed twice by NuSTAR, which was uniquely able to perform observations of the source in outburst due to low angular separation from the Sun. Spectral and timing analyses of the two NuSTAR observations demonstrated a clear change in states from a high soft state to a low hard state. We presented the following results:

- MAXI observed a short period of brightening with duration ~ 5 days, which then underwent a power law decay for several tens of days.
- In the bright state the source reached a luminosity of only $\sim 10^{36}$ erg cm $^{-2}$ s $^{-1}$, corresponding to an Eddington fraction $< 0.5\%$.
- NuSTAR spectra revealed relativistic disk reflection features. Analysis of these features showed:
 - Reflection of thermal emission in the soft state, representing evidence for returning radiation.
 - An accretor with nearly maximal spin.
 - An increase in the inner radius of the accretion disk, providing evidence for moderate disk truncation in the low hard state.
 - Narrow Fe emission components which may differ in energy due to differences in ionization or due to Doppler shifts in an outflow.
- Timing analysis of NuSTAR data revealed clear red noise in the hard state. We did not find evidence for features such as QPOs or pulsations, and the continuum noise in both states was too low for us to constrain.

Due to the high spin measurement as well as other features such as an anomalously low quiescent luminosity and spectral shapes that resemble those of black hole X-ray binaries, we favor the conclusion that the source is an accreting black hole.

However, the low luminosity of the source is difficult to explain at the same time as evidence for a hot disk which extends very close to the central accretor. We therefore discussed scenarios such as high disk inclination or scattering of emission from the outer disk in order to explain this apparent inconsistency. Further observations of the source during future outbursts — particularly those observations which can provide measurements of the binary inclination — will help to elucidate the nature of this intriguing X-ray binary.

*Chapter 6***PROPERTIES OF REDLEN CZT WITH RESPECT TO X-RAY SPECTROSCOPY****6.1 CZT detectors for X-ray Astronomy**

The detection and characterization of astrophysical X-ray emission is a rapidly maturing field which has made significant contributions to our understanding of a number of astrophysical phenomena. Given that a blackbody whose peak emission lies in the X-ray band corresponds to a temperature of $10^5 - 10^8$ K, X-ray observatories are well-positioned to study some of the most energetic events and extreme conditions in the universe. Phenomena which have been investigated by means of their X-ray emission include supernovae, disk accretion, stellar flares, and tidal disruption events. These often represent opportunities for the study of extreme gravity, magnetic fields, temperatures, and other conditions which cannot be achieved in a physical laboratory on Earth.

A NuSTAR hybrid records an event when a photon interacts with the CZT detector. In order to trigger an event, each pixel contains 16 sampling capacitors on which measured charge is deposited in a loop. When a charge is measured above a certain threshold, then an event is triggered, and 8 more capacitors are allowed to sample the current through the detector. Each event, then, consists of a pulse in current, sampled by the 16 capacitors, and the total charge of an event can be calculated by integrating this pulse. When one pixel triggers an event, it also triggers readout on the 8 pixels surrounding it. This way, the hybrid is able to detect events for which charge is spread out over multiple pixels. If the charge on any of these surrounding pixels is above a given threshold, known as the “software threshold” because it can be tuned at the time of analysis, it is included in the integration of the total electrons liberated in an event. Those pixels below this threshold are not considered when determining the electron signal, and each event is assigned a “grade” based on what combination of pixels were above the software threshold. A detailed description of the operation of the NuSTAR hybrid and the event reconstruction procedure can be found in Chapter 2 of Bhalerao (2012).

The CZT crystals which are in use aboard NuSTAR were manufactured by eV Products (since acquired by Kromek). Because eV Products’ crystals are no longer

available, we must turn to other vendors for hard X-ray detectors. In this paper, we present a study of CZT material provided by Redlen Technologies. We have previously presented work-in-progress updates on this topic (Pike, Harrison, Burnham, W. W. Cook, et al., 2018; Pike, Harrison, Burnham, W. Cook, et al., 2018). Here we present a third Redlen detector which appears to be unaffected by hybridization errors (for a discussion of the errors we encountered during hybridization, see Appendix B). We also attempt to provide a more complete picture with various corrections applied in order to minimize the unique impacts of the hybrid design itself. The detector presented here has dimensions $2\text{ cm} \times 2\text{ cm} \times 3\text{ mm}$, making it 50% thicker than the detectors aboard NuSTAR, but the hybrid design is identical. All experiments presented here were conducted using a custom setup in which we are able to shield the detectors from outside light sources and cool the detectors to temperatures below 0° C using a Temptronic Thermostream device.

In Section 6.2, we present measurements of the leakage current and in Section 6.3 we present the results of flood illumination of the full detector. We include a brief description of the corrections applied to each incoming photon event in Section 6.3, then we move on to present measurements of the pixel-by-pixel gain in Section 6.3 and variations in the spectral resolution across the detector. In Section 6.4 we discuss a more detailed investigation of a small region of the detector in order to better characterize the best-case spectral resolution (Section 6.4), depth-of-interaction effects (Section 6.4), and multiple-pixel spectra (Section 6.4). Finally, we compare these results to those for NuSTAR detectors and discuss future applications of this work in Section 6.5.

6.2 Leakage Current

We measured the leakage current by applying a voltage across the CZT crystal without illuminating the detector. We cooled the detector to 5° C and measured the leakage current for each individual pixel over a range of voltages between 0 V and 600 V. We treated the current measured at 0 V as a constant offset which we subtracted from the values measured at nonzero voltages. Additionally, we measured the leakage current in Charge Pump (CP) mode. When CP mode is activated, electronic noise is decreased substantially thanks to a charge pump circuit which mitigates shot noise. However, in this mode, pixels become saturated by lower levels of leakage current (Miyasaka et al., 2009).

We present a map and the distribution of leakage currents measured in CP mode

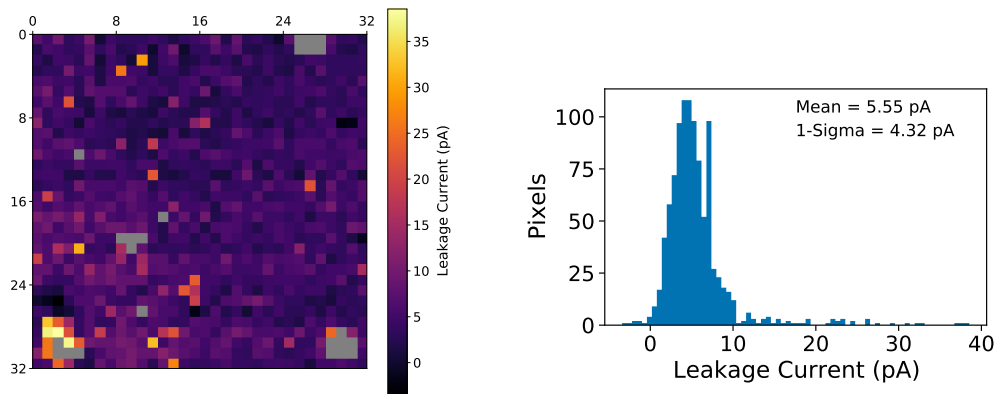


Figure 6.1: Leakage current measured in Charge Pump (CP) mode. Measurements were taken at 5°C with an applied voltage of 500 V. On the left we show the leakage currents for each pixel, and on the right we show the distribution of leakage currents. Outliers, shown in grey, have been omitted for clarity. We find relatively low leakage currents and good uniformity.

at 5°C and an applied voltage of 500 V in Figure 6.1. Outliers¹ are shown in grey, and may be the result of coupling between pixels at the ASIC level, poor bonding between the crystal and the ASIC, or they may be a result of the crystal properties in those regions of the detector. Further investigation is required to determine the root cause of these regions of high leakage current, which also correspond to bursting pixels, as seen later in Figure 6.2. Aside from these small outlier regions, the detector shows good uniformity, with a mean of 5.6 pA and a standard deviation of 4.3 pA. There is a high-current tail apparent in the distribution, which is concentrated in the bottom left corner of the detector. This region corresponds to the location of a wire bond, which may be the cause of the increased leakage current. We estimate that the noise contribution of leakage current in terms of spectral resolution corresponds to $\sim 300\text{ eV}$ FWHM.

6.3 Flood illumination

In order to determine the spectral resolution that can be achieved with Redlen CZT, we irradiated the hybrid with radioactive sources ^{241}Am and ^{155}Eu . However, we first had to perform several corrections in order to properly convert from measured charge to energy. Below, we give a brief overview of these corrections, which are the same corrections applied to the detectors aboard NuSTAR. For a more detailed

¹Here we defined outliers as those pixels with leakage current greater than 20 median deviations from the median leakage current for each mode.

description, see Bhalerao (2012).

Event Corrections

First, we measured the expected contribution of electronic noise by triggering events without applying a voltage across the crystal or illuminating the detector. This resulted in a distribution of events with respect to channels for each pixel. Each event records the number of the sampling capacitor active at the time of triggering, which we will refer to as the “starting capacitor.” The electronic noise distribution differs not only between pixels, but also depends upon the starting capacitor. We measured 16 distributions of electronic noise per pixel, one per starting capacitor, and recorded the mean of each distribution. During flood illumination experiments, we subtracted the mean corresponding to the pixel and starting capacitor of each event triggered by an incoming photon from the raw pulse height of the event.

Given that the capacitors in each pixel sample the current at discrete intervals, the measured pulse height will differ slightly from the underlying physical pulse height depending upon the time at which the event actually occurred. We applied a small “time-of-rise” correction to each event, which was calculated using the charge samples banked before and after the event was triggered. While the precise time-of-rise correction may be slightly different for each pixel, for the purposes of this analysis we used the same coefficient for all pixels.

Following the time-of-rise corrections, we applied a common mode noise correction using non-triggered pixels surrounding the triggered pixel. In addition to addressing common mode noise, this step also helps to correct for the effects of the positively charged hole cloud on the signal. When a photon interacts with the CZT detector, both a negatively charged electron cloud and a positively charged hole cloud are produced. The hole cloud drifts at a much slower rate than that of the electron cloud and induces an image charge on the anode. This image charge must be subtracted from the measured charge in order to reconstruct the charge of the electron cloud. We estimated the contribution of the hole signal per pixel as well as the common mode noise by calculating the mean charge measured on non-triggered pixels.

Pixel-by-pixel gain

Having arrived at a calibrated pulse height, we then moved on to measuring the gain across the entire detector. We did this by irradiating the detector with an ^{241}Am source. We cooled the setup to 5°C and applied a high voltage of 500 V across the detector. ^{241}Am exhibits a strong decay emission line at 59.54 keV, which we

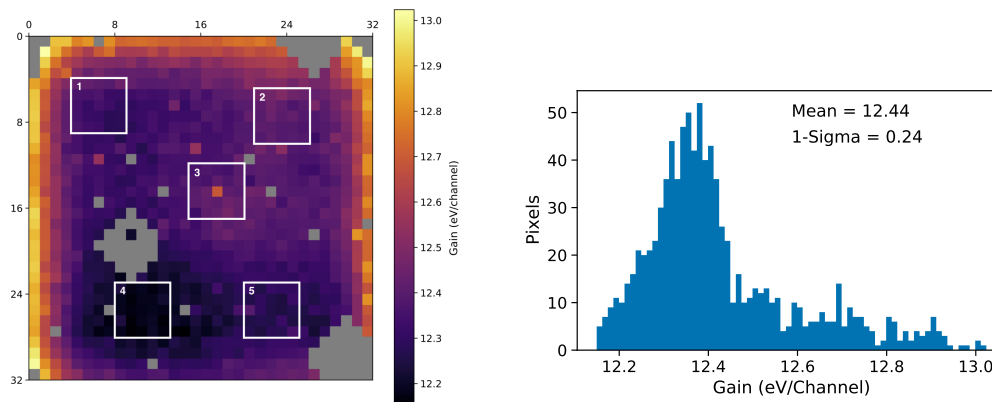


Figure 6.2: The channel-to-energy gain calculated for each activated pixel. We illuminated the full detector with an ^{241}Am source and determined the conversion from channel to energy by fitting the 59.54 keV line to a simple Gaussian. Left: Map of gain calculated for each pixel. Pixels deactivated due to bursting behavior are shown in grey. The five regions for which we produced spectra are enclosed in white squares. Right: Distribution of gain values across the detector. We find good uniformity aside from higher gain measured near the edges due to the guard ring.

used to perform a simple scaling from pulse height to energy. For each pixel, we accumulated a distribution of counts with respect to pulse height. We then fitted the line corresponding to 59.54 keV with a Gaussian function. We recorded the gain as the quotient of 59.54 keV over the centroid of the Gaussian. The resulting gain for each pixel, in units of eV/channel, are shown in Figure 6.2.

We note that during flood illumination with ^{241}Am , we turned off a number of pixels due to high rates of spurious counts, which we attribute mainly to the electronics rather than the Redlen material. We observed a phenomenon wherein turning off one bursting pixel resulted in some adjacent pixels beginning to show bursting behavior. Due to this, we inferred that the bursting was likely related to coupling of adjacent pixel electronics. The regions which we turned off are shown in grey in Figure 6.2.

Aside from the regions which were turned off, we find that the gain is relatively homogeneous across the detector with a mean value of 12.4 eV/channel, and a standard deviation of only 0.24 eV/channel. There is visible structure to the gain distribution however, with lower values clustered in the bottom left corner of the detector, and high values around the edges. The latter is most likely due to the effects of the guard ring which applies a transverse electric field to guide charge away from the edges. The former, however, is probably a result of the CZT itself,

Table 6.1: Spectral resolution measured for different regions in the detector.

Region	FWHM at 14 keV (eV)	FWHM at 60 keV (eV)
1	451 ± 6	610 ± 4
2	444 ± 6	584 ± 4
3	465 ± 7	633 ± 5
4	514 ± 7	650 ± 4
5	475 ± 6	651 ± 5
Mean ± 1σ	470 ± 30	630 ± 30

with slightly different crystal properties resulting in a somewhat smaller band gap — i.e. more electron-hole pairs are produced per energy of an incident photon — or different efficiencies in charge collection due to charge trapping.

Uniformity of Resolution

With the gain calculated, we were able to construct energy spectra. In order to probe how the spectral resolution may vary with Redlen crystal properties, we chose 5 distinct regions on the detector from which to extract spectra, making sure not to include regions in which pixels were bursting or deactivated. These regions are indicated using white boxes in Figure 6.2. For each 5×5 region, we made a spectrum using only single-pixel events, and applied the corrections described above, including the pixel-by-pixel gain correction. We binned the spectrum into bins of width 12 eV. We then measured the full-width at half-maxima (FWHM) of two spectral lines, one at 14 keV and the other at 60 keV, for each spectrum. We measured the FWHM by fitting each of the two spectral lines, but due to effects such as charge sharing, the lines do not appear as simple Gaussians, instead showing low-energy tails. Following the method of Bale (2001), we modeled each line as a combination of a normal distribution, an exponential tail, a low-energy shelf, and a constant offset. The total model, $f(E)$, where E is photon energy, may be written as

$$f(E) = Ae^{-\frac{1}{2}\left(\frac{E-E_0}{\sigma}\right)^2} + \left(Be^{\Gamma(E-E_0)} + C\right) \left[1 - \operatorname{erf}\left(\frac{E-E_0}{\sigma\sqrt{2}}\right)\right] + D \quad (6.1)$$

where A , B , C , and D are the normalization factors of the normal distribution, exponential tail, low-energy shelf, and constant offset, respectively, E_0 is the line centroid, σ is the standard deviation of the normal distribution, and Γ is the slope of the exponential tail. We note that we also activate a pulsar pixel at position (10,10)

which injected a synthetic signal at an energy corresponding to around 92 keV. We found that this signal had a FWHM of 350 eV. This number corresponds to the spectral resolution of the readout electronics themselves.

We list the resulting spectral resolution measurements in Table 6.1. We find that there is some variability in the resolution across the detector, with the FWHM varying by about 70 eV at both 14 keV and 60 keV, and a standard deviation in the FWHM values of about 25 eV for both lines. Further investigation beyond the scope of this paper is required to determine the exact causes for this variability and the variability in the gain across the detector.

6.4 Investigating a small region of the detector

In order to characterize the best-case spectral resolution achievable with the Redlen material using more complete calibration, as well as to probe effects due to depth of photon interaction and multiple-pixel events in more detail, we investigated a small region of the detector away from regions of bursting pixels and high leakage current. We irradiated the detector with ^{241}Am and ^{155}Eu while only activating a 5×5 region bounded on the upper left corner by pixel (14,12) and on the lower right corner by pixel (18,16), corresponding to region 3 shown in Figure 6.2. We performed this experiment at a temperature of 5°C and a high voltage of 500 V. We then accumulated a total of 1.6 million counts with ^{241}Am and 2.3 million counts with ^{155}Eu . For each event, we applied the corrections described in Section 6.3. We recalculated the gain, this time using both the 60 keV line emitted by ^{241}Am and the 86 keV line emitted by ^{155}Eu . We calculated the resulting gain for each pixel using a simple linear regression model where the gain, m , is given by

$$m = \frac{\sum_i x_i y_i}{\sum_i x_i^2} \quad (6.2)$$

where for each source i , x_i represents the centroid of the measured Gaussian in units of channels and y_i represents the known energy of the line (i.e. $y_1 = 59.54\text{ keV}$ and $y_2 = 86.55\text{ keV}$).

Spectral resolution

Having calculated the energy of each incoming photon, we were able to construct a spectrum using only single-pixel events. We excluded all events which occurred within the 16 pixels on the edges of the 5×5 pixel region as it is not possible to reliably determine whether those events were actually single-pixel or not due to the

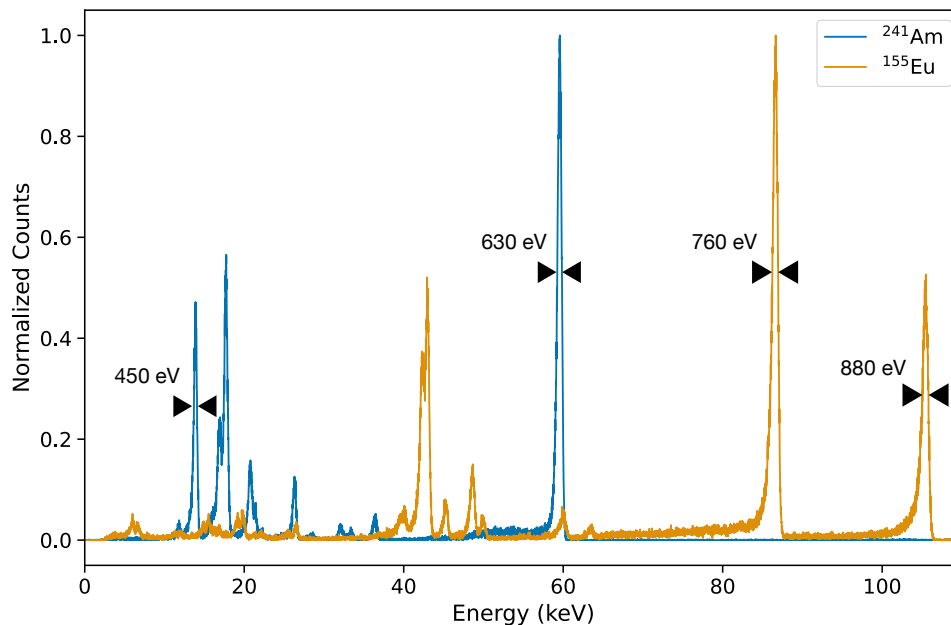


Figure 6.3: Spectra measured for a ^{241}Am source (blue) and a ^{155}Eu source (orange) using a 5×5 pixel region using only single-pixel events. Several corrections, described in Section 6.3 have been applied. The FWHM of each singlet emission line is labeled with black arrows.

fact that some adjacent pixels were not activated. We summed the 9 spectra resulting from the 3×3 pixel region to produce the spectra shown in Figure 6.3, where the spectrum of ^{241}Am is shown in blue and ^{155}Eu is shown in orange. In order to characterize the spectral resolution throughout the X-ray band, we fitted four of the most prominent singlet emission lines using the model described by Equation 6.1 and measured the FWHM for each line.

We chose to fit the ^{241}Am source emission lines at 13.95 keV² and 59.54 keV and the ^{155}Eu lines at 86.55 keV and 105.31 keV. For each line we chose an energy range in which the effects of other emission features were not visible, and we fitted the data in that range to the function above, allowing all 7 parameters to be free. The exceptions to this are the cases of the 60 keV and 105 keV lines, for which a constant offset was not necessary due to the absence of strong emission lines at higher energies. For these lines, we therefore fixed the constant offset at $D = 0$.

In Figure 6.4, we show the fits to each line, as well as the centroid and the FWHM

²The line at 13.95 keV is actually due to Lyman- α emission of ^{237}Np , the decay product of ^{241}Am .

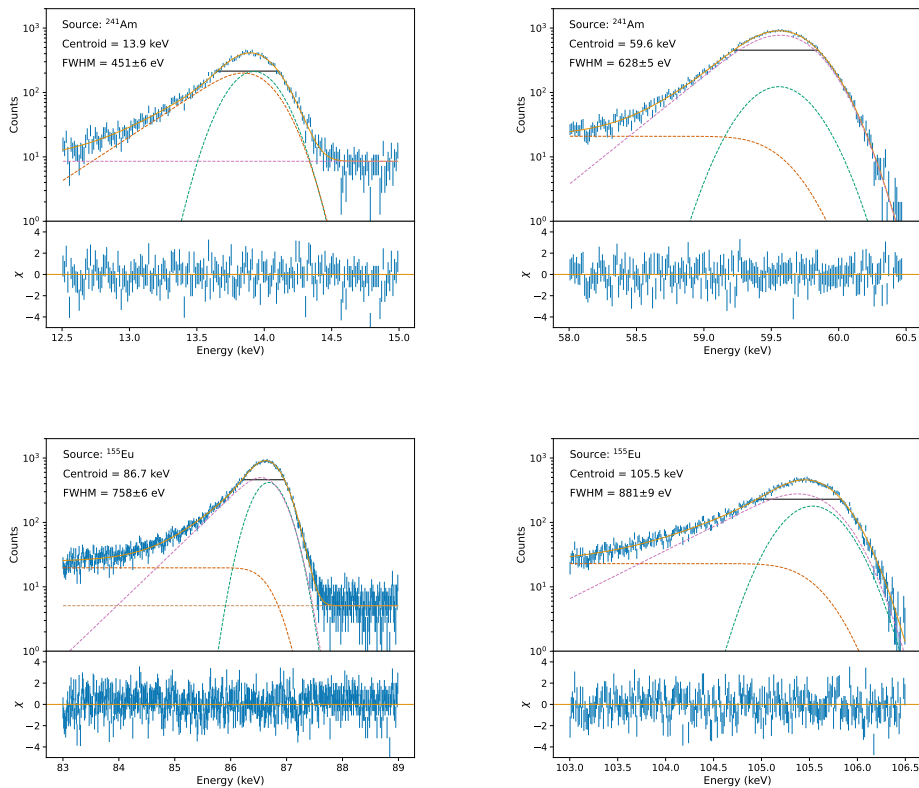


Figure 6.4: Fits to singlet emission lines in the spectra shown in Figure 6.3, transformed into logarithmic scale for legibility. Each line was fitted to the sum of a normal distribution, an exponential power law tail, a low-energy shelf, and a constant offset. These components are plotted as dashed lines while the full model is shown by the solid orange line. For each line, we also show the residuals to the model in the lower panels. The centroid of each line was determined via least-squares fitting to the model, and the FWHM (shown in black) was calculated from the resulting model. We achieve good resolution across the hard X-ray band, with particularly good performance at higher energies.

calculated from those fits. We calculated the centroid by performing a Levenberg-Marquardt least squares fit using Astropy (Astropy Collaboration, T. P. Robitaille, et al., 2013; Astropy Collaboration, Price-Whelan, Sipőcz, Günther, Lim, Crawford, Conseil, Shupe, Craig, Dencheva, Ginsburg, VanderPlas, et al., 2018a). We used the resulting fits to produce a spline from which we subtracted half of the maximum value and the constant offset, D , and we calculated the roots of this spline to determine the FWHM of each line. We calculated the $1-\sigma$ error for each FWHM by simulating 1000 spectra using the error distributions of the measured spectrum

resulting in a distribution of 1000 simulated FWHM values. The typical error in the FWHM measurements is around 6 eV, or half of the binning resolution. We achieved very good spectral resolution across the band which we investigated, ranging from 450 eV at 14 keV to 880 eV at 105 keV.

Depth of Interaction

The depth at which a photon interacts within the detector affects the efficiency with which the electron signal can be collected and the effectiveness with which we are able to account for the hole signal. As photons interact closer to the anode of the detector, charge collection is less efficient, leading to systematic underestimation of the photon energy. The more energetic an incoming photon, the deeper it is likely to penetrate the detector, meaning that higher energy spectral lines exhibit a telltale low-energy tail due to depth-of-interaction effects.

Figure 6.5 starkly demonstrates this effect. The top panels show the ^{241}Am and ^{155}Eu spectra gathered during the experiments described in Section 6.4 (multiple-pixel and edge-pixel events were excluded). The bottom panels show “depth plots:” 2-dimensional histograms of the measured events where events are binned by positively-charged hole signal along the y-axis and central pixel energy, or the negatively-charged electron signal, along the x-axis (note that the spectra in the top panels are projections of the depth plots onto the x-axis). Similarly to the common mode correction described in Section 6.3, we estimated the hole signal by taking the mean value of the charge on the 8 pixels surrounding the triggered pixel. The majority of events occur close to the cathode of the detector, resulting in a very weak hole signal, near $y=0$. However, at higher energies, tracks become apparent in the depth plot. Following these tracks from $y=0$ as they swoop downward and to the left, then back upwards, traces out a path of increasing interaction depth.

These paths are most visible for the two highest-energy spectral lines of $^{155}\text{Eu}^3$, but can even be made out for lines down to around 60 keV. Excluding events from lower regions of the depth plot will sharpen the spectral lines at higher energies. In order to demonstrate this, we chose to exclude events with a hole signal to central pixel energy ratio less than -0.01, shown by the red lines in the bottom panel of Figure 6.5. As expected, performing this depth cut noticeably reduced the low-energy tail effects for the high-energy lines and also made these lines somewhat narrower compared

³The line at 86 keV also shows additional low-energy tailing that can be attributed to down-scattering within the source itself. Thus, this tail is visible even for events with very small hole signals.

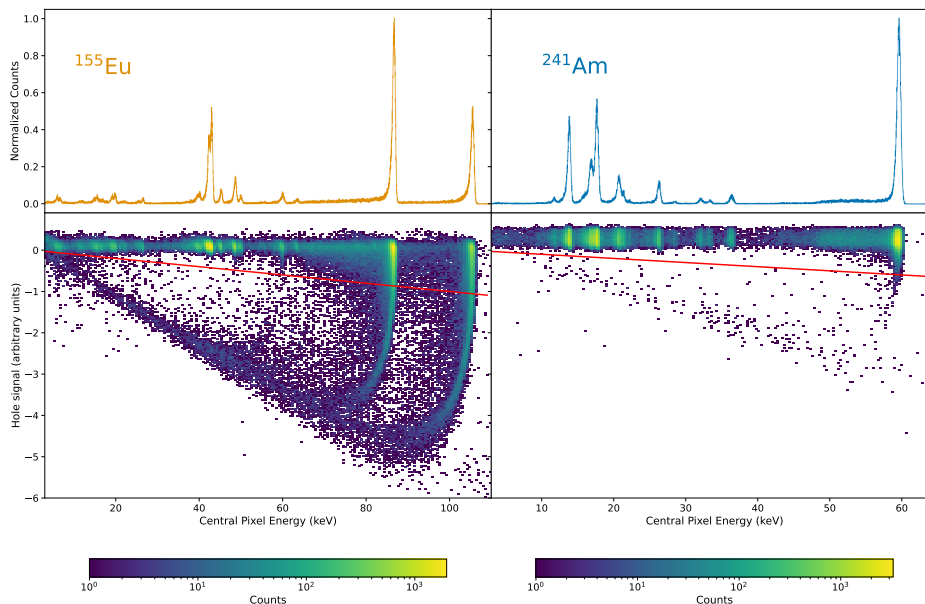


Figure 6.5: Spectra (top) and depth plots (bottom) measured for a ^{241}Am source (right) and a ^{155}Eu source (left) using a 5×5 pixel region using only single-pixel events. Several corrections, described in Section 6.3, have been applied to determine the energy of each event. The bottom panels show the distribution of the negative hole signal observed in pixels surrounding the central pixel in which the electron signal is observed. This acts as a proxy for the depth of interaction of an event, where events which lie near 0 on the y axis occurred near the top of the detector, with depth of interaction increasing as one follows the tracks downwards and to the left. By excluding events beyond a certain depth (shown by the red line with slope -0.01 hole signal/keV), energy resolution can be improved, especially at higher energies.

to the same lines without the depth cut (those shown in Figure 6.4), with a decrease in the FWHM of 3% at 86 keV and 7% at 105 keV. This depth cut results in a 20% reduction in the number of photons in the full spectrum. The efficiency reduction at 86 keV is 13% and at 105 keV the efficiency is reduced by 21%. At 60 keV the efficiency is not significantly reduced, with only 0.2% of photons removed by the depth cut.

Multiple Pixel Events

The depth of interaction will also affect the extent to which the electron cloud is spread across multiple pixels, as a charge cloud originating near the top of the detector will have more time to diffuse horizontally as it drifts vertically toward the anode. We demonstrate this effect in Figure 6.6, which shows the fraction of

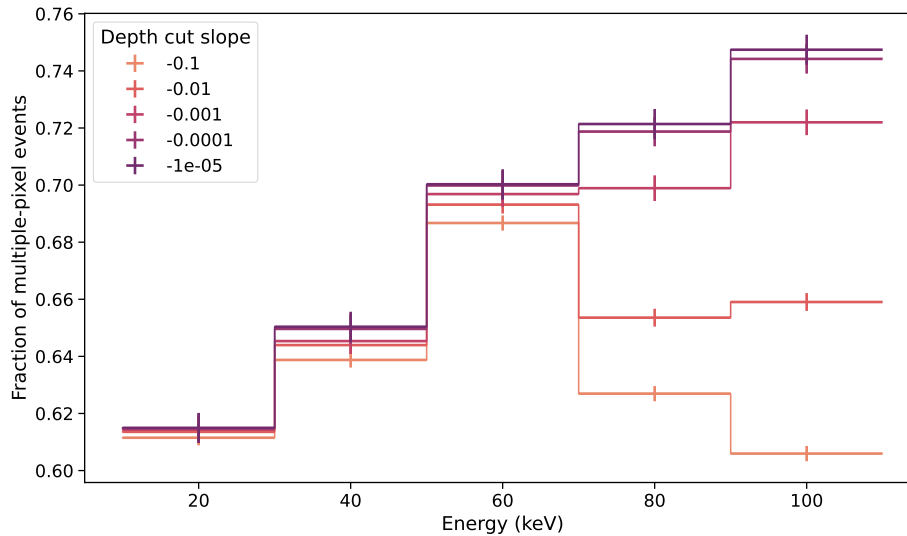


Figure 6.6: The fraction of total events which triggered more than one pixel, as a function of measured energy. Each line represents the multiple-pixel event fraction for a different depth cut slope (see Figure 6.5) between -10^{-5} and -0.1 . The shallower the slope, the more aggressive the depth cut. For a slope of -10^{-5} , all events included occurred near the top, or cathode, of the detector.

events which triggered multiple pixels as a function of energy for different values of depth cut slope. For the most aggressive depth cut, with a slope of -10^{-5} , we exclude all events except those which occurred very near the cathode of the detector. For this depth cut, then, the increase in multiple-pixel event fraction with energy can be solely attributed to the increase in the size of the charge cloud created by each incoming photon. By assuming that the charge cloud has a gaussian profile in the horizontal plane, and that any event which occurs within a certain radius of a pixel's centroid will only trigger that pixel and not its neighbors, we may relate the fraction of multiple-pixel events to the size of the charge cloud. We thus find a charge cloud FWHM of 100-120 μm for the 20-100 keV energy range. We note that this corresponds to the size of the charge cloud at the point of measurement (after the cloud has drifted downwards toward the anode) and not at the time of interaction itself. However, given that the majority of all events occur closer to the cathode (see Figure 6.5), this number is particularly relevant to understanding the tradeoffs inherent in tuning the pixel size for CZT detectors, as small pixels will decrease electronic noise while also increasing the number of multiple-pixel events.

Regardless of the depth cut, we find that at least 60% of events triggered multiple

pixels in the energy range we investigated. This highlights the drawbacks of measuring spectra only using single-pixel events, and demonstrates the need for robust calibrations in order to incorporate multiple-pixel events without degrading spectral resolution. In Figure 6.7 we show a spectrum using both single-pixel events and events for which two adjacent pixels were triggered. We performed a second-order gain correction in order to correct for gain differences between single-pixel and two-pixel events. For each two-pixel event, we first determined the energy deposited in each of the two triggered pixels using the single-pixel gain coefficients calculated using equation 6.2 and summed these two energies to get the first-order energy measurement, E_1 . For each combination of two pixels, we then produced a spectrum from the distribution of E_1 values. By fitting the prominent singlets, we determined a second gain coefficient to map E_1 to the “true” event energy. This correction amounted to a change of only 1 – 3%.

We find that including two-pixel events significantly degrades the spectral resolution with the FWHM of the emission lines varying between 564 eV at 14 keV and 1155 eV at 105 keV. However, we note that the second-order gain correction described above was limited in its precision by a lack of events. With a longer exposure, the second-order gain coefficient may be determined with less scatter, resulting in a sharper spectrum. This improved calibration will be important for applications with smaller pixels than those presented here.

6.5 Summary and Conclusions

We have presented an in-depth analysis of a pixelated CZT detector in order to characterize the material available from Redlen Technologies. We performed several experiments, including measurements of leakage current, gain corrections, and spectral resolution. We primarily aimed to determine two things: how the detector properties vary across the crystal, and what spectral resolution is achievable with this material.

We found that, with the exception of a few regions of bursting pixels, most likely due to the readout electronics rather than the CZT itself, the crystal shows very good uniformity in terms of leakage current, gain, and spectral resolution. However, some variability is apparent across the detector, with a slight gradient going from the top right to the bottom left of the detector in all three of these measured properties. Thanks to the pixelated design of the detector we have presented, these variations can be accounted for in pixel-by-pixel calibrations.

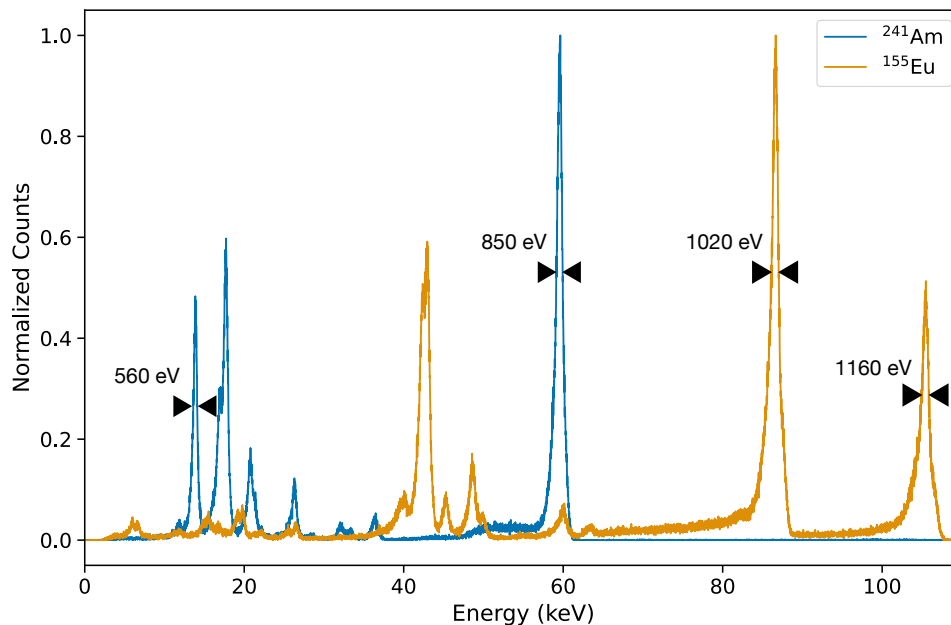


Figure 6.7: Spectra measured for a ^{241}Am source (blue) and a ^{155}Eu source (orange) using a 5×5 pixel region using single-pixel events as well as events for which two adjacent pixels were triggered. Several corrections, described in Section 6.3 and Section 6.4 have been applied. The FWHM of each singlet emission line is labeled with black arrows.

In order to characterize the spectral resolution that can be achieved with more in-depth calibrations, and without having to account for significant variations in crystal properties, we illuminated the detector with both a ^{241}Am source and a ^{155}Eu source while deactivating all but a 5×5 region of pixels on the detector. In this way, we were able to gather sufficient photons to perform precise gain calibrations, depth-of-interaction measurements, and measurements of multi-pixel event fractions in a relatively short exposure.

Using only single-pixel events, we found that the detector produced spectacular resolution across the 14-105 keV energy band. Even at 105 keV, the FWHM achieved was less than 8% of the line energy. In comparison with similar detectors aboard NuSTAR, we achieve an improvement in spectral resolution by about 30%. Further calibrations such as charge sharing and charge loss corrections will only make this improvement more dramatic. It is important to note that the increased thickness of the Redlen CZT compared to the eV Products CZT aboard NuSTAR (3 mm vs. 2 mm), is likely one reason for this improvement, as increasing the thickness at the same pixel pitch will amplify the small-pixel effect. In essence, photons tend to

interact further from the anode of the detector, decreasing the hole signal compared to the electron signal. On the other hand, thicker CZT leads to a smaller fraction of single-pixel events, meaning it's necessary to properly calibrate multiple-pixel events. We constructed a spectrum containing events which triggered two adjacent pixels and found a degradation in resolution of 25-30%, but our second-order gain calibrations were limited by the number of counts at our disposal.

We also estimated the depth of interaction for each event. We were then able to exclude events beyond a certain depth from our spectra, thereby improving the spectral resolution by several percent and significantly reducing the effect of low-energy tailing at high energies. This combination of increased thickness and depth-cut corrections will be especially important for applications such as the proposed X-ray observatory HEX-P (K. K. Madsen, Stern, and HEX-P Team, 2019) which intend to measure photons with energies far in excess of 60 keV.

Taken together, these results provide a very promising view of Redlen CZT for pixelated X-ray detectors which require good detector uniformity and high spectral resolution. While we have only presented one detector in this paper, our preliminary investigations of several other successfully hybridized detectors using Redlen CZT indicate a high yield as well, which we found was a drawback when using eV Products CZT. We hope to present results from more Redlen detectors in the future in order to better understand how much variability Redlen material shows in the properties we investigated in this work.

BIBLIOGRAPHY

- Angelini, L, L Stella, and N E White (1991). “THE DISCOVERY OF AN X-RAY BURST AND A STUDY OF APERIODIC VARIABILITY FROM SMC X-1 L”. In: *ApJ* 371, pp. 332–341.
- Arnaud, K. A. (Jan. 1996). “XSPEC: The First Ten Years”. In: *Astronomical Data Analysis Software and Systems V*. Ed. by George H. Jacoby and Jeannette Barnes. Vol. 101. Astronomical Society of the Pacific Conference Series, p. 17.
- Astropy Collaboration, A. M. Price-Whelan, B. M. Sipőcz, H. M. Günther, P. L. Lim, S. M. Crawford, S. Conseil, D. L. Shupe, M. W. Craig, N. Dencheva, A. Ginsburg, J. T. VanderPlas, et al. (Sept. 2018a). “The Astropy Project: Building an Open-science Project and Status of the v2.0 Core Package”. In: *The Astronomical Journal* 156.3, 123, p. 123. DOI: 10.3847/1538-3881/aabc4f. arXiv: 1801.02634 [astro-ph.IM].
- Astropy Collaboration, A. M. Price-Whelan, B. M. Sipőcz, H. M. Günther, P. L. Lim, S. M. Crawford, S. Conseil, D. L. Shupe, M. W. Craig, N. Dencheva, A. Ginsburg, J. T. VanderPlas, et al. (Sept. 2018b). “The Astropy Project: Building an Open-science Project and Status of the v2.0 Core Package”. In: *AJ* 156.3, 123, p. 123. DOI: 10.3847/1538-3881/aabc4f. arXiv: 1801.02634 [astro-ph.IM].
- Astropy Collaboration, T. P. Robitaille, et al. (Oct. 2013). “Astropy: A community Python package for astronomy”. In: *Astronomy and Astrophysics* 558, A33, A33. DOI: 10.1051/0004-6361/201322068. arXiv: 1307.6212 [astro-ph.IM].
- Astropy Collaboration, Thomas P. Robitaille, et al. (Oct. 2013). “Astropy: A community Python package for astronomy”. In: *A&A* 558, A33, A33. DOI: 10.1051/0004-6361/201322068. arXiv: 1307.6212 [astro-ph.IM].
- Bachetti, M. et al. (Oct. 2014). “An ultraluminous X-ray source powered by an accreting neutron star”. In: *Nature* 514.7521, pp. 202–204. DOI: 10.1038/nature13791. arXiv: 1410.3590 [astro-ph.HE].
- Bachetti, Matteo (2015). *MaLTPyNT: Quick look timing analysis for NuSTAR data*. URL: 2015ascl.soft02021B.
- Bachetti, Matteo, Fiona A. Harrison, et al. (Feb. 2015). “No Time for Dead Time: Timing Analysis of Bright Black Hole Binaries with NuSTAR”. In: *ApJ* 800.2, 109, p. 109. DOI: 10.1088/0004-637X/800/2/109. arXiv: 1409.3248 [astro-ph.HE].
- Bachetti, Matteo, Craig B. Markwardt, et al. (Feb. 2021). “Timing Calibration of the NuSTAR X-Ray Telescope”. In: *ApJ* 908.2, 184, p. 184. DOI: 10.3847/1538-4357/abd1d6. arXiv: 2009.10347 [astro-ph.IM].
- Bale, Greg (Jan. 2001). “CdZnTe radiation detectors for hard X-ray astronomy”. PhD thesis. University of Leicester, UK.

- Barrett, H. H., J. D. Eskin, and H. B. Barber (July 1995). “Charge Transport in Arrays of Semiconductor Gamma-Ray Detectors”. In: *Physics Review Letters* 75.1, pp. 156–159. doi: 10.1103/PhysRevLett.75.156.
- Barrière, Nicolas M. et al. (Feb. 2015). “NuSTAR Observation of a Type I X-Ray Burst from GRS 1741.9-2853”. In: *ApJ* 799.2, 123, p. 123. doi: 10.1088/0004-637X/799/2/123. arXiv: 1411.4745 [astro-ph.HE].
- Barthelmy, Scott D. et al. (Oct. 2005). “The Burst Alert Telescope (BAT) on the SWIFT Midex Mission”. In: *Space Science Reviews* 120.3-4, pp. 143–164. doi: 10.1007/s11214-005-5096-3. arXiv: astro-ph/0507410 [astro-ph].
- Belloni, Tomaso, Dimitrios Psaltis, and Michiel van der Klis (June 2002). “A Unified Description of the Timing Features of Accreting X-Ray Binaries”. In: *ApJ* 572.1, pp. 392–406. doi: 10.1086/340290. arXiv: astro-ph/0202213 [astro-ph].
- Ben Bekhti, N. et al. (2016). “HI4PI: a full-sky H I survey based on EBHIS and GASS”. In: *A&A* 594, A116. ISSN: 0004-6361. doi: 10.1051/0004-6361/201629178. URL: <http://www.aanda.org/10.1051/0004-6361/201629178>.
- Bhalerao, Varun (May 2012). “Neutron Stars and NuSTAR”. PhD thesis. California Institute of Technology.
- Bhattacharyya, Sudip and Tod E. Strohmayer (Jan. 2006). “A Non-PRE Double-peaked Burst from 4U 1636-536: Evidence of Burning Front Propagation”. In: *ApJL* 636.2, pp. L121–L124. doi: 10.1086/500199. arXiv: astro-ph/0509369 [astro-ph].
- Bondi, H. and F. Hoyle (Jan. 1944). “On the mechanism of accretion by stars”. In: *MNRAS* 104, p. 273. doi: 10.1093/mnras/104.5.273.
- Bonnet-Bidaud, J. M. and M. van der Klis (1981). “Long Term X-ray Observations of SMC X-1 Including a Turn-on”. In: *A&A* 97, pp. 134–138.
- Brightman, Murray et al. (Jan. 2019). “A ~60-day super-orbital period originating from the ultraluminous X-ray pulsar in M82”. In: *arXiv e-prints*, arXiv:1901.10491, arXiv:1901.10491. arXiv: 1901.10491 [astro-ph.HE].
- Brumback, Mckinley C et al. (2018). “Discovery of Pulsation Dropout and Turn-on during the High State of the Accreting X-Ray Pulsar LMC X-4”. In: *ApJ* 861, p. L7. doi: 10.3847/2041-8213/aacd13. URL: <https://doi.org/10.3847/2041-8213/aacd13>.
- Buccheri, R. et al. (Dec. 1983). “Search for pulsed γ -ray emission from radio pulsars in the COS-B data.” In: *A&A* 128, pp. 245–251.
- Burrows, David N. et al. (Oct. 2005a). “The Swift X-Ray Telescope”. In: *Space Science Reviews* 120.3-4, pp. 165–195. doi: 10.1007/s11214-005-5097-2. arXiv: astro-ph/0508071 [astro-ph].

- Burrows, David N. et al. (Oct. 2005b). “The Swift X-Ray Telescope”. In: *SSRv* 120.3-4, pp. 165–195. DOI: 10.1007/s11214-005-5097-2. arXiv: astro-ph/0508071 [astro-ph].
- Caballero, I. et al. (Feb. 2013). “A Double-peaked Outburst of A 0535+26 Observed with INTEGRAL, RXTE, and Suzaku”. In: *ApJL* 764.2, L23, p. L23. DOI: 10.1088/2041-8205/764/2/L23. arXiv: 1301.4856 [astro-ph.HE].
- Carpano, S. et al. (2018). “Discovery of pulsations from NGC 300 ULX1 and its fast period evolution”. In: *MNRAS* 476, pp. L45–L49. DOI: 10.1093/mnras1/sly030.
- Cash, W. (Mar. 1979). “Parameter estimation in astronomy through application of the likelihood ratio.” In: *ApJ* 228, pp. 939–947. DOI: 10.1086/156922.
- Chakrabarty, Deepto et al. (Feb. 2021). “Chandra Localization of MAXI J1848-015”. In: *The Astronomer’s Telegram* 14424, p. 1.
- Charles, Phil et al. (May 2008). “Observational properties of accretion discs: Precessing and warped?” In: *New Astronomy Reviews* 51.10-12, pp. 768–774. DOI: 10.1016/j.newar.2008.03.025.
- Church, M. J., A. Gibiec, and M. Bałucińska-Church (Mar. 2014). “The nature of the island and banana states in atoll sources and a unified model for low-mass X-ray binaries”. In: *MNRAS* 438.4, pp. 2784–2797. DOI: 10.1093/mnras/stt2364. arXiv: 1312.1823 [astro-ph.HE].
- Clarkson, W. I. et al. (2003). “Long-term properties of accretion discs in X-ray binaries - I. The variable third period in SMC X-1”. In: *MNRAS* 339.2, pp. 447–454. ISSN: 00358711. DOI: 10.1046/j.1365-8711.2003.06176.x. arXiv: 0210241v1 [astro-ph].
- Coburn, W. et al. (2002). “Magnetic Fields of Accreting X-Ray Pulsars with the Rossi X-Ray Timing Explorer”. In: *ApJ* 580, pp. 394–412. DOI: 10.1086/343033.
- Cocchi, M. et al. (June 1999). “Discovery of type-I X-ray bursts from GRS 1741.9-2853”. In: *A&A* 346, pp. L45–L48. arXiv: astro-ph/9905184 [astro-ph].
- Connors, Riley M. T., Javier A. García, Thomas Dauser, et al. (Mar. 2020). “Evidence for Returning Disk Radiation in the Black Hole X-Ray Binary XTE J1550-564”. In: *ApJ* 892.1, 47, p. 47. DOI: 10.3847/1538-4357/ab7afc. arXiv: 2002.11873 [astro-ph.HE].
- Connors, Riley M. T., Javier A. García, James F. Steiner, et al. (Sept. 2019). “Conflicting Disk Inclination Estimates for the Black Hole X-Ray Binary XTE J1550-564”. In: *ApJ* 882.2, 179, p. 179. DOI: 10.3847/1538-4357/ab35df.
- Connors, Riley M. T., Javier A. García, John Tomsick, et al. (Mar. 2021). “Reflection Modeling of the Black Hole Binary 4U 1630-47: The Disk Density and Returning Radiation”. In: *ApJ* 909.2, 146, p. 146. DOI: 10.3847/1538-4357/abdd2c. arXiv: 2101.06343 [astro-ph.HE].

- Corral-Santana, J. M. et al. (Mar. 2016). “BlackCAT: A catalogue of stellar-mass black holes in X-ray transients”. In: *Astronomy and Astrophysics* 587, A61, A61. DOI: 10.1051/0004-6361/201527130. arXiv: 1510.08869 [astro-ph.HE].
- Dage, Kristen C et al. (Sept. 2018). “Long-term properties of accretion discs in X-ray binaries – III. A search for spin–superorbital correlation in SMC X-1”. In: *Monthly Notices of the Royal Astronomical Society* 482.1, pp. 337–350. ISSN: 0035-8711. DOI: 10.1093/mnras/sty2572. eprint: <http://oup.prod.sis.lan/mnras/article-pdf/482/1/337/26151572/sty2572.pdf>. URL: <https://dx.doi.org/10.1093/mnras/sty2572>.
- Dauser, T. et al. (Oct. 2014). “The role of the reflection fraction in constraining black hole spin.” In: *MNRAS* 444, pp. L100–L104. DOI: 10.1093/mnrasl/slu125. arXiv: 1408.2347 [astro-ph.HE].
- Davidge, T. J. et al. (Dec. 2016). “Cluster Glimpses with RAVEN: AO-corrected Near and Mid-infrared Images of GLIMPSE C01 and GLIMPSE C02”. In: *AJ* 152.6, 173, p. 173. DOI: 10.3847/0004-6256/152/6/173. arXiv: 1610.09484 [astro-ph.GA].
- Davies, Ben et al. (Feb. 2011). “GLIMPSE-CO1: the most massive intermediate-age stellar cluster in the Galaxy”. In: *MNRAS* 411.2, pp. 1386–1394. DOI: 10.1111/j.1365-2966.2010.17777.x. arXiv: 1010.2973 [astro-ph.GA].
- Degenaar, N. et al. (Apr. 2020). “Swift/XRT detects a new outburst of the Galactic Center transient GRS 1741.9-2853”. In: *The Astronomer’s Telegram* 13683, p. 1.
- Deloye, Christopher J. and Lars Bildsten (Dec. 2003). “White Dwarf Donors in Ultracompact Binaries: The Stellar Structure of Finite-Entropy Objects”. In: *ApJ* 598.2, pp. 1217–1228. DOI: 10.1086/379063. arXiv: astro-ph/0308233 [astro-ph].
- Edgar, Richard (Sept. 2004). “A review of Bondi-Hoyle-Lyttleton accretion”. In: *New Astronomy Reviews* 48.10, pp. 843–859. DOI: 10.1016/j.newar.2004.06.001. arXiv: astro-ph/0406166 [astro-ph].
- Esin, Ann A., Jeffrey E. McClintock, and Ramesh Narayan (Nov. 1997). “Advection-Dominated Accretion and the Spectral States of Black Hole X-Ray Binaries: Application to Nova Muscae 1991”. In: *ApJ* 489.2, pp. 865–889. DOI: 10.1086/304829. arXiv: astro-ph/9705237 [astro-ph].
- Falanga, M et al. (2015). “Astrophysics Ephemeris , orbital decay , and masses of ten eclipsing high-mass X-ray binaries”. In: *A&A* 577, A130.
- Fender, R. P., T. M. Belloni, and E. Gallo (Dec. 2004). “Towards a unified model for black hole X-ray binary jets”. In: *MNRAS* 355.4, pp. 1105–1118. DOI: 10.1111/j.1365-2966.2004.08384.x. arXiv: astro-ph/0409360 [astro-ph].

- Fisker, Jacob Lund, Friedrich-Karl Thielemann, and Michael Wiescher (June 2004). “The Nuclear Reaction Waiting Points: ^{22}Mg , ^{26}Si , ^{30}S , and ^{34}Ar and Bolometrically Double-peaked Type I X-Ray Bursts”. In: *ApJL* 608.1, pp. L61–L64. DOI: 10.1086/422215. arXiv: astro-ph/0312361 [astro-ph].
- Foreman-Mackey, Daniel (June 2016). “corner.py: Scatterplot matrices in Python”. In: *The Journal of Open Source Software* 1.2, p. 24. DOI: 10.21105/joss.00024. URL: <https://doi.org/10.21105/joss.00024>.
- Fürst, F, S Suchy, et al. (2011). “Astronomy Astrophysics Study of the many fluorescent lines and the absorption variability in GX 301 –2 with XMM-Newton”. In: *A&A* 535, p. 9. DOI: 10.1051/0004-6361/201117665. URL: <http://www.batse.msfc.nasa.gov/gbm/science/>.
- Fürst, F, D J Walton, et al. (2018). “A tale of two periods: determination of the orbital ephemeris of the super-Eddington pulsar NGC 7793 P13”. In: *A&A* 616, A186. DOI: 10.1051/0004-6361/201833292. URL: https://swift.gsfc.nasa.gov/analysis/UVOT_.
- Fürst, F. et al. (2016). “Discovery of Coherent Pulsations From the Ultraluminous X-Ray Source Ngc 7793 P13”. In: *ApJ* 831.2, p. L14. ISSN: 2041-8213. DOI: 10.3847/2041-8205/831/2/L14. URL: <http://stacks.iop.org/2041-8205/831/i=2/a=L14?key=crossref.b881c45d1142356713ebb95ab977fb05>.
- Galloway, Duncan K. and Laurens Keek (2021). “Thermonuclear X-ray Bursts”. In: *Timing Neutron Stars: Pulsations, Oscillations and Explosions*. Ed. by Tomaso M. Belloni, Mariano Méndez, and Chengmin Zhang. Berlin, Heidelberg: Springer Berlin Heidelberg, pp. 209–262. ISBN: 978-3-662-62110-3. DOI: 10.1007/978-3-662-62110-3_5. URL: https://doi.org/10.1007/978-3-662-62110-3_5.
- Galloway, Duncan K., Michael P. Munro, et al. (Dec. 2008). “Thermonuclear (Type I) X-Ray Bursts Observed by the Rossi X-Ray Timing Explorer”. In: *ApJS* 179.2, pp. 360–422. DOI: 10.1086/592044. arXiv: astro-ph/0608259 [astro-ph].
- Galloway, Duncan K., Dimitrios Psaltis, et al. (June 2003). “Eddington-limited X-Ray Bursts as Distance Indicators. I. Systematic Trends and Spherical Symmetry in Bursts from 4U 1728-34”. In: *ApJ* 590.2, pp. 999–1007. DOI: 10.1086/375049. arXiv: astro-ph/0208464 [astro-ph].
- Garcia, Michael R. et al. (May 2001). “New Evidence for Black Hole Event Horizons from Chandra”. In: *ApJL* 553.1, pp. L47–L50. DOI: 10.1086/320494. arXiv: astro-ph/0012452 [astro-ph].
- García, J., T. Dauser, A. Lohfink, et al. (Feb. 2014). “Improved Reflection Models of Black Hole Accretion Disks: Treating the Angular Distribution of X-Rays”. In: *ApJ* 782.2, 76, p. 76. DOI: 10.1088/0004-637X/782/2/76. arXiv: 1312.3231 [astro-ph.HE].

- García, J., T. Dauser, C. S. Reynolds, et al. (May 2013). “X-Ray Reflected Spectra from Accretion Disk Models. III. A Complete Grid of Ionized Reflection Calculations”. In: *ApJ* 768.2, 146, p. 146. DOI: 10.1088/0004-637X/768/2/146. arXiv: 1303.2112 [astro-ph.HE].
- García, J. and T. R. Kallman (Aug. 2010). “X-ray Reflected Spectra from Accretion Disk Models. I. Constant Density Atmospheres”. In: *ApJ* 718.2, pp. 695–706. DOI: 10.1088/0004-637X/718/2/695. arXiv: 1006.0485 [astro-ph.HE].
- García, Javier A., Thomas Dauser, et al. (Feb. 2022). “Relativistic X-Ray Reflection Models for Accreting Neutron Stars”. In: *ApJ* 926.1, 13, p. 13. DOI: 10.3847/1538-4357/ac3cb7. arXiv: 2111.12838 [astro-ph.HE].
- García, Javier A., John A. Tomsick, et al. (Nov. 2019). “The 2017 Failed Outburst of GX 339-4: Relativistic X-Ray Reflection near the Black Hole Revealed by NuSTAR and Swift Spectroscopy”. In: *ApJ* 885.1, 48, p. 48. DOI: 10.3847/1538-4357/ab384f. arXiv: 1908.00965 [astro-ph.HE].
- Gehrels, N. et al. (Aug. 2004). “The Swift Gamma-Ray Burst Mission”. In: *ApJ* 611.2, pp. 1005–1020. DOI: 10.1086/422091. arXiv: astro-ph/0405233 [astro-ph].
- Gendreau, Keith and Zaven Arzoumanian (Dec. 2017). “Searching for a pulse”. In: *Nature Astronomy* 1, pp. 895–895. DOI: 10.1038/s41550-017-0301-3.
- Goodman, Jonathan and Jonathan Weare (Jan. 2010). “Ensemble samplers with affine invariance”. In: *Communications in Applied Mathematics and Computational Science* 5.1, pp. 65–80. DOI: 10.2140/camcos.2010.5.65.
- Goodwin, A. J., A. Heger, and D. K. Galloway (Jan. 2019). “Neutrino Losses in Type I Thermonuclear X-Ray Bursts: An Improved Nuclear Energy Generation Approximation”. In: *ApJ* 870.2, 64, p. 64. DOI: 10.3847/1538-4357/aaeed2. arXiv: 1808.02225 [astro-ph.HE].
- Hainich, R. et al. (Feb. 2020). “The stellar and wind parameters of six prototypical HMXBs and their evolutionary status”. In: *Astronomy and Astrophysics* 634, A49, A49. DOI: 10.1051/0004-6361/201935498. arXiv: 2001.02420 [astro-ph.SR].
- Hare, Jeremy, Oleg Kargaltsev, and Blagoy Rangelov (Sept. 2018). “Chandra X-Ray Observatory and Hubble Space Telescope Observations of the Intermediate-age Cluster GLIMPSE-C01”. In: *ApJ* 865.1, 33, p. 33. DOI: 10.3847/1538-4357/aad90d. arXiv: 1808.02902 [astro-ph.HE].
- Hare, Jeremy, Hui Yang, et al. (Mar. 2021). “Chandra Observations of MAXI J1848-015 prior to its outburst and a possible NIR counterpart”. In: *The Astronomer’s Telegram* 14499, p. 1.
- Harrison, Fiona A. et al. (June 2013). “The Nuclear Spectroscopic Telescope Array (NuSTAR) High-energy X-Ray Mission”. In: *ApJ* 770.2, 103, p. 103. DOI: 10.1088/0004-637X/770/2/103. arXiv: 1301.7307 [astro-ph.IM].

- He, C. -C. and L. Keek (Mar. 2016). “Anisotropy of X-Ray Bursts from Neutron Stars with Concave Accretion Disks”. In: *ApJ* 819.1, 47, p. 47. DOI: 10.3847/0004-637X/819/1/47. arXiv: 1512.02889 [astro-ph.HE].
- Hickox, R C and S D Vrtilek (2005). “Pulse-Phase Spectroscopy of SMC X-1 with Chandra and XMM-Newton: Reprocessing by a Precessing Disk?” In: *ApJ* 633.2, pp. 1064–1075. ISSN: 0004-637X. DOI: 10.1086/491596.
- Hilditch, R. W., I. D. Howarth, and T. J. Harries (2005). “Forty eclipsing binaries in the Small Magellanic Cloud: Fundamental parameters and Cloud distance”. In: *MNRAS* 357.1, pp. 304–324. ISSN: 00358711. DOI: 10.1111/j.1365-2966.2005.08653.x.
- Hogg, David W. and Daniel Foreman-Mackey (May 2018). “Data Analysis Recipes: Using Markov Chain Monte Carlo”. In: *ApJS* 236.1, 11, p. 11. DOI: 10.3847/1538-4365/aab76e. arXiv: 1710.06068 [astro-ph.IM].
- Hoyle, F. and R. A. Lyttleton (Jan. 1939). “The effect of interstellar matter on climatic variation”. In: *Proceedings of the Cambridge Philosophical Society* 35.3, p. 405. DOI: 10.1017/S0305004100021150.
- Hunter, J. D. (2007). “Matplotlib: A 2D graphics environment”. In: *Computing in Science & Engineering* 9.3, pp. 90–95. DOI: 10.1109/MCSE.2007.55.
- Huppenkothen, D et al. (Aug. 2016). *Stingray: Spectral-timing software*. Astrophysics Source Code Library. URL: 2016ascl.soft08001H.
- Huppenkothen, Daniela, Matteo Bachetti, Abigail L. Stevens, Simone Migliari, and Paul Balm (Aug. 2016). *Stingray: Spectral-timing software*. ascl: 1608.001.
- Huppenkothen, Daniela, Matteo Bachetti, Abigail L. Stevens, Simone Migliari, Paul Balm, et al. (Aug. 2019). “Stingray: A Modern Python Library for Spectral Timing”. In: *ApJ* 881.1, 39, p. 39. DOI: 10.3847/1538-4357/ab258d. arXiv: 1901.07681 [astro-ph.IM].
- Hutchings, J. B. et al. (1977). “The spectroscopic orbit and masses of SK 160/SMC X-1”. In: *ApJ* 217, pp. 186–196.
- Hynes, Robert I. (Oct. 2010). “Multiwavelength Observations of Accretion in Low-Mass X-ray Binary Systems”. In: *arXiv e-prints*, arXiv:1010.5770, arXiv:1010.5770. arXiv: 1010.5770 [astro-ph.HE].
- Illarionov, A F and R A Sunyaev (1975). “Why the Number of Galactic X-ray Stars Is so Small?” In: *A&A* 39, p. 185. ISSN: 1098-6596. DOI: 10.1017/CB09781107415324.004. URL: http://adsabs.harvard.edu/cgi-bin/nph-data_query?bibcode=1975A&A...39..185I&link_type=ABSTRACT%5Cnpapers://ae138101-6c21-4699-bf77-43c1601c1c3a/Paper/p209.
- Inam, S., A. Baykal, and E. Beklen (2010). “Analysis of RXTE-PCA Observations of SMC X-1”. In: *MNRAS* 403.1, pp. 378–386. DOI: 10.1111/j.1365-2966.2009.16121.x.

- Israel, G. L. et al. (2017). “Discovery of a 0.42-s pulsar in the ultraluminous X-ray source NGC 7793 P13”. In: *MNRAS* 466.1, pp. L48–L52. ISSN: 17453933. DOI: 10.1093/mnrasl/slw218.
- Israel, Gian Luca et al. (2017). “An accreting pulsar with extreme properties drives an ultraluminous x-ray source in NGC 5907”. In: *Science* 355.6327, pp. 817–819. ISSN: 10959203. DOI: 10.1126/science.aai8635.
- Jaisawal, Gaurava K. et al. (Sept. 2019). “NICER Observes a Secondary Peak in the Decay of a Thermonuclear Burst from 4U 1608-52”. In: *ApJ* 883.1, 61, p. 61. DOI: 10.3847/1538-4357/ab3a37. arXiv: 1908.03373 [astro-ph.HE].
- Joye, W. A. and E. Mandel (2003a). “New Features of SAOImage DS9”. In: *Astronomical Data Analysis Software and Systems XII*. Ed. by H. E. Payne, R. I. Jedrzejewski, and R. N. Hook. Vol. 295. Astronomical Society of the Pacific Conference Series, p. 489.
- (Jan. 2003b). “New Features of SAOImage DS9”. In: *Astronomical Data Analysis Software and Systems XII*. Ed. by H. E. Payne, R. I. Jedrzejewski, and R. N. Hook. Vol. 295. Astronomical Society of the Pacific Conference Series, p. 489.
- Kaaret, Philip, Hua Feng, and Timothy P. Roberts (2017). “Ultraluminous X-Ray Sources”. In: *Annual Review of Astronomy and Astrophysics* 55.1, pp. 303–341. DOI: 10.1146/annurev-astro-091916-055259. eprint: <https://doi.org/10.1146/annurev-astro-091916-055259>. URL: <https://doi.org/10.1146/annurev-astro-091916-055259>.
- Kaastra, J. S. and J. A. M. Bleeker (Mar. 2016). “Optimal binning of X-ray spectra and response matrix design”. In: *A&A* 587, A151, A151. DOI: 10.1051/0004-6361/201527395. arXiv: 1601.05309 [astro-ph.IM].
- Kalogera, Vassiliki and Gordon Baym (Oct. 1996). “The Maximum Mass of a Neutron Star”. In: *ApJL* 470, p. L61. DOI: 10.1086/310296. arXiv: astro-ph/9608059 [astro-ph].
- Kennea, J. A. et al. (Feb. 2021). “MAXI J1848-015: Swift localization at the core of GLIMPSE-C01”. In: *The Astronomer’s Telegram* 14420, p. 1.
- Kobulnicky, Henry A. et al. (Jan. 2005). “Discovery of a New Low-Latitude Milky Way Globular Cluster Using GLIMPSE”. In: *AJ* 129.1, pp. 239–250. DOI: 10.1086/426337. arXiv: astro-ph/0410400 [astro-ph].
- Koljonen, K. I. I. and J. A. Tomsick (July 2020). “The obscured X-ray binaries V404 Cyg, Cyg X-3, V4641 Sgr, and GRS 1915+105”. In: *A&A* 639, A13, A13. DOI: 10.1051/0004-6361/202037882. arXiv: 2004.08536 [astro-ph.HE].
- Kremer, Kyle et al. (Jan. 2018). “Accreting Black Hole Binaries in Globular Clusters”. In: *ApJ* 852.1, 29, p. 29. DOI: 10.3847/1538-4357/aa99df. arXiv: 1709.05444 [astro-ph.HE].
- Kreykenbohm, I. et al. (2008). “High variability in Vela X-1: giant flares and off states”. In: *A&A* 492, pp. 511–525. DOI: 10.1051/0004-6361:200809956.

- Kubota, Aya and Kazuo Makishima (Jan. 2004). “The Three Spectral Regimes Found in the Stellar Black Hole XTE J1550-564 in Its High/Soft State”. In: *ApJ* 601.1, pp. 428–438. DOI: 10.1086/380433. arXiv: astro-ph/0310085 [astro-ph].
- Kubota, Aya, Yasuo Tanaka, et al. (Dec. 1998). “Evidence for a Black Hole in the X-Ray Transient GRS 1009-45”. In: *PASJ* 50, pp. 667–673. DOI: 10.1093/pasj/50.6.667.
- Kuster, M. et al. (2001). “A Her X-1 Turn-On: Using the pulse profile to probe the outer edge of an accretion disk”. In: *New Visions of the X-ray Universe in the XMM-Newton and Chandra Era*. November, pp. 26–30. URL: <http://arxiv.org/abs/astro-ph/0203213>.
- Kuulkers, E., P. R. den Hartog, et al. (Feb. 2003). “Photospheric radius expansion X-ray bursts as standard candles”. In: *A&A* 399, pp. 663–680. DOI: 10.1051/0004-6361:20021781. arXiv: astro-ph/0212028 [astro-ph].
- Kuulkers, E., J. Homan, et al. (Feb. 2002). “X-ray bursts at extreme mass accretion rates from GX 17+2”. In: *A&A* 382, pp. 947–973. DOI: 10.1051/0004-6361:20011656. arXiv: astro-ph/0105386 [astro-ph].
- Kuulkers, E., M. van der Klis, and J. van Paradijs (Sept. 1995). “Burstlike Events in the Z Source Cygnus X-2”. In: *ApJ* 450, p. 748. DOI: 10.1086/176180.
- La Palombara, N. et al. (2009). “XMM-Newton observation of the persistent Be/NS X-ray binary pulsar RX J0440.9+4431”. In: *A&A* 505, p. 947. DOI: 10.1051/0004-6361/201118221.
- Lai, Dong (Jan. 2014). “Theory of Disk Accretion onto Magnetic Stars”. In: *European Physical Journal Web of Conferences*. Vol. 64. European Physical Journal Web of Conferences, 01001, p. 01001. DOI: 10.1051/epjconf/20136401001. arXiv: 1402.1903 [astro-ph.SR].
- Lasota, Jean-Pierre (June 2001). “The disc instability model of dwarf novae and low-mass X-ray binary transients”. In: *NewAR* 45.7, pp. 449–508. DOI: 10.1016/S1387-6473(01)00112-9. arXiv: astro-ph/0102072 [astro-ph].
- Lazar, Hadar et al. (Nov. 2021). “Spectral and Timing Analysis of NuSTAR and Swift/XRT Observations of the X-Ray Transient MAXI J0637-430”. In: *ApJ* 921.2, 155, p. 155. DOI: 10.3847/1538-4357/ac1bab. arXiv: 2108.03299 [astro-ph.HE].
- Leong, C. et al. (1971). “X-Ray Emission from the Magellanic Clouds Observed by UHURU”. In: *ApJ* 170.1950, p. L67. ISSN: 0004-637X. DOI: 10.1086/180842. URL: <http://adsabs.harvard.edu/doi/10.1086/180842>.
- Lewin, W. H. G., W. D. Vacca, and E. M. Basinska (Feb. 1984). “Precursors to X-ray bursts : the result of expansion and subsequent contraction of the neutron star’s photosphere.” In: *ApJL* 277, pp. L57–L60. DOI: 10.1086/184202.
- Lewin, Walter H. G., Jan van Paradijs, and Ronald E. Taam (Sept. 1993). “X-Ray Bursts”. In: *SSRv* 62.3-4, pp. 223–389. DOI: 10.1007/BF00196124.

- Lucke, R et al. (1976). “Discovery of X-ray pulsations in SMC X-1”. In: *ApJ* 206, pp. L25–L28.
- Ludlam, R. M. et al. (Mar. 2022). “Radius Constraints from Reflection Modeling of Cygnus X-2 with NuSTAR and NICER”. In: *ApJ* 927.1, 112, p. 112. DOI: 10.3847/1538-4357/ac5028. arXiv: 2201.11767 [astro-ph.HE].
- Maccarone, T. J. (Oct. 2003). “Do X-ray binary spectral state transition luminosities vary?” In: *A&A* 409, pp. 697–706. DOI: 10.1051/0004-6361:20031146. arXiv: astro-ph/0308036 [astro-ph].
- Madsen, K. K., D. Stern, and HEX-P Team (Apr. 2019). “HEX-P: The High-Energy X-Ray Probe”. In: *The Space Astrophysics Landscape for the 2020s and Beyond*. Vol. 2135. LPI Contributions, 5013, p. 5013.
- Madsen, Kristin K., Brian W. Grefenstette, et al. (May 2020). “NuSTAR low energy effective area correction due to thermal blanket tear”. In: *arXiv e-prints*, arXiv:2005.00569, arXiv:2005.00569. arXiv: 2005.00569 [astro-ph.IM].
- Madsen, Kristin K., Stephen Reynolds, et al. (Mar. 2015). “Broadband X-ray Imaging and Spectroscopy of the Crab Nebula and Pulsar with NuSTAR”. In: *ApJ* 801.1, 66, p. 66. DOI: 10.1088/0004-637X/801/1/66. arXiv: 1502.07765 [astro-ph.HE].
- Maitra, Dipankar and Charles D. Bailyn (Feb. 2006). “X-Ray Observations of V4641 SGR (SAX J1819.3-2525) during the Brief and Violent Outburst of 2003”. In: *ApJ* 637.2, pp. 992–1001. DOI: 10.1086/498422. arXiv: astro-ph/0510531 [astro-ph].
- Mandrou, P. (June 1990). “Galactic Center”. In: *IAUC* 5032, p. 1.
- Matsuoka, Masaru et al. (Oct. 2009). “The MAXI Mission on the ISS: Science and Instruments for Monitoring All-Sky X-Ray Images”. In: *PASJ* 61, p. 999. DOI: 10.1093/pasj/61.5.999. arXiv: 0906.0631 [astro-ph.IM].
- McClintock, Jeffrey E. and Ronald A. Remillard (2006). “Black hole binaries”. In: *Compact stellar X-ray sources*. Vol. 39, pp. 157–213.
- Meer, A. van der et al. (2007). “Determination of the mass of the neutron star in SMC X-1, LMC X-4, and Cen X-3 with VLT/UVES”. In: *A&A* 473.2, pp. 523–538. ISSN: 0004-6361. DOI: 10.1051/0004-6361:20066025. URL: <http://www.aanda.org/10.1051/0004-6361:20066025>.
- Migliari, Simone, Rob Fender, and Mariano Méndez (Sept. 2002). “Iron Emission Lines from Extended X-ray Jets in SS 433: Reheating of Atomic Nuclei”. In: *Science* 297.5587, pp. 1673–1676. DOI: 10.1126/science.1073660. arXiv: astro-ph/0209131 [astro-ph].
- Mihara, T (1995). “Observational study of X-ray spectra of binary pulsars with Ginga”. PhD thesis. Department of Physics, University of Tokyo.

- Mihara, T. et al. (Jan. 2021). “NuSTAR observation of the hard state of MAXI J1848-015”. In: *The Astronomer’s Telegram* 14327, p. 1.
- Mihara, Tatehiro et al. (Nov. 2011). “Gas Slit Camera (GSC) onboard MAXI on ISS”. In: *PASJ* 63, S623–S634. DOI: 10.1093/pasj/63.sp3.S623. arXiv: 1103.4224 [astro-ph.IM].
- Miller, J. M., A. C. Fabian, et al. (Sept. 2002). “A Relativistic Fe $K\alpha$ Emission Line in the Intermediate-Luminosity BeppoSAX Spectrum of the Galactic Microquasar V4641 Sgr”. In: *ApJL* 577.1, pp. L15–L18. DOI: 10.1086/344047. arXiv: astro-ph/0206467 [astro-ph].
- Miller, J. M., A. Sanna, et al. (Mar. 2021). “NICER Spectroscopy of MAXI J1848-015 in the Stellar Cluster GLIMPSE-C01”. In: *The Astronomer’s Telegram* 14429, p. 1.
- Miyasaka, Hiromasa et al. (Aug. 2009). “Development of a cadmium telluride pixel detector for astrophysical applications”. In: *UV, X-Ray, and Gamma-Ray Space Instrumentation for Astronomy XVI*. Ed. by Oswald H. Siegmund. Vol. 7435. Society of Photo-Optical Instrumentation Engineers (SPIE) Conference Series, 74350Q, 74350Q. DOI: 10.1117/12.825711.
- Moon, Dae-Sik, Stephen S Eikenberry, and Ira M Wasserman (2003). “SMC X-1 AS AN INTERMEDIATE-STAGE FLARING X-RAY PULSAR Dae-Sik Moon, Stephen S. Eikenberry, 1 and Ira M. Wasserman”. In: *ApJ* 582, pp. 91–94.
- Morii, M. et al. (Oct. 2010). “MAXI/GSC image fitting analysis for transient X-ray sources”. In: *Deciphering the Ancient Universe with Gamma-ray Bursts*. Ed. by Nobuyuki Kawai and Shigehiro Nagataki. Vol. 1279. American Institute of Physics Conference Series, pp. 391–393. DOI: 10.1063/1.3509322.
- Motch, C. et al. (2014). “A mass of less than 15 solar masses for the black hole in an ultraluminous X-ray source”. In: *Nature* 514.7521, pp. 198–201. ISSN: 14764687. DOI: 10.1038/nature13730.
- Muno, M. P., F. K. Baganoff, and J. S. Arabadjis (Nov. 2003). “The X-Ray Binary GRS 1741.9-2853 in Outburst and Quiescence”. In: *ApJ* 598.1, pp. 474–480. DOI: 10.1086/378851. arXiv: astro-ph/0307179 [astro-ph].
- Naik, S and B Paul (2004). “Beppo{SAX} observations of the accretion-powered {X}-ray pulsar {SMC} {X}-1”. In: *A&A* 418, pp. 655–661. ISSN: 00046361. DOI: 10.1051/0004-6361:20040048. arXiv: 0402096v1 [astro-ph]. URL: http://adsabs.harvard.edu/cgi-bin/nph-bib_query?bibcode=2004A&A...418..655N&db_key=AST&high=436c7b4a7a01561.
- Negoro, H. et al. (Dec. 2020). “A sudden decrease in soft X-ray flux of MAXI J1848-015”. In: *The Astronomer’s Telegram* 14292, p. 1.
- Negoro, Hitoshi et al. (June 2016). “The MAXI/GSC Nova-Alert System and results of its first 68 months”. In: *PASJ* 68, S1, S1. DOI: 10.1093/pasj/psw016.

- Neilsen, J, R C Hickox, and S D Vrtilik (2004). “PHASE VARIATION IN THE PULSE PROFILE OF SMC X-1”. In: *ApJ* 616, pp. 135–138.
- Paradijs, J van and E Zuiderwijk (1977). “Evidence for an Accretion Disk in SMC X-1”. In: *A&A* 61, pp. L19–L22.
- Penninx, W. et al. (Jan. 1989). “EXOSAT observations of the X-ray burst source 4U 1608-52.” In: *A&A* 208, pp. 146–152.
- Pfahl, Eric, Saul Rappaport, and Philipp Podsiadlowski (May 2002). “On the Population of Wind-accreting Neutron Stars in the Galaxy”. In: *ApJL* 571.1, pp. L37–L40. DOI: 10.1086/341197. arXiv: astro-ph/0203266 [astro-ph].
- Pike, Sean N., Fiona A. Harrison, Jill A. Burnham, Walter Cook, et al. (Sept. 2018). “Characterization of Redlen CZT detectors for hard x-ray astronomy”. In: *Hard X-Ray, Gamma-Ray, and Neutron Detector Physics XX*. Vol. 10762. Society of Photo-Optical Instrumentation Engineers (SPIE) Conference Series, 1076214, p. 1076214. DOI: 10.1117/12.2321990.
- Pike, Sean N., Fiona A. Harrison, Jill A. Burnham, Walter W. Cook, et al. (Aug. 2018). “Characterization of Redlen CZT detectors for x-ray astronomy”. In: *High Energy, Optical, and Infrared Detectors for Astronomy VIII*. Ed. by Andrew D. Holland and James Beletic. Vol. 10709. Society of Photo-Optical Instrumentation Engineers (SPIE) Conference Series, 107091D, p. 107091D. DOI: 10.1117/12.2313860.
- Pike, Sean N., Fiona A. Harrison, Karl Forster, et al. (Dec. 2020). “NuSTAR observations and a refined position estimate of MAXI J1848-015”. In: *The Astronomer’s Telegram* 14290, p. 1.
- Pottschmidt, Katja et al. (Aug. 2014). “NuSTAR observations of SMC X-1 at two different superorbital phases”. In: *AAS/High Energy Astrophysics Division #14*. AAS/High Energy Astrophysics Division, 117.02, p. 117.02. URL: https://files.aas.org/head14/117-02%5C%20Katja_Pottschmidt.pdf.
- Price, R. E. et al. (1971). “X-Rays from the Magellanic Clouds”. In: *ApJ* 168, p. L7. ISSN: 0004-637X. DOI: 10.1086/180773. URL: <http://adsabs.harvard.edu/doi/10.1086/180773>.
- Rai, Binay, Pragati Pradhan, and Bikash Chandra Paul (Dec. 2018). “A report on Type II X-ray bursts from SMC X-1”. In: *Research in Astronomy and Astrophysics* 18, 148, p. 148. DOI: 10.1088/1674-4527/18/12/148. arXiv: 1806.03244 [astro-ph.HE].
- Raichur, Harsha and Biswajit Paul (2010). “Effect of pulse profile variations on measurement of eccentricity in orbits of Cen X-3 and SMC X-1”. In: *MNRAS* 401.3, pp. 1532–1539. ISSN: 00358711. DOI: 10.1111/j.1365-2966.2009.15778.x.
- Ramo, S. (Sept. 1939). “Currents Induced by Electron Motion”. In: *Proceedings of the IRE* 27.9, pp. 584–585. DOI: 10.1109/jrproc.1939.228757.

- Reig, Pablo (2011). “Be/X-ray binaries”. In: *Astrophysics and Space Science* 332.1, pp. 1–29. ISSN: 0004640X. DOI: 10.1007/s10509-010-0575-8.
- Reig, Pablo and Paul Roche (1999). “Discovery of two new persistent Be/X-ray pulsar systems”. In: *MNRAS* 306.1, pp. 100–106. ISSN: 00358711. DOI: 10.1046/j.1365-8711.1999.02473.x.
- Revnivtsev, M., E. Churazov, et al. (June 2001). “New class of low frequency QPOs: Signature of nuclear burning or accretion disk instabilities?” In: *A&A* 372, pp. 138–144. DOI: 10.1051/0004-6361:20010434. arXiv: astro-ph/0011110 [astro-ph].
- Revnivtsev, M., M. Gilfanov, et al. (Sept. 2002). “Super-Eddington outburst of V4641 Sgr”. In: *A&A* 391, pp. 1013–1022. DOI: 10.1051/0004-6361:20020865. arXiv: astro-ph/0204132 [astro-ph].
- Reynolds, Christopher S. (Sept. 2021). “Observational Constraints on Black Hole Spin”. In: *Annual Review of Astronomy and Astrophysics* 59, pp. 117–154. DOI: 10.1146/annurev-astro-112420-035022. arXiv: 2011.08948 [astro-ph.HE].
- Santangelo, A et al. (1998). “BeppoSAX detection of a Cyclotron Feature in the spectrum of Cen X-3”. In: *A&A* 340, pp. L55–L59.
- Savitzky, Abraham and Marcel Golay (1964). “Smoothing and differentiation of data by simplified least squares”. In: *Z. Physiol. Chem. Chem. & Ind* 36.8, pp. 1627–1639.
- Schreier, E et al. (1972). “Discovery of the binary nature of smc x-1 from uhuru”. In: *ApJ* 178, p. L71. DOI: 10.1086/181086. URL: <http://adsabs.harvard.edu/full/1972ApJ...178L..71S%5Cnhttp://adsabs.harvard.edu/abs/1972ApJ...178L..71S>.
- Schwarz, Gideon (1978). “Estimating the Dimension of a Model”. In: *The Annals of Statistics* 6.2, pp. 461–464. DOI: 10.1214/aos/1176344136.
- Shakura, N. I. and R. A. Sunyaev (June 1973). “Reprint of 1973A&A...24..337S. Black holes in binary systems. Observational appearance.” In: *A&A* 500, pp. 33–51.
- Shimura, Toshiya and Fumio Takahara (June 1995). “On the Spectral Hardening Factor of the X-Ray Emission from Accretion Disks in Black Hole Candidates”. In: *ApJ* 445, p. 780. DOI: 10.1086/175740.
- Shockley, W. (Oct. 1938). “Currents to Conductors Induced by a Moving Point Charge”. In: *Journal of Applied Physics* 9.10, pp. 635–636. DOI: 10.1063/1.1710367.

- Singh, Kulinder Pal et al. (July 2014). “ASTROSAT mission”. In: *Space Telescopes and Instrumentation 2014: Ultraviolet to Gamma Ray*. Ed. by Tadayuki Takahashi, Jan-Willem A. den Herder, and Mark Bautz. Vol. 9144. Society of Photo-Optical Instrumentation Engineers (SPIE) Conference Series, 91441S, 91441S. DOI: 10.1117/12.2062667.
- Strohmayer, Tod E. et al. (Sept. 1997). “Millisecond Pulsations from a Low-Mass X-Ray Binary in the Galactic Center Region”. In: *ApJ* 486.1, pp. 355–362. DOI: 10.1086/304522.
- Strüder, L. et al. (Jan. 2001). “The European Photon Imaging Camera on XMM-Newton: The pn-CCD camera”. In: *Astronomy and Astrophysics* 365, pp. L18–L26. DOI: 10.1051/0004-6361:20000066.
- Sugizaki, Mutsumi, Tatehiro Mihara, et al. (Nov. 2011). “In-Orbit Performance of MAXI Gas Slit Camera (GSC) on ISS”. In: *PASJ* 63, S635–S644. DOI: 10.1093/pasj/63.sp3.S635. arXiv: 1102.0891 [astro-ph.IM].
- Sugizaki, Mutsumi, Kazuhisa Mitsuda, et al. (May 2001). “Faint X-Ray Sources Resolved in the ASCA Galactic Plane Survey and Their Contribution to the Galactic Ridge X-Ray Emission”. In: *ApJS* 134.1, pp. 77–102. DOI: 10.1086/320358. arXiv: astro-ph/0101093 [astro-ph].
- Suleimanov, V., J. Poutanen, and K. Werner (Mar. 2011). “X-ray bursting neutron star atmosphere models: spectra and color corrections”. In: *A&A* 527, A139, A139. DOI: 10.1051/0004-6361/201015845. arXiv: 1009.6147 [astro-ph.HE].
- Sunyaev, R. (Sept. 1990). “GX 1+4, KS 1731-260, GRS 1741.9-2853, A1524-62”. In: *IAUC* 5104, p. 1.
- Syunyaev, R. et al. (Jan. 1991). “Observations of the Galactic Center in the 4-30-KEV Range with the Art-P X-Ray Telescope of the GRANAT Observatory - Preliminary Results”. In: *Soviet Astronomy Letters* 17, p. 42.
- Sztajno, M. et al. (Dec. 1985). “Unusual X-ray burst profiles from 4U/MXB 1636-53.” In: *ApJ* 299, pp. 487–495. DOI: 10.1086/163715.
- Takagi, R. et al. (Dec. 2020). “MAXI/GSC detection of an X-ray outburst from a new X-ray transient MAXI J1848-015 or AX J1848.8-0129”. In: *The Astronomer’s Telegram* 14282, p. 1.
- Tanaka, Y (1986). “Observations of Compact X-Ray Sources”. In: *International Astronomical Union Colloquium*. Vol. 89, pp. 198–221. DOI: 10.1017/S0252921100086097.
- Tawara, Y. et al. (Jan. 1984). “A very long X-ray burst with a precursor from XB 1715-321.” In: *ApJL* 276, pp. L41–L44. DOI: 10.1086/184184.
- Tomsick, John A. et al. (2011). “Confirmation of IGR J01363+6610 as a Be X-ray Binary with very low quiescent X-ray luminosity”. In: *ApJ* 728.2, pp. 86–95. ISSN: 15384357. DOI: 10.1088/0004-637X/728/2/86.

- Trap, G. et al. (Sept. 2009). “Bursting behavior of the Galactic center faint X-ray transient GRS 1741.9-2853”. In: *A&A* 504.2, pp. 501–510. DOI: 10.1051/0004-6361/200911773. arXiv: 0906.3633 [astro-ph.HE].
- Tremou, Evangelia et al. (Mar. 2021). “MeerKAT observations of the new transient MAXI J1848-015”. In: *The Astronomer’s Telegram* 14432, p. 1.
- Tsygankov, Sergey S et al. (2016). “Propeller effect in action in the ultraluminous accreting magnetar M82 X-2”. In: *MNRAS* 457.1, pp. 1101–1106. ISSN: 13652966. DOI: 10.1093/mnras/stw046.
- Tsygankov, Sergey S. et al. (Sept. 2017). “The X-ray properties of Be/X-ray pulsars in quiescence”. In: *MNRAS* 470.1, pp. 126–141. DOI: 10.1093/mnras/stx1255. arXiv: 1703.04634 [astro-ph.HE].
- Turner, M. J. L. et al. (Jan. 2001). “The European Photon Imaging Camera on XMM-Newton: The MOS cameras”. In: *Astronomy and Astrophysics* 365, pp. L27–L35. DOI: 10.1051/0004-6361:20000087. arXiv: astro-ph/0011498 [astro-ph].
- Vahdat Motlagh, A., E. Kalemci, and T. J. Maccarone (May 2019). “Investigating state transition luminosities of Galactic black hole transients in the outburst decay”. In: *MNRAS* 485.2, pp. 2744–2758. DOI: 10.1093/mnras/stz569. arXiv: 1903.00837 [astro-ph.HE].
- van der Klis, M. (Nov. 1989). “The Z/atoll Classification”. In: *Two Topics in X-Ray Astronomy, Volume 1: X Ray Binaries. Volume 2: AGN and the X Ray Background*. Ed. by J. Hunt and B. Battrick. Vol. 1. ESA Special Publication, p. 203.
- van Paradijs, J. (Aug. 1978). “Average properties of X-ray burst sources”. In: *Nature* 274.5672, pp. 650–653. DOI: 10.1038/274650a0.
- van Paradijs, J. et al. (Aug. 1986). “A unique triple-peaked type-1 X-ray burst from 4U/MXB 1636-53.” In: *MNRAS* 221, pp. 617–623. DOI: 10.1093/mnras/221.3.617.
- Verner, D. A. et al. (July 1996). “Atomic Data for Astrophysics. II. New Analytic FITS for Photoionization Cross Sections of Atoms and Ions”. In: *ApJ* 465, p. 487. DOI: 10.1086/177435. arXiv: astro-ph/9601009 [astro-ph].
- Virtanen, Pauli et al. (Feb. 2020). “SciPy 1.0: fundamental algorithms for scientific computing in Python”. In: *Nature Methods* 17, pp. 261–272. DOI: 10.1038/s41592-019-0686-2. arXiv: 1907.10121 [cs.LG].
- Wachter, K., R. Leach, and E. Kellogg (May 1979). “Parameter estimation in X-ray astronomy using maximum likelihood.” In: *ApJ* 230, pp. 274–287. DOI: 10.1086/157084.
- Walton, D. J. et al. (2016). “A 78 DAY X-RAY PERIOD DETECTED FROM NGC 5907 ULX1 BY <i>SWIFT</i>”. In: *ApJ* 827, pp. L13–L19. DOI: 10.3847/2041-8205/827/1/L13.

- Watts, Anna L. (Sept. 2012). “Thermonuclear Burst Oscillations”. In: *ARA&A* 50, pp. 609–640. DOI: 10.1146/annurev-astro-040312-132617. arXiv: 1203.2065 [astro-ph.HE].
- Webster, B. L. et al. (1972). “Optical Candidate for SMC X-1”. In: *Nature Physical Science* 240, p. 183.
- Weisskopf, Martin C. et al. (July 2000a). “Chandra X-ray Observatory (CXO): overview”. In: *X-Ray Optics, Instruments, and Missions III*. Ed. by Joachim E. Truemper and Bernd Aschenbach. Vol. 4012. Society of Photo-Optical Instrumentation Engineers (SPIE) Conference Series, pp. 2–16. DOI: 10.1117/12.391545. arXiv: astro-ph/0004127 [astro-ph].
- (July 2000b). “Chandra X-ray Observatory (CXO): overview”. In: *X-Ray Optics, Instruments, and Missions III*. Ed. by Joachim E. Truemper and Bernd Aschenbach. Vol. 4012. Society of Photo-Optical Instrumentation Engineers (SPIE) Conference Series, pp. 2–16. DOI: 10.1117/12.391545. arXiv: astro-ph/0004127 [astro-ph].
- Wijnands, R. et al. (June 2005). “New outbursts of two faint X-ray transients (GRS 1741.9-2853 and XMM J174457-2850.3) located in the Galactic center region”. In: *The Astronomer’s Telegram* 512, p. 1.
- Wijnands, Rudy and Michiel van der Klis (Jan. 2000). “The Rapid X-Ray Variability of V4641 Sagittarii (SAX J1819.3-2525 = XTE J1819-254)”. In: *ApJL* 528.2, pp. L93–L96. DOI: 10.1086/312439. arXiv: astro-ph/9910079 [astro-ph].
- Wilkins, D. R. (Mar. 2018). “On the illumination of neutron star accretion discs”. In: *MNRAS* 475.1, pp. 748–756. DOI: 10.1093/mnras/stx3167. arXiv: 1712.02364 [astro-ph.HE].
- Wilms, J., A. Allen, and R. McCray (Oct. 2000). “On the Absorption of X-Rays in the Interstellar Medium”. In: *ApJ* 542.2, pp. 914–924. DOI: 10.1086/317016. arXiv: astro-ph/0008425 [astro-ph].
- Wojdowski, Patrick et al. (1998). “Quasi-periodic Occultation by a Precessing Accretion Disk and Other Variabilities of SMC X-1”. In: *ApJ* 502.1991, p. 253. ISSN: 15384357. DOI: 10.1086/305893. URL: http://adsabs.harvard.edu/cgi-bin/nph-bib_query?bibcode=1998ApJ...502..253W&db_key=AST&high=436c7b4a7a24054.
- Wolter, Hans (Jan. 1952). “Spiegelsysteme streifenden Einfalls als abbildende Optiken für Röntgenstrahlen”. In: *Annalen der Physik* 445.1, pp. 94–114. DOI: 10.1002/andp.19524450108.
- Woo, J. W., G. W. Clark, J. M. Blondin, et al. (1995). “Wind Dynamics in SMC X-1. II. Ginga and Rosat Observations”. In: *ApJ* 445.2, pp. 896–908. DOI: 10.1086/175749. URL: <http://adsabs.harvard.edu/abs/1995ApJ...445..896W>.

- Woo, J. W., G. W. Clark, and A. M. Levine (1995). “ROSAT Observations of Scattered X-rays from LMC X-4 in its low state”. In: *ApJ* 449, p. 880. DOI: 10.1086/176105. URL: <http://adsabs.harvard.edu/abs/1995ApJ...449..880W>.
- Worpel, Hauke, Duncan K. Galloway, and Daniel J. Price (Aug. 2013). “Evidence for Accretion Rate Change during Type I X-Ray Bursts”. In: *ApJ* 772.2, 94, p. 94. DOI: 10.1088/0004-637X/772/2/94. arXiv: 1303.4824 [astro-ph.HE].
- (Mar. 2015). “Evidence for Enhanced Persistent Emission During Sub-Eddington Thermonuclear Bursts”. In: *ApJ* 801.1, 60, p. 60. DOI: 10.1088/0004-637X/801/1/60. arXiv: 1501.02070 [astro-ph.HE].
- Xu, Yanjun et al. (Apr. 2020). “Evidence for Disk Truncation at Low Accretion States of the Black Hole Binary MAXI J1820+070 Observed by NuSTAR and XMM-Newton”. In: *ApJ* 893.1, 42, p. 42. DOI: 10.3847/1538-4357/ab7cdb. arXiv: 2003.01778 [astro-ph.HE].
- Zdziarski, A. A., W. N. Johnson, and P. Magdziarz (Nov. 1996). “Broad-band γ -ray and X-ray spectra of NGC 4151 and their implications for physical processes and geometry.” In: *MNRAS* 283.1, pp. 193–206. DOI: 10.1093/mnras/283.1.193. arXiv: astro-ph/9607015 [astro-ph].
- Zhang, Guobao, Mariano Méndez, and Diego Altamirano (May 2011). “The cooling phase of Type I X-ray bursts in 4U 1636-53”. In: *MNRAS* 413.3, pp. 1913–1921. DOI: 10.1111/j.1365-2966.2011.18271.x. arXiv: 1010.2533 [astro-ph.HE].
- Życki, Piotr T., Chris Done, and David A. Smith (Nov. 1999). “The 1989 May outburst of the soft X-ray transient GS 2023+338 (V404 Cyg)”. In: *MNRAS* 309.3, pp. 561–575. DOI: 10.1046/j.1365-8711.1999.02885.x. arXiv: astro-ph/9904304 [astro-ph].

Appendix A

BREAKING THE SPECTRAL FIT DEGENERACY

Fitting the MAXI J1848–015 spectra with their respective best fit models (described in Section 5.3) individually, rather than performing a joint fit, resulted in significant degeneracies between a number of parameters. In Figure A.1 we show the resulting distributions for those parameters which demonstrate this degeneracy. In particular, although the spin is consistent with values above $a = 0.7$, it is not particularly well-constrained.

In the soft state, the spin and the inclination show a clear dependence on one another, as do the spin and the inner radius. The latter degeneracy is due to the proximity of the inner radius with the inner-most stable circular orbit, the physical value of which depends directly on the spin of the central accretor. The strength of reflection, parameterized by the reflection fraction, f_{refl} , also shows a clear correlation with a number of parameters, including the absorption column density, the spin, the inclination, and the inner disk radius. In the hard state, on the other hand, the spin appears to be controlled mainly by the iron abundance, A_{Fe} , the absorption column density, the height of the lamppost, and the inner disk radius, and it shows less dependence on the inclination of the inner disk. In the soft state, the iron abundance consistently tended towards the lower limit of the model, $A_{\text{Fe}} = 0.5 A_{\text{Fe},\odot}$, so we froze the parameter at this value.

We also show the parameter distributions for the joint fits in Figure A.2 in order to demonstrate the superior constraints we were able to achieve via this method. Importantly, the spin and the inner disk inclination were constrained very well compared to the individual fits. A few distinct correlations remain, with the spin depending on the inner disk radius of the soft state and the lamppost height during the hard state, and the inclination being controlled by the ionization of the disk in the hard state. Both values also show a noticeable dependence on the absorption column density. Notably, using this joint fitting method, we obtained a well-constrained distribution for the iron abundance, which we were not able to achieve via the individual fits.

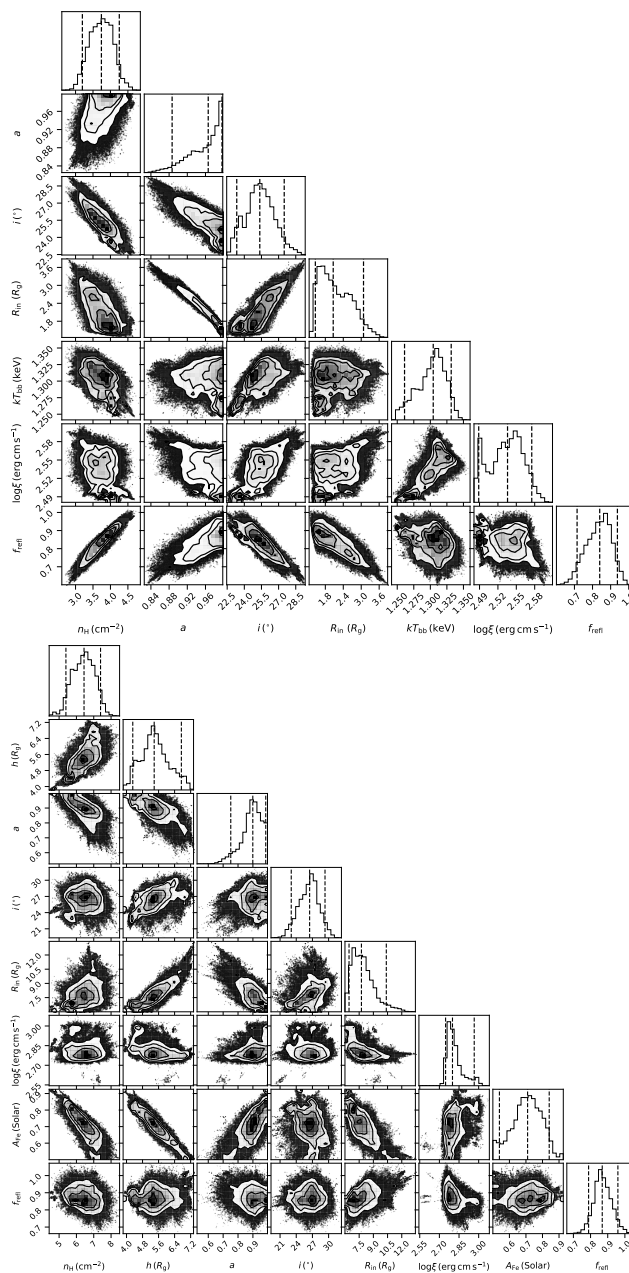


Figure A.1: Distributions of selected parameters resulting from MCMC analysis of each spectrum individually, without joint fitting. The dashed lines shown in the one-dimensional histograms represent, from left to right, the 5%, 50%, and 95% quantiles, while the contours shown in the two-dimensional histograms represent confidence regions of increasing sigma. Top: soft state parameters. Bottom: hard state parameters.

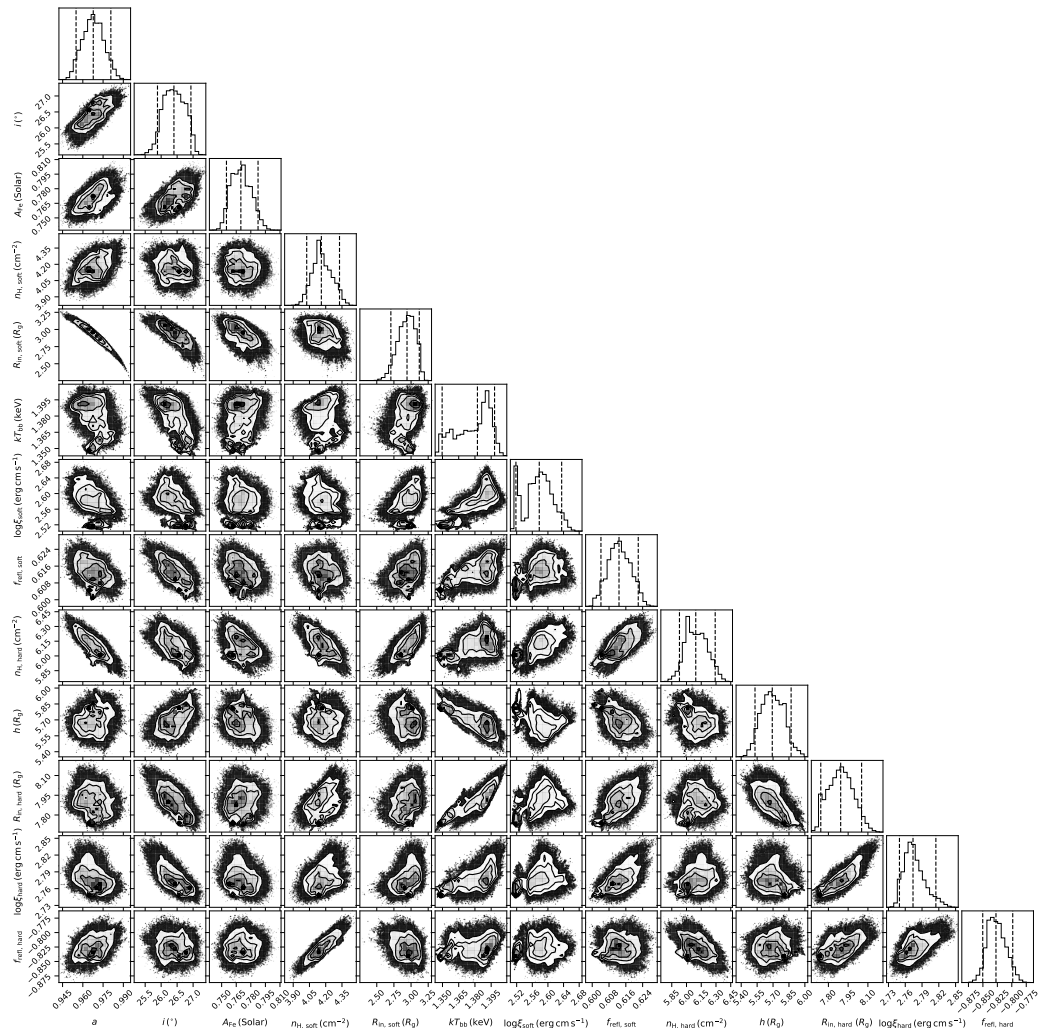


Figure A.2: Distributions of selected parameters resulting from MCMC analysis of the NuSTAR spectra with joint fitting where the parameters a , i , and A_{Fe} were tied between the soft and hard states. The dashed lines shown in the one-dimensional histograms represent, from left to right, the 5%, 50%, and 95% quantiles, while the contours shown in the two-dimensional histograms represent confidence regions of increasing sigma.

Appendix B

INVESTIGATING ERRORS IN HYBRIDIZATION

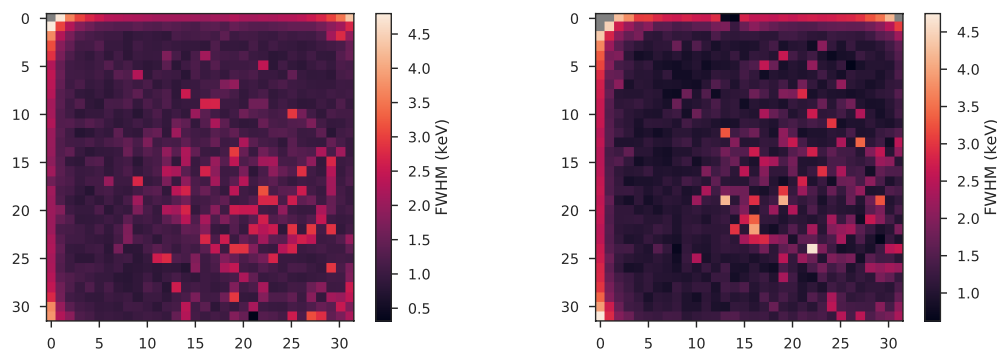


Figure B.1: Electronic noise maps for two hybrids which suffered poor hybridization. High levels of noise can be seen across the majority of each detector, rendering them both unusable for scientific applications. In the ideal case, the electronic noise should be less than 1 keV and should show good uniformity across the detector.

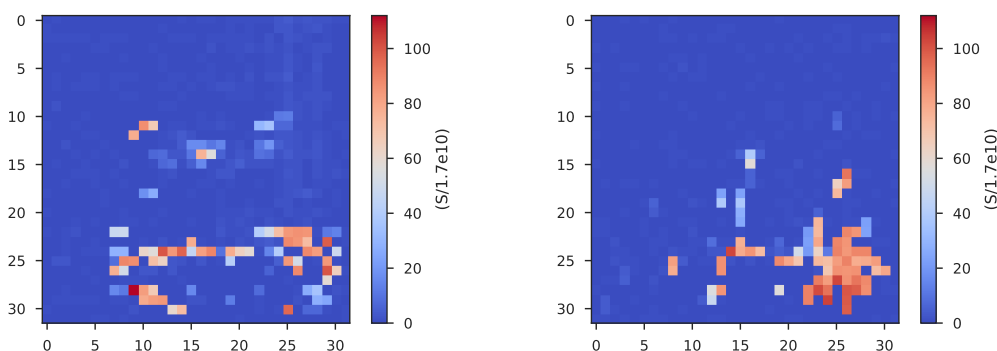


Figure B.2: Interpixel conductance maps for a hybrid which we determined to have suffered a failure in the application of epoxy during the hybridization process. The figure on the left shows the conductance in the horizontal direction, while the figure on the right shows the conductance in the vertical direction. Large regions of the detector were rendered unusable due to the high conductance between pixels.

In the process of characterizing Redlen CZT, we encountered a small set of hybrids which exhibited large regions of high electronic noise leading to many bursting pixels which had to be deactivated in order to mitigate spurious events. All of

these hybrids were flip-chip bonded in the same batch. Figure B.1 shows maps of electronic noise for two such detectors. A properly functioning hybrid should show good uniformity across the detector with a mean electronic noise contribution of less than 1 keV. We found that in one extreme case, the regions of high noise corresponded to regions of very high interpixel conductance as well. Figure B.2 shows the interpixel conductance in the horizontal and vertical directions for this hybrid. We therefore inferred that coupling between pixels may have been responsible for the high electronic noise seen in this batch of hybrids, and we hypothesized that this could be the result of an error in the hybridization process, particularly in the application of the conducting epoxy which is used to bond the CZT crystal to the gold studs on the custom ASIC.

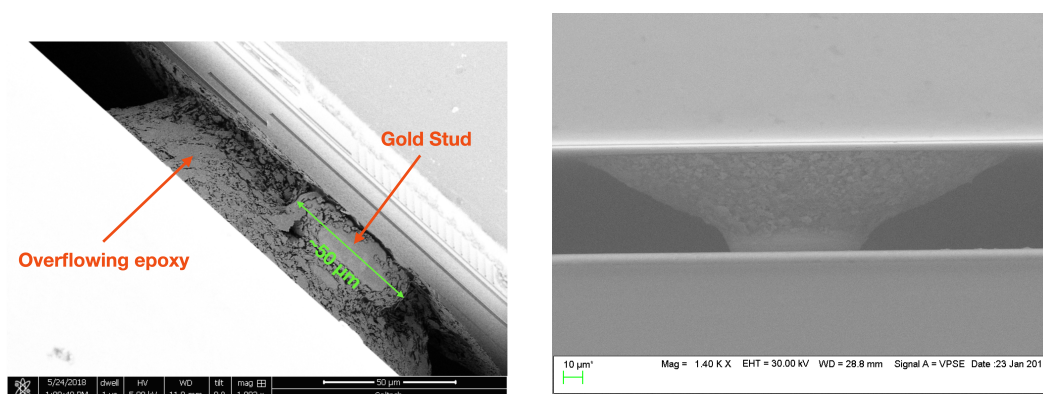


Figure B.3: SEM images of epoxy used to bond the CZT detector to the custom NuSTAR ASIC. On the left is shown an example of a failed bond, while on the right is shown a successful bond. It is clear from SEM imaging that the noisy batch of hybrids suffered from a failure in the application of epoxy which resulted in overflow onto the detector electronics. We inferred that this was the cause of the large-scale pixel failure observed in this batch of hybrids.

In order to investigate this hypothesis, I took one of the affected hybrids to the scanning electron microscope (SEM) housed in the Caltech GPS Division Analytical Facility. Because the detectors had already been hybridized, it was impossible to investigate the epoxy in the middle of the detectors, but I was able to image the epoxy along the edges. I found that the epoxy was flaky and that it did not set correctly on top of the gold studs which connect the CZT and the ASIC. Rather, I observed dramatic overflow of epoxy onto the detector electronics themselves. We alerted the firm which performed the flip-chip bonding procedure to this result, and they performed an investigation into their epoxy application process. They reported that the epoxy used for this batch was likely poorly mixed and stored, which could

have caused the hybridization failures which we observed. During the hybridization of subsequent batches of detectors, they addressed this issue, which appears to have addressed the noisy pixel behavior. The hybrid presented in Chapter 6 is one of the successfully hybridized detectors.